Energy-Dispersive NEXAFS: A Novel Tool for the Investigation of Intermolecular Interaction and Structural Phase Dynamics

Dissertation zur Erlangung des naturwissenschaftlichen Doktorgrades der Julius-Maximilians-Universität Würzburg

vorgelegt von

Markus Scholz

aus Deggendorf

Würzburg 2013

b

Eingereicht am 27.06.2013
bei der Fakultät für Physik und Astronomie

Gutachter der Dissertation:

1. Gutachter: Priv.-Doz. Dr. Achim Schöll
2. Gutachter: Prof. Dr. Jean Geurts

Prüfungskomitee im Promotionskolloquium:

1. Prüfer: Priv.-Doz. Dr. Achim Schöll
2. Prüfer: Prof. Dr. Jean Geurts
3. Prüfer: Prof. Dr. Björn Trauzettel

Tag des Promotionskolloquiums:

Ich habe keine besondere Begabung, sondern bin nur leidenschaftlich neugierig.

(Albert Einstein)

Abstract

In the context of this thesis, the novel method soft X-ray energy-dispersive NEXAFS spectroscopy was explored and utilized to investigate intermolecular coupling and post-growth processes with a temporal resolution of seconds. 1,4,5,8-naphthalene tetracarboxylic acid dianhydride (NTCDA) multilayer films were the chosen model system for these investigations.

The core hole-electron correlation in coherently coupled molecules was studied by means of energy-dispersive near-edge X-ray absorption fine-structure spectroscopy. A transient phase was found which exists during the transition between a disordered condensed phase and the bulk structure. This phase is characterized by distinct changes in the spectral line shape and energetic position of the X-ray absorption signal at the C K-edge. The findings were explained with the help of theoretical models based on the coupling of transition dipole moments, which are well established for optically excited systems. In consequence, the experimental results provides evidence for a core hole-electron pair delocalized over several molecules.

Furthermore, the structure formation of NTCDA multilayer films on Ag(111) surfaces was investigated. With time-resolved and energy-dispersive NEXAFS experiments the intensity evolution in s- and p-polarization showed a very characteristic behavior. By combining these findings with the results of time-dependent photoemission measurements, several sub-processes were identified in the post-growth behavior. Upon annealing, the amorphous but preferentially flat-lying molecules flip into an upright orientation. After that follows a phase characterized by strong intermolecular coupling. Finally, three-dimensional islands are established. Employing the Kolmogorov-Johnson-Mehl-Avrami model, the activation energies of the sub-processes were determined.

Zusammenfassung

Im Rahmen dieser Arbeit wurden die Möglichkeiten der neuartigen Methode energiedispersive Röntgen-Nahkanten-Absorptions-Spektroskopie für die Untersuchung intermolekularer Wechselwirkungen und zeitabhängiger Prozesse während der Strukturbildung aufgezeigt. Als Modellsystem wurden hierbei 1,4,5,8-Naphthalin-Tetracarboxylsäure-Dianhydrid- (NTCDA-) Filme verwendet.

Es wurde die Rumpfloch-Elektronen-Wechselwirkung kohärent gekoppelter Moleküle mittels energiedispersiver Röntgen-Nahkanten-Absorptions-Spektroskopie untersucht. Dabei wurde eine Übergangsphase gefunden, die während der Ausbildung einer langreichweitigen Ordnung zeitlich zwischen der ungeordneten und der Volumenstruktur auftritt. Diese Übergangsphase zeichnete sich durch eine charakteristische Änderung der spektralen Linienform und ihrer energetischen Position bei Messungen an der C K-Kante aus. Die experimentellen Befunde lassen sich mit Hilfe theoretischer Modelle erklären, welche die Kopplung von Übergangsdipolmomenten beschreiben. Diese theoretischen Konzepte sind bei optisch angeregten Systemen etabliert. Die experimentellen Ergebnisse zeigen den über mehrere Moleküle delokalisierten Charakter des Rumpfloch-Elektron-Paars.

Zudem wurde die Strukturbildung von mehrlagigen NTCDA-Filmen auf Ag(111) untersucht. Zeitabhängige energiedispersive NEXAFS-Experimente mit s- und p-polarisiertem Licht zeigten ein charakteristisches Verhalten. In Kombination mit zeitabhängigen Photoemissionsmessungen wurden bei der Strukturbildung verschiedene Unterprozesse gefunden. Nach erwärmen der Probe richten sich die ursprünglich flach orientierte Moleküle zunächst auf. Im Anschluss folgt eine Aggregation der Moleküle in einer Phase mit starker intermolekularer Kopplung. Letztendlich bildet sich die bekannte dreidimensionale Filmstruktur aus. Anhand des Kolmogorov-Johnson-Mehl-Avrami Modells konnte die Aktivierungsenergie für die verschiedenen Unterprozesse ermittelt werden.

Contents

1

Introduction

The pioneering experiments concerning organic electronics date back to 1862. H. Letheby anodically oxidized the organic compound aniline in sulphuric acid and found coloured films. By changing the applied electric potential between anode and cathode, Letheby could change the colour of the film [1]. Most interestingly, the pigments were conductive although the reactants were electrically insulating before oxidation. After these early experiments and increasing research on conducting organic molecules in the following years, A. Heeger, A. G. MacDiarmid and H. Shirakawa transformed in 1976 an insulating polymer into a material with metal-like conductivity by doping it with iodine vapor and, thus, discovered conducting polymers. In 2000 they were awarded the Nobel prize in chemistry "for the discovery and development of conductive polymers" [2].

The first electronic product with an organic electronics component I owned was a Pioneer car radio with an organic light-emitting diode (OLED) display in early 2000. It was also one of the first consumer products utilizing conducting organic materials. Nowadays, organic electronics are increasingly installed in premium products and convince the users with unique properties such as flexibility and transparency. Needless to say, the commercial interest is also fueled by the low-cost fabrication processes. In molecular vapor deposition or roll-to-roll techniques organic films can be deposited on inexpensive substrates, e.g. metal foils and glasses. OLED displays are more and more used in smartphones, tablet computers and high-definition television systems and they offer deep black levels, bright whites and a higher contrast ratio than that obtained with LCD panels.

Despite commercial applications and the enormous amount of theoretical and experimental research, there are still gaps in our understanding of plastic devices which need to be filled to optimize the performance. The better we understand the molecule and its interactions with the surrounding, the easier it is to predict the physical and electric properties of such molecules and to design new and efficient materials. One bottleneck is the relatively low charge carrier mobility

(electrons and/or holes) in contrast to silicon- or germanium-based electronics. From a microscopic point of view, the chemical composition and geometric arrangement but also the intermolecular interaction determines the mobility. For instance, if molecules are arranged in a way that the frontier orbitals of adjacent dye molecules overlap, band dispersion and high charge carrier mobility can be observed [3–7]. Also the morphology of the conducting material is of crucial importance for the construction of high-performance devices. For a high mobility, large domains and highly ordered films are most desirable [8–11].

In this work, I will study the intermolecular interaction and the post-growth of molecular films in real time. Such time-dependent measurements are mandatory for studying transient phases as well as organic film growth and post-growth and they can contribute to a better understanding of the underlying physics of intermolecular coupling and morphology evolution [12–16].
In particular, I will investigate in the first part of my experimental results a new transition phase of 1,4,5,8-naphthalene tetracarboxylic acid dianhydride (NTCDA) multilayer films which exhibits peculiar changes in the line shape and energy position of the X-ray absorption signals at the C K-edge. I demonstrate that these spectral changes can be attributed to an intermolecularly delocalized core hole-electron pair which is facilitated by the coupling of transition dipole moments between adjacent molecules. From the spectral shape change upon aggregation, the coherence length of the delocalized core exciton can be extracted. The second part of my experimental results deals with a real-time post-growth study where I investigate the morphology evolution and the formation of a three-dimensional, stable geometric structure within NTCDA multilayer films. The initially amorphous film undergoes several sub-processes during structure formation which I was able to identify with time-dependent X-ray absorption and photoemission experiments. From the evolution of the X-ray absorption signals and from measurements at different temperatures I quantify the activation energy as a thermodynamic parameter which is important for structure formation.

The results were obtained with a novel method, i.e. energy-dispersive near-edge X-ray absorption fine-structure (NEXAFS) spectroscopy. Energy-dispersive NEXAFS is a very powerful method. It combines the advantages of the traditional NEXAFS setup with a fast data acquisition at high energy resolution. As a local probe with a high chemical selectivity, it is suited for investigations of specific core-to-valence transitions which might be sensitive to intermolecular interactions. Since I also probed the involved vibronic modes [17–19], specific and characteristic changes of the spectral signature can be traced back to intermolecular coupling. Time-dependent energy-dispersive NEXAFS measurements allowed me

to explore short-lived transient phases, determine the molecular orientation, and investigate the influence on the electronic properties simultaneously.

In Chapter 2, I will lay out the theoretical concepts of intermolecular interaction and film growth relevant in this work. Hereby I will focus on the intermolecular interaction based on transition dipole moments (Section 2.1.1–2.1.2). A short introduction to molecular growth will follow, after which I present a kinetic nucleation model (see Section 2.2.2). After laying out the theoretical background of X-ray absorption spectroscopy in Chapter 3, I will introduce the novel method, energy-dispersive near-edge X-ray absorption fine-structure, in Chapter 4. In Chapter 5, my experimental results of coherently coupled molecules (see Section 5.2) and a post-growth study of NTCDA multilayer films (see Section 5.3) will follow. Finally, I will summarize my findings in Chapter 6.

2

Theoretical concepts

In this chapter, different theoretical models will be presented which constitute the basis for the experiments. In Section 2.1, some basic models of intermolecular interaction will be outlined. They describe some of the fundamental coupling concepts for intermolecular interaction, although they are mostly applied for optically excited systems. Their validity in the context of X-ray excitations will be investigated in the course of this work. In Chapter 2.1.1, I will focus on the Coulomb interaction between transition dipole moments of adjacent molecules (i.e. Förster interaction, [20]). The coupling strength is related to the geometric arrangement of the transition dipole moments and, thus, to the molecular orientation. In the following Chapter 2.1.2, the coherent exciton scattering approximation (CES) [21,22] will be examined. Under certain circumstances, the absorption signature of a molecule changes drastically and can be best explained by a coherently transferred hole-electron pair within a molecular aggregate. Finally, in Chapter 2.1.3 a short discussion of molecular orbital overlap and its contribution to the molecular coupling mechanism will follow.

After treating the electronic coupling of molecules, I will give a short introduction to growth and post-growth processes of molecular layers in Chapter 2.2. Despite most of the presented mathematical models were developed for atomistic growth and post-growth of atomic layers [23], the principal ideas can be adapted to molecular systems [24–27]. In Chapter 2.2.1, I will introduce some of the basic descriptions of crystal growth and distinguish between three fundamental growth modes. The crystal growth must not solely be described for systems in thermal equilibrium, but also the post-growth kinetics and re-organization have to be taken into account. The Kolmogorov-Johnson-Mehl-Avrami kinetic model has proven very successful in modeling the post-growth nucleation of amorphous materials, polymers, metals and metal alloys. This model will be introduced in Chapter 2.2.2. It describes a first-order phase transition and nucleation and is widely used to obtain kinetic parameters, e.g. the activation energy of a particular phase change.

2.1 Intermolecular interaction

The electronic structure of organic thin films strongly depends on the properties of the individual molecules, which are determined by the chemical composition. Intermolecular forces are weak compared to intramolecular forces, nevertheless, intermolecular interaction can affect and alter the optical and electronic properties of condensed films [28–32]. Some effects of intermolecular interaction can be explained by the pairwise electronic and vibronic coupling between adjacent dye molecules. In the following, I will concentrate on those basic concepts which might prove relevant for the interpretation of the experimental results. A detailed and comprehensive discussion of intermolecular interaction can be found in the literature [21, 33–37].

By following the argumentation outlined in the references above, I will demonstrate that intramolecular vibronic modes can couple between neighboring molecules. The Hamiltonian H_n of a single molecule is

$$\hat{H}_n = \hat{K} + \hat{H}^{el}, \tag{2.1}$$

where $\hat{K}$ is the kinetic energy operator of the nuclei and $\hat{H}^{el}$ the electronic Hamiltonian of the molecule. The Hamiltonian $\hat{H}_{non}$ of a well-defined assembly of N non-interacting molecules labeled $n = 1, \cdots, m, \cdots, N$ can be expressed as the sum of the individual molecular Hamiltonians

$$\hat{H}_{non} = \sum_{n=1}^{N} \hat{H}_n. \tag{2.2}$$

For a pairwise interaction between nearest-neighbor molecules, the aggregate Hamiltonian $\hat{H}_{agg}$ is given by the sum of the monomer Hamiltonians and the pairwise intermolecular interaction operator $V = \sum_{n>m} V_{nm}$, where V_{nm} is the Coulomb interaction between molecules n and m. For the aggregate Hamiltonian $\hat{H}_{agg}$ thus follows

$$\hat{H}_{agg} = \sum_{n=1}^{N} \hat{H}_n + V = \hat{H}_{non} + V. \tag{2.3}$$

For the sake of simplicity, the wave functions of neighboring molecules are assumed not to overlap. Thus, the intermolecular interaction V is restricted to Coulomb dipole-dipole coupling but it also allows to express the aggregate wave function as a Hartree product of single molecular wave functions $|\psi_m\rangle$. With this

constraint, the electronic part of the aggregate wave function in the ground state is given by

$$|\pi^g\rangle = \prod_{m=1}^{N} |\psi_m^g\rangle. \tag{2.4}$$

If after an excitation of monomer n all other N–1 molecules remain in their ground state, the electronic part of the wave function $|\pi_n\rangle$ can be expressed as

$$|\pi_n\rangle = |\psi_n^e\rangle \prod_{m\neq n}^{N} |\psi_m^g\rangle. \tag{2.5}$$

Also the vibrational coupling to the electron excitation has to be considered. For small aromatic molecules, the excitation will couple to various intramolecular vibrational modes [17, 19, 38, 39], which can be defined as $|\zeta_n\rangle$ for molecule n. Under the assumption that all other N–1 molecules remain in their vibronic ground state, which is defined as $|\chi\rangle$, the vibrational aggregate wave function can be expressed as follows [36]:

$$|\Psi_{n,\nu_n}\rangle = |\pi_n\rangle\,|\zeta_n\rangle \prod_{m\neq n}^{N} |\chi_m\rangle, \tag{2.6}$$

where molecule n is excited and ν_n refers to the specific vibrational numbers $(\chi_1, \cdots \zeta_n, \cdots \chi_N)$. In this basis the matrix elements of the aggregate Hamiltonian 2.3 are given as follows [36, 40, 41]

$$\left\langle \Psi_{n,\nu_n} \left| \hat{H}_{agg} \right| \Psi_{m,\widetilde{\nu}_m} \right\rangle = \epsilon^{\nu_n}\delta_{nm}\delta_{\nu_n,\widetilde{\nu}_m} + V_{nm}\left\langle \zeta_n \right| \widetilde{\chi}_n \left\rangle \right\langle \chi_m \right| \widetilde{\zeta}_m \Big\rangle \prod_{\substack{i=1 \\ i\neq n,m}}^{N} \delta_{\chi_i\widetilde{\chi}_i}, \tag{2.7}$$

with $\epsilon^{\nu_n} = \epsilon^{\chi_1} + \cdots + \epsilon^{\zeta_n} + \cdots + \epsilon^{\chi_N}$, where ϵ^{ζ_n} is the energy eigenstate of molecule n in the excited vibrational state $|\zeta_n\rangle$ and ϵ^{χ_i} refers to the electronic ground state of molecule i in the vibrational ground state $|\chi_i\rangle$. Furthermore, the manifold of vibronic transitions of the aggregate is governed by the product of the Franck-Condon factors $\langle\chi_n|\zeta_n\rangle$ and $\langle\chi_m|\zeta_m\rangle$. For a detailed discussion of the Franck-Condon principle and factors, see Chapter 3.2.

The aggregate matrix elements of expression 2.7 demonstrate that the intermolecular coupling V mixes the vibrational states of the excited molecule n with the vibrational state of molecule i in the ground state. Hence, a change in the vibronic signature during the formation of molecular aggregates can serve as a probe for investigations on the intermolecular interaction strength. Nevertheless, it has to be stressed that not every change in the vibronic signature can be traced back

to intermolecular interaction. Only some very specific and characteristic spectral changes can be identified as a consequence of intermolecular coupling. In the next sections, I will take a closer look at this topic.

2.1.1 Dipole-dipole interaction

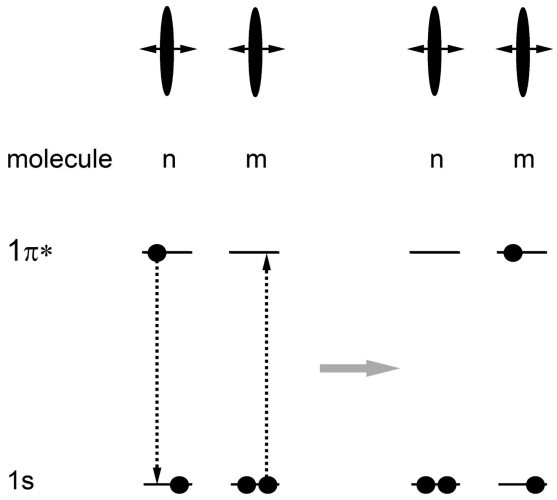

Figure 2.1: Transition dipole-dipole coupling mechanism between molecules n and m. In the upper part, molecule n and m are aligned parallel. The transition dipole moments (left-right arrows) are orientated perpendicular to the molecular plane. In the lower part, the energy levels are represented schematically for both molecules. Molecule n is in an excited state in which one 1s core electron was promoted from the core 1s level to the primarily unoccupied orbital $1\pi^*$. The dotted black arrows indicate the change in electron configuration resulting from the Coulomb interaction between the transition dipole moments of molecules n and m. After the initial excitation, molecule n is in its ground state and molecule m is excited.

For simplicity, I will demonstrate the Coulomb transition dipole-dipole interaction (Förster interaction [20]) for two coupled molecules. The interaction between the transition dipole moments of two nearest-neighbor molecules is analogous to the classic electrostatic interaction of two electric dipoles. Furthermore, the dipole approximation for the interacting transition moments can be assumed to be valid. Higher orders of interaction beyond the dipole approximation (quadrupole-quadrupole, octopole-octopole, etc.) may be important in systems where the Coulomb interaction is extremely small. Only in such cases, higher orders of interaction can contribute significantly to the transition [33, 34].

The process I will discuss in this section is illustrated in Fig. 2.1. For a comprehensive overview of various interaction processes of two-level molecular systems, see [33–35, 37].

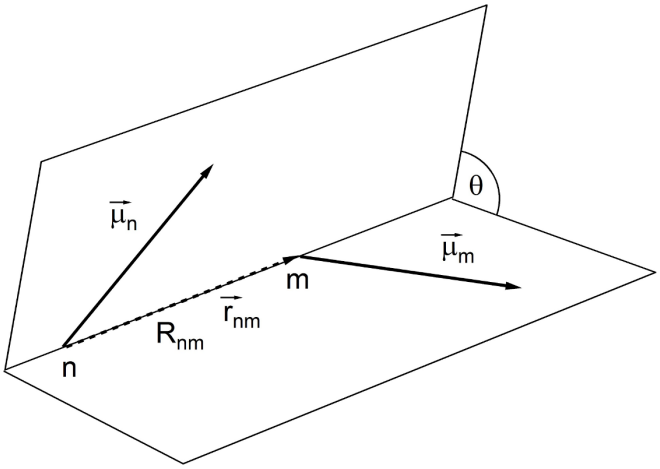

Figure 2.2: Transition dipole moments $\vec{\mu}_n$ and $\vec{\mu}_m$ of molecules n and m, respectively, separated by a distance R_{nm}.

The transition dipole moments corresponding to an 1s–1π^* transition are orientated perpendicular to the molecular plane. In the ground state, the core level is completely filled and the orbital 1π^* is unoccupied. On the left hand side of Fig. 2.1, one core electron is already promoted to the primarily unoccupied molecular orbital 1π^*. The Förster interaction between the transition dipole moments of molecules n and m triggers a deexcitation of molecule n and promotes a core electron of molecule m into the 1π^* orbital. This process is often called *resonant* dipole-dipole interaction [34, 37] because the energy difference between ground and excited state, i.e. $\Delta E = E_{1\pi^*} – E_{1s}$, is the same for molecule n and m. Therefore, the excitation energy is *resonantly* transferred from one molecule to the other.

In the Hamiltonian 2.3, the operator V is identified as the transition dipole-dipole interaction between molecules n and m. Assuming two identical molecules, V_{nm} is determined in [42] as follows:

$$\langle \Psi_n | \, V \, | \Psi_m \rangle = \mu_n \vec{n}_{\vec{\mu}_n} \cdot T_{nm} \cdot \vec{n}_{\vec{\mu}_m} \mu_m, \tag{2.8}$$

were μ_n and μ_m are the magnitude and $\vec{n}_{\vec{\mu}_n}$ and $\vec{m}_{\vec{\mu}_m}$ are the orientation of the transition dipole matrix element of molecules n and m, respectively. T_{nm} is given by:

$$T_{nm} = \frac{1 - 3\vec{r}_{nm}\vec{r}_{nm}}{R_{nm}^3}, \tag{2.9}$$

where $\vec{r}_{mn}$ is the vector pointing from the mass center of molecule m to the mass center of n. R_{nm} is the absolute value of the distance between molecules n and m. In Fig. 2.2, the transition dipole moments $\vec{\mu}_n$ and $\vec{\mu}_m$ are illustrated.

In this notation, V_{nm} is given by

$$V_{nm} = |\vec{\mu}_n|\,|\vec{\mu}_m| \cdot \left(\frac{\vec{n}_{\vec{\mu}_n}\vec{n}_{\vec{\mu}_m}}{R_{nm}^3} - \frac{3(\vec{n}_{\vec{\mu}_n}\vec{r}_{nm})(\vec{n}_{\vec{\mu}_m}\vec{r}_{nm})}{R_{nm}^5} \right). \tag{2.10}$$

For coplanar arranged dipoles, where θ is the dihedral angle with respect to $\vec{r}_{nm}$ that connects the transition dipoles, equation 2.10 can be rewritten to obtain

$$V_{nm} = |\vec{\mu}_n|\,|\vec{\mu}_m| \cdot \frac{(1 - 3\cos^2\theta)}{R_{nm}^3}. \tag{2.11}$$

Thus, for the transition dipole-dipole coupling follows that the magnitude of the interaction depends on the magnitude of the participating transition dipole moments ($|\vec{\mu}_n|$ and $|\vec{\mu}_m|$), the distance R_{nm}, and the angle θ. For $\theta \sim 54.7°$, the so-called *magic angle*, the dipole-dipole interaction is zero due to $1–3\cos^2\theta = 0$. For the angles $\theta = 0°$ and $\theta = 90°$, where the dipoles are aligned parallel and perpendicular, respectively, V_{nm} has a minimum at $-2 \cdot |\vec{\mu}_n|\,|\vec{\mu}_m|$ and maximum at $|\vec{\mu}_n|\,|\vec{\mu}_m|$, respectively. In the next section, I will outline the CES approximation and model the effect of transition dipole-dipole interactions on the shape of the absorption spectra of interacting molecules, with a particular focus on the sign of the coupling constant.

2.1.2 Coherent exciton scattering approximation

The coherent exciton scattering approximation (CES) was developed by Briggs et al. [21] and describes the coherent propagation of a hole-electron pair between interacting polymers. In his model, the delocalized hole-electron pair has a very specific spectroscopic signature, which was found for a certain type of molecular aggregates, the so-called J-aggregates. Briggs' approach to the coherent hole-electron propagation is similar to a model for the exciton photon interaction in the coherent-potential approximation (CPA) [43] and theoretical concepts for the electron propagation in random lattices [44–46]. In the following, I will introduce the CES approximation and explain the effect of intermolecular interaction on the spectral shape of the absorption. A detailed discussion of the CES approximation can be found in the literature [21, 22, 36, 40, 47–52].

The time evolution of the exciton propagation within an aggregate is given by the time-dependent Schrödinger equation

$$i\hbar\partial_t \left|\Psi(t)\right\rangle = \hat{H} \left|\Psi(t)\right\rangle . \tag{2.12}$$

Finding a Green's function $G(t)$ satisfying equation 2.12 is equivalent to solving the time-dependent Schrödinger equation. Briggs et al. [21, 22] exploited a one-particle Green's function approach to the optical exciton propagation within a molecular aggregate. In the time space, a Green's operator is given by

$$G(t) = \exp\left(-\frac{i\hat{H}t}{\hbar}\right)\theta(t) \quad \text{with} \quad \begin{array}{l}\theta(t) = 0 \ \text{ for } \ t < 0\\ \theta(t) = 1 \ \text{ for } \ t > 0,\end{array} \tag{2.13}$$

where $\hat{H}$ is the Hamiltonian, $\hbar$ is Planck's constant, and t is the time. To apply this function to absorption spectra, the Green's function 2.13 is Fourier-transformed into the energy space first, leading to

$$G(E) = -\frac{i}{\hbar}\int_{-\infty}^{\infty} dt\ G(t)\exp\left(-\frac{iEt}{\hbar}\right) = \frac{1}{E - \hat{H} + i\delta} \ \text{ with } \delta = 0_+. \tag{2.14}$$

Inserting the Hamiltonian 2.2, or the Hamiltonian 2.3 for interacting molecules, respectively, into the Green's function 2.14 yields the equations

$$g(E) = \frac{1}{E - \hat{H}_0 + i\delta} \tag{2.15}$$

$$G(E) = \frac{1}{E - \hat{H}_{agg} - V + i\delta}, \tag{2.16}$$

where $g(E)$ is the Green's function for non-interacting molecules and $G(E)$ is the Green's function for interacting molecules. With the following operator identity

$$\frac{1}{A - B} = \frac{1}{A} + \frac{1}{A - B}\cdot\frac{B}{A}$$

and $A = E – \hat{H}_0 + i\delta$ and $B = V$, the Green's functions $g(E)$ and $G(E)$ can be rearranged to the Dyson's equation

$$G(E) = g(E) + G(E)\ V\ g(E). \tag{2.17}$$

The difference between the inverse of the non-interacting and interacting Green's function is the intermolecular interaction V

$$V = g(E)^{-1} - G(E)^{-1}, \tag{2.18}$$

which is also referred to as the particle's, i.e. the optical exciton's, self-energy.

The absorption cross-section is proportional to the imaginary part of the spectral function and is given by [21, 22]

$$\sigma_{\vec{e}} \propto \mathrm{Im}\left(\sum_{nm} (\vec{e}\vec{\mu}_n) G_{nm} (\vec{\mu}_m \vec{e})\right), \tag{2.19}$$

where $\vec{e}$ is the polarization vector of the light and $\vec{\mu}_n$ and $\vec{\mu}_m$ the transition dipole moment of molecules n and m, respectively. With equation 2.17, it follows that

$$\sigma_{\vec{e}} \propto \mathrm{Im}\left(\sum_{nm} (\vec{e}\vec{\mu}_n) \left(\frac{g_n(E)}{1 - \sum_n V_{nm}\ g_n(E)}\right) (\vec{\mu}_m \vec{e})\right). \tag{2.20}$$

In the CES approximation, the exact single-molecule Green's function $g(E)$ is replaced by its average $\langle g \rangle$ if the molecule is in the ground vibronic and electronic state. Assuming that the intermolecular interaction V is independent of the vibrations, it follows that

$$\langle G \rangle = \langle g \rangle + \langle g \rangle V \langle G \rangle . \tag{2.21}$$

With this, the averages of the aggregate Green's function matrix elements of the aggregate Green's function can be obtained:

$$\langle \langle \Psi_n | G | \Psi_m \rangle \rangle = \langle G_{nm} \rangle$$
$$\langle G_{nm} \rangle = \langle g_n \rangle \delta_{nm} + \langle g_n \rangle V_{nm} \langle g_m \rangle + \sum_{n'} \langle g_n \rangle V_{nn'} \langle g_{n'} \rangle V_{n'm} \langle g_m \rangle + \cdots .$$

The coherent coupling can be best understood in the iterative form of equation 2.21. Here, the electron hole is transferred between single molecules which remain in their vibrational ground state. Degradation during the propagation of the exciton will not be considered [21, 22]. Therefore, the electron is coherently transferred between neighboring molecules.

The CES approximation was successfully applied for coherently coupled molecules [21, 22, 36, 40, 47–52]. Any measured absorption spectrum of an isolated molecule is related to the absorption cross section of a single molecule and, thus, to the imaginary part of the Green's function (equation 2.19). With the Kramers-Kronig relation [53, 54], the real part of the Green's function can be calculated and the aggregate Green's function $\langle G(E) \rangle$ can be determined with equation 2.21. Therefore, only with the monomer absorption spectra it is possible to model the absorption signature of coherently coupled molecules.

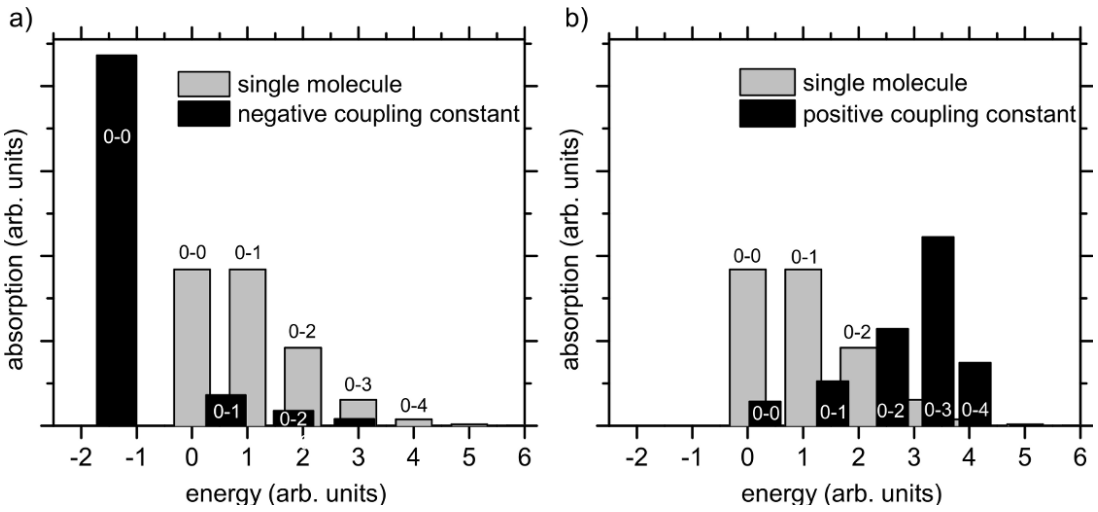

Figure 2.3: Results of coherent exciton scattering calculations: The adiabatic component of the (0–0) transition and the vibronic progression (0–1, 0–2, 0–3) are plotted for an isolated molecule (gray) and coupled molecules (black). In a) the coupling constant is negative, in b) it is positive.

In Fig. 2.3, I demonstrate the calculation of the coherent coupling with the CES approximation. For a single molecule, the intensity of the adiabatic component of the (0–0) transition and the corresponding vibronic progression (0–1, 0–2, 0–3) follows a Poisson distribution. The absolute value and the sign of the coupling constant strongly affects the absorption signature of interacting molecules. In Fig. 2.3, the same absolute values of the coupling constant were chosen for both calculations, only with different signs. For a negative constant, the adiabatic component shifts to lower energy and increases in intensity. As it is evident in Fig. 2.3 a), the intensity of the corresponding vibronic progression decreases drastically. For a positive constant, the absorption spectrum shifts to higher energy. In addition, also the spectral signature changes, as can be seen in Fig. 2.3 b). For a detailed discussion of the spectral shape in respect to the coupling constant, see References [21, 22, 36].

2.1.3 Wave function overlap

In Chapter 2.1, the aggregate wave function was constructed as a Hartree product of single-molecule wave functions. By excluding the wave function overlap between adjacent dye molecules, intermolecular interaction was restricted to

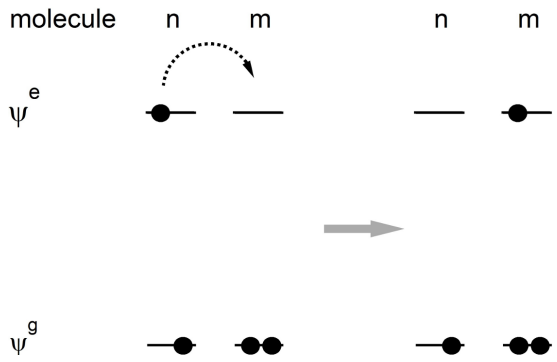

Figure 2.4: Illustration of the electron transfer mechanism from molecule n to molecule m. Molecule n is in an excited state, where one electron was promoted from the ground state with a wave function ψ_n^g to the primarily unoccupied state with a wave function ψ_n^e. The dotted black arrow indicates the electron transfer into the primarily unoccupied state with a wave function ψ_m^e, of molecule m. After the initial excitation, molecule n is positively charged and molecule m is negatively charged.

long-range Coulomb interaction between transition dipole moments. For closely packed and face-to-face stacked π-conjugated molecules, adjacent dyes can have a considerable wave function overlap between their frontier orbitals [7,55–61]. Such an overlap increases exponentially with decreasing intermolecular distance. For example, for naphthalene dimers, the short-range component of the electronic coupling becomes significant at a separation of about 6 Å [34, 62]. This can lead to intermolecular charge transfer (CT) between adjacent molecules [63–67]. The character of the thus created electron-hole pairs, either weakly or strongly bound, depends on the distance between the two charge carriers. At a certain distance between the electron-hole pair, CT states can bridge the gap between so-called Frenkel excitons, i.e. bound excitons located at a single molecule, and weakly bound electron-hole pairs (large distance between charge carriers).

From the extent of the overlap of the molecular orbitals one can evaluate the CT states and estimate the CT transition dipole moment of such a CT configuration. The precise calculation is most challenging [60, 61, 68–71]. Here, I can only estimate, for a very simple two-level system, the possible contribution for closely packed and face-to-face stacked aromatic dyes.

The model system consists of two molecules with two energetic states each. The exchange of a single electron between molecule n and m is depicted in Fig. 2.4. For the sake of simplicity, the wave function, π, is restricted to the electronic

part. The ground-state and excited-state wave functions are denoted as ψ_n^g and ψ_n^e and ψ_m^g and ψ_m^e for molecules n and m, respectively. Like in Chapter 2.1, I will construct $\pi_{n,m}$ as a Hartree product wave function. The use of a Slater determinant guarantees the antisymmetry.

$$\begin{aligned}\pi_{n,m} &= \frac{1}{\sqrt{2}}\begin{vmatrix}\psi_n(\vec{r'}_n,\vec{r}_n) & \psi_m(\vec{r'}_m,\vec{r}_n)\\ \psi_n(\vec{r'}_n,\vec{r}_m) & \psi_m(\vec{r'}_m,\vec{r}_m)\end{vmatrix}\\ &= \frac{1}{\sqrt{2}}\{\psi_n(\vec{r'}_n,\vec{r}_n)\psi_m(\vec{r'}_m,\vec{r}_m)-\psi_n(\vec{r'}_n,\vec{r}_m)\psi_m(\vec{r'}_m,\vec{r}_n)\},\end{aligned} \tag{2.22}$$

where $\vec{r}_n$ and $\vec{r}_m$ are the coordinates of the single electron which can be exchanged between molecules n and m. The coordinates $\vec{r'}_n$ and $\vec{r'}_m$ refer to the remaining coordinates of the molecule. For the exchange of one electron from molecule n to m follows

$$\begin{aligned}&\left\langle \pi_{n_g,m_e}\left|V_{nm}\right|\pi_{n_e,m_g}\right\rangle =\\ &\int d^3r_n d^3r_m \frac{1}{\sqrt{2}}\left(\psi_n^{g*}(\vec{r'}_n,\vec{r}_n)\psi_m^{e*}(\vec{r'}_m,\vec{r}_m)-\psi_n^{g*}(\vec{r'}_n,\vec{r}_m)\psi_m^{e*}(\vec{r'}_m,\vec{r}_n)\right)\\ &\times V_{nm}\frac{1}{\sqrt{2}}\left(\psi_m^{g}(\vec{r'}_m,\vec{r}_m)\psi_n^{e}(\vec{r'}_n,\vec{r}_n)-\psi_m^{g}(\vec{r'}_m,\vec{r}_n)\psi_n^{e}(\vec{r'}_n,\vec{r}_m)\right).\end{aligned} \tag{2.23}$$

Here, the Coulomb coupling, i.e. transition dipole-dipole coupling (see Chapter 2.1), is modified by the terms $\psi_n^{g*}(\vec{r'}_n,\vec{r}_m)\psi_m^{e*}(\vec{r'}_m,\vec{r}_n)$ and $\psi_m^{g}(\vec{r'}_m,\vec{r}_n)\psi_n^{e}(\vec{r'}_n,\vec{r}_m)$. Due to the electron exchange, the wave functions $\psi_m^g(\vec{r'}_m,\vec{r}_n)$ and $\psi_n^e(\vec{r'}_n,\vec{r}_m)$ also depend on $\vec{r}_n$ and $\vec{r}_m$.

Mulliken investigated the charge transfer for molecular compounds and charge transfer complexes in great detail and determined the CT transition moment for σ-type overlap [63,72]. He used following expression to evaluate the CT transition moment [73]:

$$\vec{\mu}_{n,m} = -e\left\langle \pi_{n_g,m_e}\left|\vec{r}\right|\pi_{n_e,m_g}\right\rangle \tag{2.24}$$

$$\rho_{n,m}(\vec{r}) = \pi_{n_g,m_e}(\vec{r})\pi_{n_e,m_g}(\vec{r}) \tag{2.25}$$

and

$$\vec{\mu}_{n,m} = -e\int d^3r\ \vec{r}\times\rho_{n,m}(\vec{r}), \tag{2.26}$$

where $\rho_{n,m}$ is the transition density. For σ-type overlap, Mulliken approximated the CT transition moment, $\vec{\mu}_{n,m}$, with

$$-e\int d^3r\ \vec{r}\times\rho_{n,m}(\vec{r}) \approx -e\vec{R}_{n,m}\int d^3r\rho_{n,m}(\vec{r}) = -e\vec{R}_{n,m}\left\langle \pi_{n_g,m_e}|\pi_{n_e,m_g}\right\rangle, \tag{2.27}$$

where $\vec{R}_{n,m}$ is the average position of the transition density. For a σ-type overlap, the transition density is located between the two molecules [73, 74]. The vector $\vec{\mu}_{n,m}$ is aligned parallel to the connecting line of molecules n and m.

About 20 years ago, people started to investigate and combine the effects of molecular orbital overlap and Förster transition dipole-dipole coupling [34,35,62]. Nevertheless, the exact mechanism and its relevance for closely packed and coherently coupled molecules is still fervently discussed [56, 60, 61, 75–79]. In Chapter 5.2 I will contribute to this discussion and present experimental results which suggest that the wave function overlap might significantly contribute to coherent interaction between molecules at a short distance.

2.2 Film growth and kinetics

The growing interest in organic thin films results to a large extent from the increasing implementation of organic electronics in high-tech end consumer products [80, 81]. The performance of such devices is not only related to the chemical structure of the molecules but also to the structural characteristics of the thin film. To further optimize and improve the device control, a better understanding of growth and post-growth behavior is mandatory.

The growth and post-growth kinetics of molecular films can be quite different from their inorganic counterparts. For organic thin films, also the molecular orientation and the internal degrees of freedom of molecules play a crucial role in thin-film growth. Depending on the orientation and the often anisotropic shape of molecules, their diffusion coefficient can vary over a wide range [12–16, 82]. In addition, intermolecular attraction or repulsion between adjacent dyes but also interaction and charge transfer between molecules and the substrate surface affects the growth and post-growth. This can lead to multiple thermal diffusion pathways, unexpected transient phases [83], and various different film structures and morphologies, depending on the preparation parameters or post-growth treatment. Real-time studies of such systems could reveal important steps in growth and post-growth behavior [24].

2.2.1 Thermodynamics and kinetics

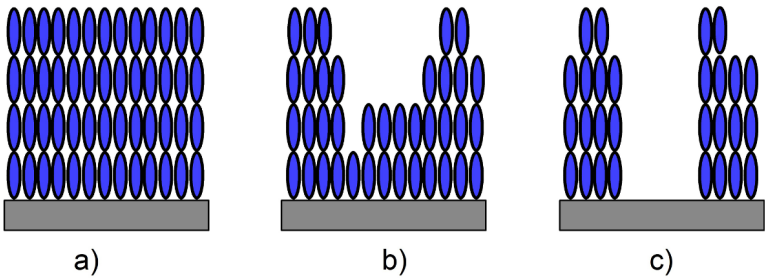

Figure 2.5: Illustration of different thin-film growth modes. a) Frank-van der Merwe (layer-by-layer), b) Stranski-Krastanov (layer-plus-island), and c) Volmer-Weber (island formation). See text for discussion.

The growth of atomic or molecular vapor-deposited films occurs far from thermal equilibrium and is governed by the competition between thermodynam-

ics and kinetics [23]. At thermal equilibrium, the shape of a crystal is determined by the surface tension, γ, which is defined as the reversible work necessary for creating a unit area of new surface. Thus, for the surface tension follows

$$\gamma = \lim_{dA \to 0} \left(\frac{dW}{dA} \right) = \left(\frac{dF}{dA} \right)_{T,V}, \tag{2.28}$$

where W is the reversible work, A the area of the crystal, and F the free energy. At equilibrium and, thus, constant temperature and volume, dF is 0 and the total energy of the system integrated over the entire surface area of the crystal,

$$\int \gamma dA, \text{ reaches a minimum.} \tag{2.29}$$

In this terminology, Bauer et al. classified three primary film growth processes during the deposition of a material A on a substrate B [23, 84, 85]. The three fundamental growth modes are:

- Frank-van der Merwe growth (layer-by-layer)
- Stranski-Krastanov growth (layer-plus-island)
- Volmer-Weber growth (island formation),

and illustrated in Fig. 2.5.

Which growth mode of atomic or molecular vapor-deposited films will be dominant depends on the interaction strength among deposited atoms or molecules, and on the interaction strength between deposited atoms or molecules and the substrate surface. If the atoms or molecules are more attracted to each other than to the substrate surface, the film will grow in islands, as illustrated in Fig. 2.5 c). If the interaction between atoms or molecules and the substrate surface is stronger, the film will grow layer by layer (Fig. 2.5 a)). Stranski-Krastanov growth represents an intermediate case: at first, the film grows in a layer-by-layer fashion but at a critical film thickness, island formation sets in (Fig. 2.5 b)).

In terms of surface tension, Bauer concluded for layer-by-layer growth that

$$\gamma_A + \gamma_{\text{int}} < \gamma_B, \tag{2.30}$$

where γ_A is the surface tension of material A, γ_B the surface tension of the substrate B, and γ_{int} the surface tension of the interface, which represents the excess surface tension integrated over the interfacial region of bulk A and B. Equation

2.29 leads to the conclusion that the energy of the total system will be minimized and, therefore, the surface of A will be maximized whereas the bare surface of B will be minimized. If the interfacial tension γ_{int} increases with increasing film thickness, for example due to strain in this layer, and

$$\gamma_A + \gamma_{\text{int}} > \gamma_B \tag{2.31}$$

at a critical film thickness the growth will continue in a 3D fashion. Here, the surface of A will be minimized whereas the bare surface of B will be maximized. For island formation, equation 2.31 is already fulfilled for the first layer.

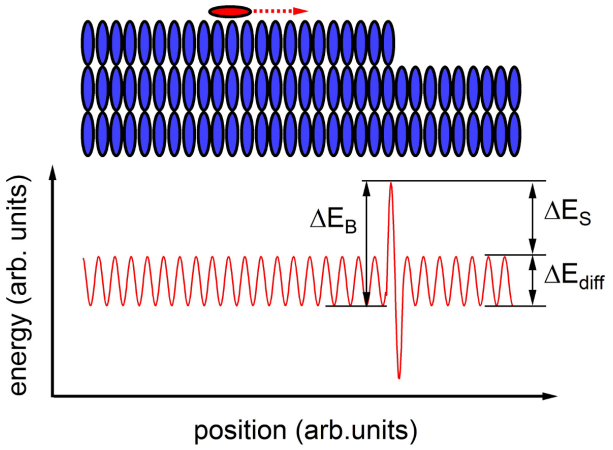

Figure 2.6: Energies associated with the diffusion (E_{diff}) and crossing over a step edge (E_{S}) with an energy barrier (E_{B}) of a molecule on top of an organic film.

In a microscopic picture, the growth mechanism is often explained with rate equation models where the interlayer diffusion of the molecule and additional energy barriers at step edges determine the growth mode and the shape of the islands [13, 14, 86]. If the interlayer mass transport is sufficiently high, the film will grow in a layer-by-layer fashion. For many inorganic and organic systems it was observed that atoms or molecules were reflected by the additional energy barrier at the step edges. This so-called Ehrlich-Schwoebel barrier can hinder the interlayer mass transport and promotes the formation of islands. Fig. 2.6 illustrates the energy barrier at a step edge of an organic multilayer film. Here, the Ehrlich-Schwoebel barrier is defined as

$$E_S = E_B - E_{\text{diff}}, \tag{2.32}$$

where E_B is the energy barrier at the step edge and E_{diff} the diffusion barrier. The rate with which molecules can diffuse downwards at a step-edge depends on the height of the Ehrlich-Schwoebel barrier and is proportional to $v \propto e^{-\frac{E_S}{k_B T}}$. The jump rate of molecules on a single terrace is proportional to $v' \propto e^{-\frac{\text{diff}}{k_B T}}$, where E_{diff} is the energy barrier for the diffusion on the initial layer. The combination of both leads to the interlayer jump rate [26]

$$v_{\text{rate}} \propto \; e^{-\frac{E_S}{k_B T}} \; e^{-\frac{E_{\text{diff}}}{k_B T}}. \tag{2.33}$$

For organic systems, the barrier height itself strongly depends on the molecular structure and conformation but also on the attractive intermolecular interaction between the diffusing molecule and the organic film [26]. For the class of conjugated molecules, all three fundamental growth modes were observed. Typically, the Ehrlich-Schwoebel barrier is in the order of 0.5–1 eV. The diffusion activation energy is usually between 10 meV and 100 meV, depending on the substrate roughness and layer thickness [26, 82, 87, 88].

2.2.2 Kolmogorov-Johnson-Mehl-Avrami kinetic model

During a phase transition, atoms or molecules rearrange in order to attain the energetically most favorable configuration. A phase change and the post-growth behavior depend on a wide variety of parameters. Some kinetic parameters, e.g. the activation energy of a phase transition, are often deduced from spectroscopic or microscopic measurements of the transformed volume fraction during a phase change as a function of time. In Chapter 5.3, the transformed volume fraction will be determined with time-dependent X-ray absorption measurements. The observed characteristic intensity evolution can be best explained with the Kolmogorov-Johnson-Mehl-Avrami (KJMA) model [89–92].

The KJMA model has proven very successful for modeling the isothermal crystallization of amorphous materials, polymers, metals and metal alloys [93–97]. The model describes a first-order phase transition in which nucleation is modeled by a spatial Poisson process. The phase transition occurs in a finite volume, but the system is much larger than the distance between two nuclei within the transformed volume. Under these assumptions, the transformed volume fraction can be expressed as a function of time and from this a number of kinetic parameters,

e.g. the activation energy of a particular phase change, can be extracted.

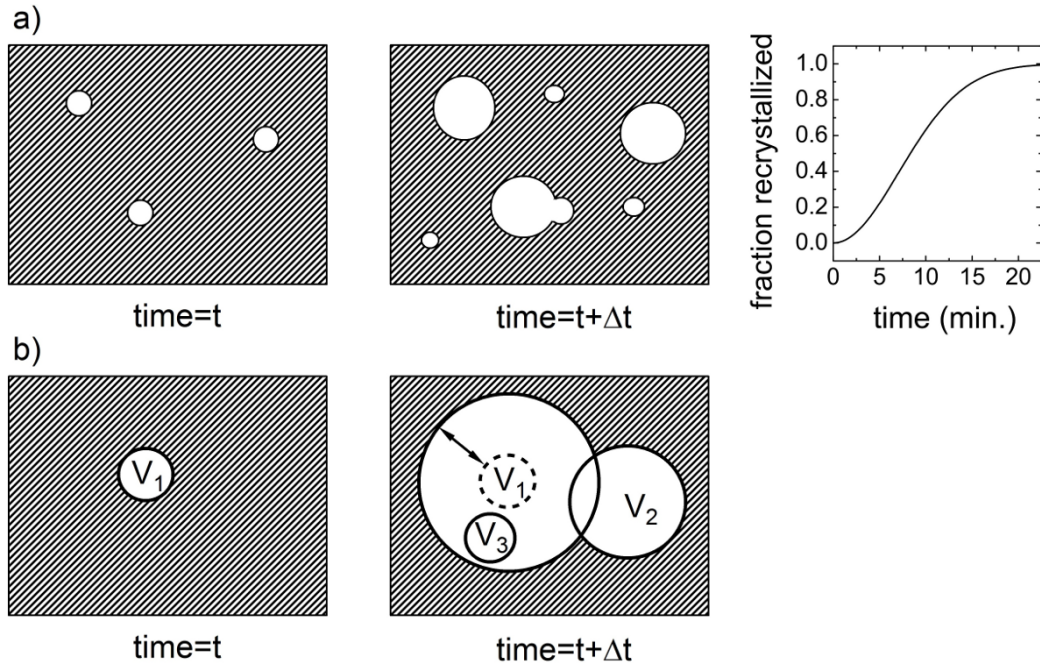

Figure 2.7: Illustration of phase transformation according to the KJMA model. At time = t, the initial phase has been transformed at some locations. The curve on the right-hand side shows the time evolution of the transformed volume fraction. The initial phases are represented by shaded areas and the transformed phases are represented by white areas. See text for details.

A typical isothermal nucleation process is illustrated in Fig. 2.7 a). At time = t, the initial phase has been transformed at three random positions (white area). After some time, t+Δt, more of the initial phase has been transformed. The time evolution of the transformed volume fraction follows an s-shaped curve, i.e. a sigmoidal function (Fig. 2.7 a)). For the KJMA model, Avrami introduced the extended volume [90–92], or *phantom nuclei*, concept. It states, that the (fictitious) nucleation occurs at spatially random positions within transformed as well as untransformed regions. The *phantom* volume denotes the transformed volume each nucleus would have if its growth were not affected by other nuclei.

In Fig. 2.7 b), this concept is illustrated. After some time, at t+Δt, area V_1 has grown and areas V_2 and V_3 are newly transformed. Since $V_1 \cap V_2$ and V_3 are located in already transformed regions, they are also referred to as *phantom* volume.

The *phantom* volume contributes to the extended volume fraction. In particular, the extended volume accounts for all transformations without consideration of impingement and pre-existing nucleation.

To obtain an analytical expression and to solve the impingement, Avrami distinguishes between the extended volume fraction $f_{\text{ext}}(t)$ and the transformed volume fraction $f(t)$, which are defined as follows

$$f_{\text{ext}}(t) = \frac{V_1(t) + V_2(t)}{V_{\text{total}}(t)} \quad \text{and} \quad f(t) = \frac{V_1(t) \cup V_2(t)}{V_{\text{total}}(t)},$$

where $V_1(t)$ and $V_2(t)$ are transformed volume fractions as illustrated in Fig. 2.7 b).

In the KJMA theory, the nucleation is spatially and temporally uniform. The probability of the extended volume fraction is expressed by Poisson's distribution

$$P_n(t) = \frac{[f_{\text{ext}}(t)]^n}{n!} e^{-f_{\text{ext}}(t)}. \tag{2.34}$$

With the probability of the untransformed volume fraction, expressed by $P_0(t) = e^{-f_{\text{ext}}(t)}$, follows for the transformed volume fraction

$$f(t) = 1 - e^{-f_{\text{ext}}(t)}. \tag{2.35}$$

In the KJMA model, the transformed volume fraction is often expressed by the following equation

$$f(t) = 1 - e^{-kt^n}, \tag{2.36}$$

where k is the temperature-dependent reaction rate constant, t the time, and n the Avrami exponent. The Avrami exponent itself is often written as follows

$$n = a + bc. \tag{2.37}$$

Fig. 2.8 shows the transformed volume fraction, $f(t)$, for Avrami exponents $\mathrm{n} = 2, 3$, and 4, respectively, as a function of time and at constant reaction rate. The larger the Avrami exponent, the steeper the slope of the sigmoidal function and the faster the phase transformation progresses. At constant nucleation rate and phase boundary-controlled growth, Avrami exponents of $\mathrm{n} = 2, 3$ or 4 are originally interpreted as 1D, 2D, or 3D growth, respectively. Nevertheless, the analysis and interpretation of experimental data is most challenging as n can

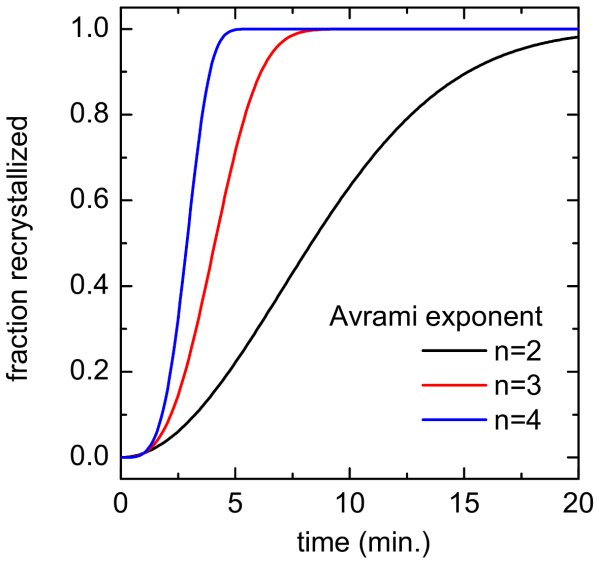

Figure 2.8: Transformed volume fraction as a function of time and according to the KJMA model. The transformed volume fraction was calculated for various Avrami exponents. The reaction rate was held constant.

vary with time and non-integer and abnormally low values are reported in the literature [98–102]. Some of the most common physical interpretations of the Avrami exponents are summarized in table 2.1 [103].

Assuming that the rate constant k shows a Arrhenius temperature dependency,

$$k = k_0 \cdot e^{-\frac{E_{act}}{k_B T}}, \tag{2.38}$$

with k_0 being the frequency factor, E_{act} the activation energy, and k_B Boltzmann's constant. The frequency factor describes the total number of collisions per second which result in a specific reaction, whereas the probability for a reaction is governed by the exponential term, $e^{-\frac{E_{act}}{k_B T}}$. With $g(f(t)) \equiv n(1-f(t))\left[(-\ln(1-f(t))\right]^{\frac{n^2-1}{n}}$ and the time derivative of Equation 5.15, this leads to the expression

$$\ln\left(\frac{df(t)}{dt}\right) = \ln\left[k_0\ g(f(t))\right] - \frac{E_{act}}{k_B T}. \tag{2.39}$$

For an Arrhenius temperature dependency, we obtain a straight line in a plot of $\ln\left(\frac{df(t)}{dt}\right)$ against the inverse temperature. From the slope of this line we can extract the activation energy and from the intersection point of the line and the

y-axis, i.e. $\ln\left(\frac{df(t)}{dt}\right)$-axis, the frequency factor for the nucleation process can be obtained.

Table 2.1: Interpretation of the Avrami exponent of the form n=a+bc. See text for discussion.

a=0	zero nucleation rate
a=1	constant nucleation rate
a>1	increasing nucleation rate
0<a<1	decreasing nucleation rate
b=3	3D growth
b=2	2D growth
b=1	1D growth
c=1/2	diffusion controlled growth
c=1	phase-boundary controlled growth

3

Theoretical background of X-ray absorption

3.1 X-ray absorption spectroscopy

X-ray absorption spectroscopy (XAS) is a powerful tool for investigations on electronic properties and local atomic order but also on the geometric orientation of surface adsorbates [104]. Normally, XAS experiments were performed by stepping the photon energy and measuring the signal of a secondary process (e.g. Auger decay) which is assumed to be proportional to the absorption cross section.

In Fig. 3.1, the XAS process for a diatomic molecule is depicted. Usually, we distinguish between at least two different regions in the XAS spectra. At sufficient high X-ray photon energy, an inner-shell electron can be excited above the ionization threshold and emitted as a photoelectron. The electron wave function of this photoelectron interferes with itself when it is back-scattered by neighboring atoms. In a XAS spectrum, this results in a series of oscillations from which information about the local coordination environment of the investigated element can be gathered.

In this work, I will investigate the electronic properties and spatial orientation of condensed molecular films with X-ray absorption normally measured at some eV below the ionization threshold. In such measurements, often referred to as near-edge X-ray absorption fine-structure (NEXAFS), sharp and distinct features at the C K-edge of molecular films of aromatic molecules can be observed. These absorption peaks arise if the photon energy is lower than the ionization energy but sufficiently high to excite a core electron into an unoccupied lowest-energy molecular orbital. In Fig. 3.1 such an initially unoccupied orbital is denoted by $1\pi^*$. The position and shape of the absorption peaks are very sensitive to the chemical structure of the individual molecule but also to charge transfer to the substrate surface, as well as electronic interactions with neighboring molecules [19, 83, 105].

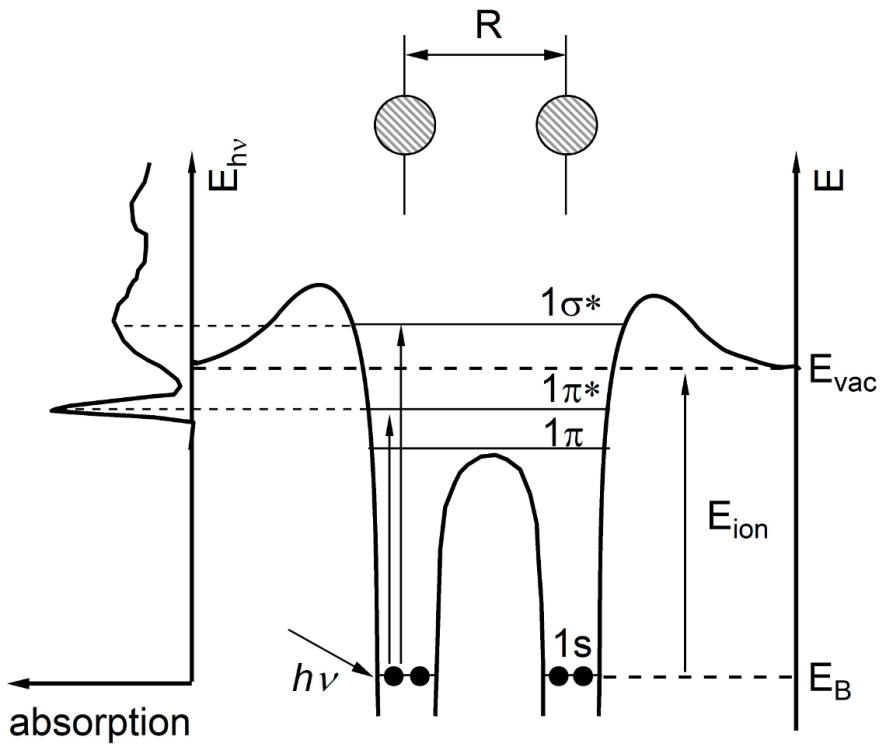

Figure 3.1: Illustration of the XAS process for a diatomic molecule. Core electrons with a binding energy E_B are excited into the π^* and σ^* orbitals. The asterisk indicates an initially unoccupied molecular orbital. The resulting absorption spectrum for such a core-valence excitation is plotted on the left-hand side.

The core-valence excitation is followed by two competing processes: Auger decay and radiative fluorescence decay. For measurements of carbon-based molecules and at the C *K*-edge, the Auger decay is the dominant relaxation process [104]. After core-valence excitation, the core hole in the *K*-shell is filled by an electron from the *L*-shell. In this process, another *L*-shell electron is emitted. The emitted Auger electrons can be measured by the so-called Auger electron yield (AEY) method. AEY measurements have a very high chemical selectivity since only Auger electrons with a specific kinetic energy (e.g. about 255 eV for C *KLL*-Auger electrons) will be counted. Also, it is a very surface-sensitive method since the mean free path of an emitted Auger electron is only about 1 nm [106]. For a detailed discussion of different detection methods see Reference [104].

The probability per unit time, P_{if}, for the transition from an initial state, $|\Psi_i\rangle$, to a final state, $|\Psi_f\rangle$, with the energetic difference $E_{if} = E_i - E_f$ between the two states is governed by Fermi's Golden rule [107]:

$$P_{if} \sim \left|\left\langle \Psi_f \left| \hat{H}' \right| \Psi_i \right\rangle\right|^2 \delta(\hbar\omega - E_{if}) = |M_{if}|^2 \, \delta(\hbar\omega - E_{if}), \tag{3.1}$$

with $M_{if} = \langle \Psi_f \left| H' \right| \Psi_i \rangle$ being the transition matrix elements and the delta function providing energy conservation. The perturbing Hamiltonian H' in Equation 3.1 is given by

$$\hat{H}' = \frac{e}{2mc}(\hat{A}\cdot\hat{p} + \hat{p}\cdot\hat{A}) - e\phi + \frac{e^2}{2mc^2}A^2, \tag{3.2}$$

with $\hat{A}$ and ϕ being the vector and scalar potentials of the incident light field, respectively, and $\hat{p} = -i\hbar\vec{\nabla}$ being the momentum operator. If two-photon processes are neglected and the quadratic term A^2 is dropped, we obtain with the dipole approximation for the vector potential, $\hat{A}(t,\vec{r}) \rightarrow \hat{A}(t)$, and the gauge $\phi = 0$:

$$\hat{H}' = \frac{e}{mc}\left(\hat{A}\cdot\hat{p}\right). \tag{3.3}$$

In the following, I will apply several approximations to equation 3.1 and concentrate on some aspects of the NEXAFS process which are relevant in this work. Within the so-called *sudden approximation* in NEXAFS, it is assumed that the excited core electron has little effect on the remaining ground state electrons. Therefore, we can define the following wave function

$$\Psi_f = \hat{C}\Phi_f^k \psi_f^{k,\mathrm{ion}}(N-1), \tag{3.4}$$

in which the wave function of the excited and "active" electron, Φ_f^k, can be separated from that of the remaining and 'inactive' electrons which is denoted by $\psi_f^{k,\mathrm{ion}}(N-1)$. The operator $\hat{C}$ ensures the antisymmetry of the wave function. Within the dipole approximation (i.e. $\vec{k}\vec{r} \ll 1$), which is valid in the soft X-ray regime and especially at the C K-edge and $h\nu \approx 285\,\mathrm{eV}$, the following expression for the transition dipole matrix elements can be obtained:

$$\begin{aligned} M_{if} &= \langle \Psi_f \left| \vec{e}\cdot\hat{p} \right| \Psi_i \rangle = \left\langle \Psi_f(N) \left| \vec{e}\sum_{k=1}^{N}\hat{p_k} \right| \Psi_i(N) \right\rangle \\ &= \left\langle \Phi_f^1 \left| \vec{e}\cdot\hat{p}_1 \right| \Phi_i^1 \right\rangle \left\langle \psi_f^{\mathrm{ion}}(N-1) | \psi_i^{\mathrm{ion}}(N-1) \right\rangle \cdots . \end{aligned} \tag{3.5}$$

If Koopman's theorem [108] holds true for the wave functions of the "inactive" ground state electrons (equation 3.4), the expression above can be simplified even further. In the so-called *frozen-orbital approximation*, we assume that the

orbitals of the "inactive" electrons remain unchanged and thus "frozen", i.e. $\left\langle \psi_f^{k,\mathrm{ion}}(N-1) | \psi_i^{k,\mathrm{ion}}(N-1) \right\rangle = 1$. For the transition dipole matrix elements the following equation is valid:

$$M_{if} = \langle \Psi_f \left| \vec{e} \cdot \hat{p} \right| \Psi_i \rangle = \left\langle \Phi_f^1 \left| \vec{e} \cdot \hat{p} \right| \Phi_i^1 \right\rangle . \tag{3.6}$$

In this simplest expression for M_{if}, the transition matrix elements are reduced to one-electron elements and all effects due to orbital relaxation or electron correlation are ignored. Thus, the energy of an absorption is the difference of the Koopman's binding energies of the core electron initial state and final state. Although this theoretical description of the NEXAFS process might be oversimplified and in actual NEXAFS measurements satellite peaks resulting from multi-electron processes were reported [109–111], equation 3.6 illustrates the local character of X-ray absorption measurements. The transition dipole matrix elements in equation 3.6 only depend on the initial core electron state Φ_i and the resulting valence state Φ_f. If a molecule consists of chemically different carbon atoms (e.g. due to different binding partners), NEXAFS can selectivity probe a particular core-valence transition.

The optical oscillator strength f is a dimensionless quantity and related to the transition dipole matrix elements as follows [104]:

$$f \sim |\langle \Psi_f \left| \vec{e} \cdot \hat{p} \right| \Psi_i \rangle|^2 = |M_{if}|^2. \tag{3.7}$$

Through this quantity we can connect the square of the transition dipole matrix elements with the X-ray absorption cross section:

$$\sigma_x(E) = C \frac{df}{dE}, \tag{3.8}$$

with $C = \frac{2\pi^2 e^2}{\hbar} = 1.1 \cdot 10^2\,\mathrm{Mb\,eV}$. Due to the scalar product $\vec{e} \cdot \hat{p}$ in equation 3.2, the cross section σ_x shows an angular dependency. This can be utilized to determine the symmetry and orientation of adsorbed molecules with respect to the substrate surface. The transition dipole matrix elements in equation 3.7 are non-zero only if they are totally symmetric or contain a totally symmetric component. This implicates that for non-zero matrix elements at a given polarisation of the light, the initial state Ψ_i and final state Ψ_f have to be of a particular symmetry, which I will demonstrate for the initial state $1s$ and final state $2\pi^*$ of NTCDA. The symmetry classification of orbitals can be determined by group theoretical

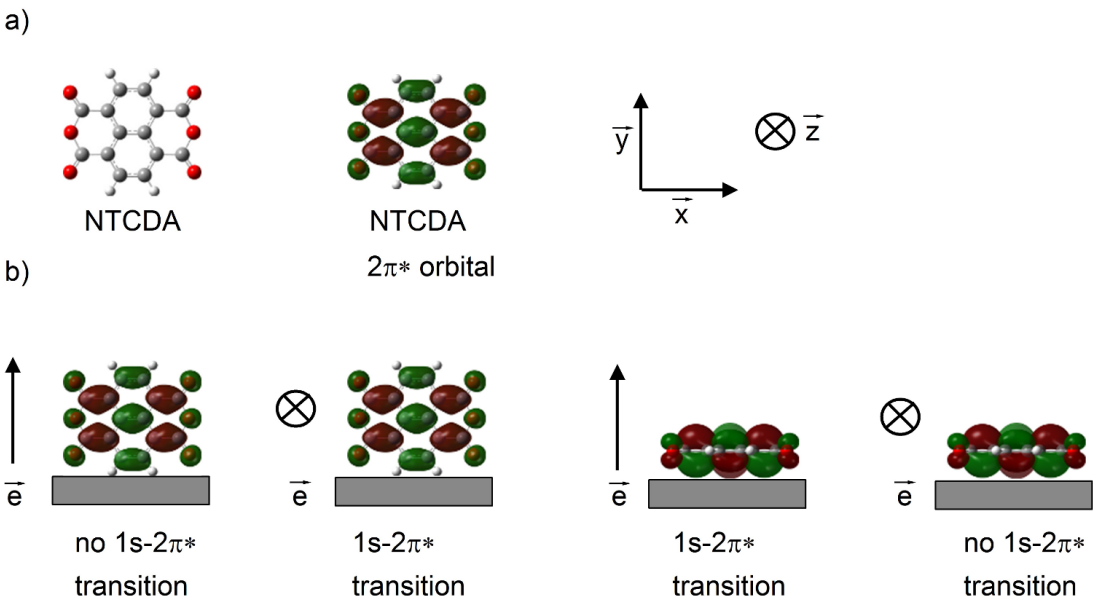

Figure 3.2: Symmetry properties of the NEXAFS process. a) Free NTCDA molecule and the $2\pi^*$ molecular orbital. b) Adsorbed NTCDA molecule and $2\pi^*$ molecular orbitals for different orientations towards the surface. Depending on the molecular orientation and polarisation of the light, the $1s$-$2\pi^*$ transition is either allowed or forbidden.

methods. For a detailed discussion of molecular symmetry classification see References [104, 112–114].

In Fig. 3.2 b), the dependency of the $1s$-$2\pi^*$ transition of NTCDA on its orientation towards the substrate surface is illustrated. At a given polarisation of the light, a C 1s core electron with s-orbital character is excited into the initially unoccupied molecular orbital $2\pi^*$ which has p_z-orbital character and is oriented parallel to the y-z-plane, see Fig. 3.2 a). For molecules standing perpendicular to the substrate surface (3.2 b), left-hand side), the transition dipole matrix elements are zero for light polarized in $\vec{y}$-direction and non-zero for light polarized in $\vec{z}$-direction. In contrast, for molecules oriented parallel to the substrate surfaces (Fig. 3.2 b), right-hand side), the transition dipole matrix elements are non-zero for light polarized in $\vec{y}$-direction and zero for light polarized $\vec{z}$-direction.

If the molecules are oriented at a different angle with respect to the surface substrate, as illustrated in Fig. 3.3, the absorption cross section and hence also the intensity of the NEXAFS signal changes accordingly. The orientation of the ad-

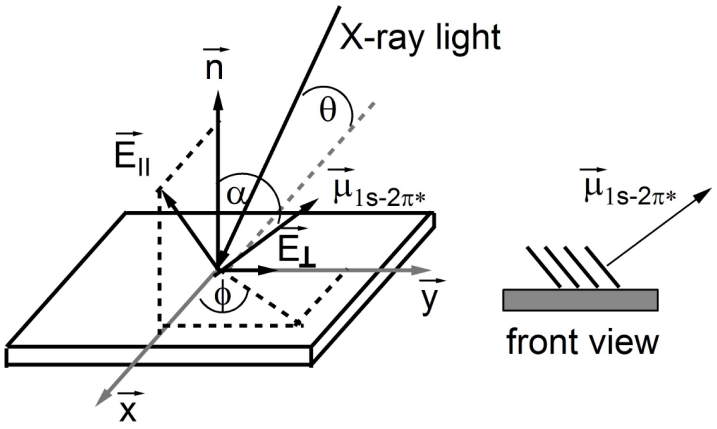

Figure 3.3: Angles relevant for the determination of the orientation of an adsorbed molecule with respect to the substrate surface and surface normal. The $1s$–$2\pi^*$ transition dipole moment, $\vec{\mu}_{1s-2\pi^*}$, is orientated perpendicular to the molecular plane. The molecule itself is tilted at an angle α with respect to the surface normal $\vec{n}$.

sorbed molecules can be determined from the intensity ratio of some core-valence transitions for different polarisations of the incident light. Alternatively, we can collect the NEXAFS signal at a fixed polarisation but at different angles Θ, where Θ is defined according to Fig. 3.3 as the angle between the incident X-ray light and the substrate surface. With the following expression for the angular dependent NEXAFS intensity, $I_{\parallel}(\Theta, \varphi)$ and $I_{\perp}(\Theta, \varphi)$ for parallel and perpendicularly polarized light (see also Fig. 3.3) [104], respectively, we can calculate any arbitrary molecular orientation within ordered films:

$$I_{\parallel}(\Theta, \alpha) = \frac{1}{3}\left[1 + \frac{1}{2}\left(3\cos^2\Theta - 1\right)\left(3\cos^2\alpha - 1\right)\right] \tag{3.9}$$

$$I_{\perp}(\alpha) = \frac{1}{2}\sin^2\alpha \tag{3.10}$$

The angles Θ and α are defined according to Fig. 3.3. These expressions were derived for substrates with three-fold or higher symmetry. On such a substrate surface, aromatic molecules typically grow in multiple domains. Therefore, an average over the azimuthal angular variation ϕ is calculated.

3.2 Vibronic excitation

With NEXAFS, not only the transition of a core electron into an unoccupied state is probed but also the vibrational energy levels. It is assumed that the electronic-vibrational (or electron-phonon) coupling during a core-valence transition is described by the Franck-Condon principle. This assumption is valid, if one can apply the Born-Oppenheimer approximation [115] and separate the total wave function into its electronic, $\pi(\vec{r})$, and nuclear, $\chi(\vec{R})$, components:

$$|\psi\rangle = |\pi\rangle \times |\chi\rangle. \tag{3.11}$$

Within the Franck-Condon framework, the Condon approximation is even more restrictive than the Born-Oppenheimer approximation since the nuclear position is fixed for the duration of a transition. This means that an electronic transition from a ground state into an excited state is so fast in comparison to the nuclear motion that the molecular degrees of freedom are frozen during the core-valence excitation [116–118].

Fig. 3.4 illustrates the NEXAFS process for a diatomic molecule. In a simple approximation, the potential energy curves of the ground and excited states are approximated by harmonic potentials. The potential curves of the excited states, i.e. AB* and AB**, are displaced from the equilibrium position of the electronic ground potential by $\Delta R'$ and $\Delta R''$, respectively. The amount of this displacement depends on the nature of the ground and excited molecular orbitals. If the bond character of the ground and excited states is similar, the displacement is smaller than for a very different bonding character of the two states.

In Fig. 3.4, the potential energy curve for a non-bonding orbital of the electronic state AB* is shown. Here, the displacement is smaller than for the potential energy curve for an anti-bonding orbital of the state AB**. For the electronic states AB and AB* follows for the potential energy curves:

$$V_{AB}(R) = \frac{h\nu R_0^2}{2} \quad \text{and} \tag{3.12}$$

$$V_{AB^*}(R) = \Delta E_a + \frac{h\nu(R_0 - \Delta R')^2}{2}, \tag{3.13}$$

where ν is the vibrational frequency, $\Delta R'$ the displacement of the potential energy curve AB*, and ΔE_a the adiabatic energy difference between initial and

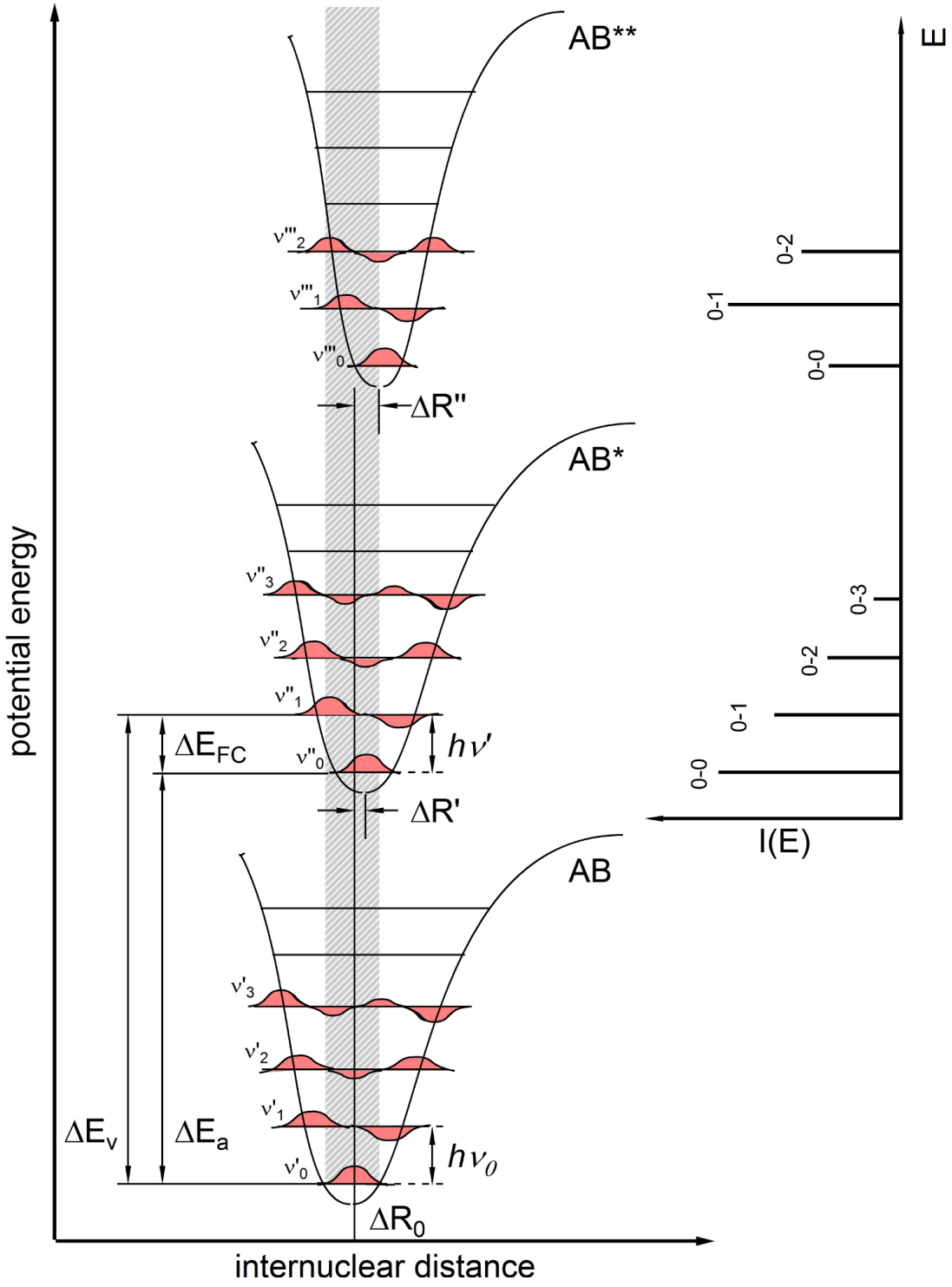

Figure 3.4: Franck-Condon principle illustrated with potential energy curves of a diatomic molecule AB. The electronic states AB, AB*, and AB** and the vibronic excitation in the NEXAFS process are shown.

excited state. With equations 3.12 and 3.13 for the potentials, the wave function illustrated in Fig. 3.4 and the eigen-energies can be calculated according to

$$E_{\mathrm{vib,m}} = h\nu_0(m + \frac{1}{2}), \tag{3.14}$$

with the quantum number $m = 0 \cdots \infty$ with respect to the ground vibronic state of the corresponding potential energy surface. From the position of the minima of the potential energy curves, i.e. the displacements $\Delta R'$ and $\Delta R''$, the coupling strength of the electron with molecular vibrations can also be derived. The electronic-vibrational (or electron-phonon) coupling is often quantified by the Huang-Rhys factor [119] which is given by

$$S = \frac{\Delta R^2}{2}, \tag{3.15}$$

where ΔR is the equilibrium displacement.

On the right-hand side of Fig. 3.4, an absorption spectrum is shown. The shape of the spectrum, i.e. the intensity ratio of the adiabatic transition (0-0) and corresponding vibronic progression (0-1, 0-2, 0-3, etc.), depends on the overlap of the vibronic ground state wave function of the inital state with the vibronic wave functions of the excited states. For the probability P_{ge} per unit time follows:

$$P_{ge} \sim |\langle\psi^e|\vec{e}\cdot\hat{p}|\psi^g\rangle|^2\,\delta(h\nu - E_a - E_{\mathrm{vib,m}}) \tag{3.16}$$

$$P_{ge} \sim |\langle\pi^e|\vec{e}\cdot\hat{p}|\pi^g\rangle|^2 \cdot |\langle\chi^e|\chi^g\rangle|^2\,\delta(h\nu - E_a - E_{\mathrm{vib,m}})$$

$$P_{ge} \sim |M_{ge}|^2 \cdot \underbrace{|\langle\chi^e|\chi^g\rangle|^2}_{\text{FC factor}} \cdot \delta(h\nu - E_a - E_{\mathrm{vib,m}}). \tag{3.17}$$

Since $\vec{e}\cdot\hat{p}$ only affects $|\pi\rangle$ of the total wave function, P_{ge} can be expressed in terms of the transition matrix elements $|M_{ge}|$, the Franck-Condon factor $|\langle\chi^e|\chi^g\rangle|^2$, and a delta function which ensures the energy conservation during the whole process.

In the Chapters 5.2 and 5.3, organic thin films in a temperature range between 180–240 K are investigated. The correspondent thermal energy kT is in the order of 15–20 meV and, thus, much smaller than $h\nu{\sim}100$ meV. Therefore, it can be assumed that the molecules are initially in their vibronic ground state and, for harmonic oscillator potential energy curves, small displacements, and without second-order coupling terms, the Franck-Condon factors follow a Poisson distribution [120]:

$$I_{\mathrm{abs}} \sim \exp^{\frac{\Delta E_{FC}}{E_{\mathrm{vib}}}} \sum_{n=0}^{\infty} \left(\frac{(\Delta E_{FC}/E_{\mathrm{vib,m}})^n}{n!} \right) \delta(h\nu - E_a - E_{\mathrm{vib,m}}), \tag{3.18}$$

where ΔE_{FC} is the energy difference between the adiabatic energy, E_a, and the energy of the vertical transition, E_v. For $5 \leq \frac{\Delta E_{FC}}{E_{\text{vib}}}$, the distribution of Franck-Condon factors passes into a Gaussian distribution [120].

4

Novel method: soft X-ray energy-dispersive NEXAFS

X-ray absorption spectroscopy (XAS) is a well-established technique for investigations of the electronic and geometric structure of molecular thin films [17–19, 121, 122]. In the soft X-ray regime, the XAS spectrum is usually measured by stepping the photon energy with a monochromator and monitoring a secondary process which is proportional to the X-ray absorption cross-section [104]. In the following, I will concentrate on the exclusive detection of *KLL*-Auger electrons with a kinetic energy of about 250 eV. Auger electron yield (AEY) XAS is a very surface-sensitive method with a probing depth of about 1 nm, due to the short mean free path of such electrons [106].

At high resolution, an XAS measurement of an organic sample at the C *K*-edge and in the photon energy range between 280 eV and 320 eV can take up to 45 min. Even a scan over a range of a few eV can take a some minutes. For studies of organic film growth and post-growth, the measurement time of the traditional XAS setup might be too long [12–16]. Especially investigations of the transition from a disordered to an ordered arrangement requires a faster measurement. In the Chapters 5.2 and 5.3, I will present experimental data of short-lived transient phases during post-growth which I could not investigate with the traditional XAS setup.

One way to accelerate the measurement while maintaining high-resolution capabilities has proven to be very successful. In this measurement method, the sample is illuminated with energy-dispersed light and the resulting signal is recorded simultaneously at different photon energies with an electron spectrometer with spatial resolution capabilities. While energy-dispersive X-ray absorption spectroscopy is a well-established technique in the hard X-ray regime [123–127], the setup for the soft X-ray regime is more challenging. The energy-dispersed hard X-ray light is obtained using a bent crystal. In the soft X-ray regime, this is not possible due to the limited penetration depth of soft X-ray light. Instead, the

optical parameters of the mirrors and the grating are chosen in a suitable combination so that the dispersed light of the grating monochromator is projected and focused onto the sample [128–131]. With an electron spectrometer with spatial resolution a simultaneous detection of the emitted electrons at different photon energies is possible.

Up to now, the soft X-ray energy-dispersive setup was mainly used for resonant photoemission experiments on organic compounds and for investigations of the molecule-substrate charge transfer dynamics [131, 132]. In this work, I will demonstrate the capabilities of energy-dispersive NEXAFS for real-time studies on post-growth processes. Moreover, since the electronic and especially the vibronic structure are simultaneously probed, the method is also sensitive to intermolecular interaction which might alter the vibronic and electronic structure (see Chapter 2.1). From the combined and simultaneously obtained information on the molecular spatial orientation, film morphology and electronic properties, we could gain new insight into the complex interplay of post-growth and electronic structure.

In the following section, 4.1, I will describe the beamline and experimental setup for time-dependent and temperature-controlled energy-dispersive NEXAFS measurements in detail. Section 4.2 covers the data acquisition and evaluation employed for energy-dispersive NEXAFS. Especially the correction of the non-linear behavior of the micro channel plate and the photon energy calibration will be discussed. I will close this chapter in Section 4.3 with an investigation of the radiation damage to NTCDA multilayer films during NEXAFS measurements in the energy-dispersive setup.

4.1 Beamline and experimental setup

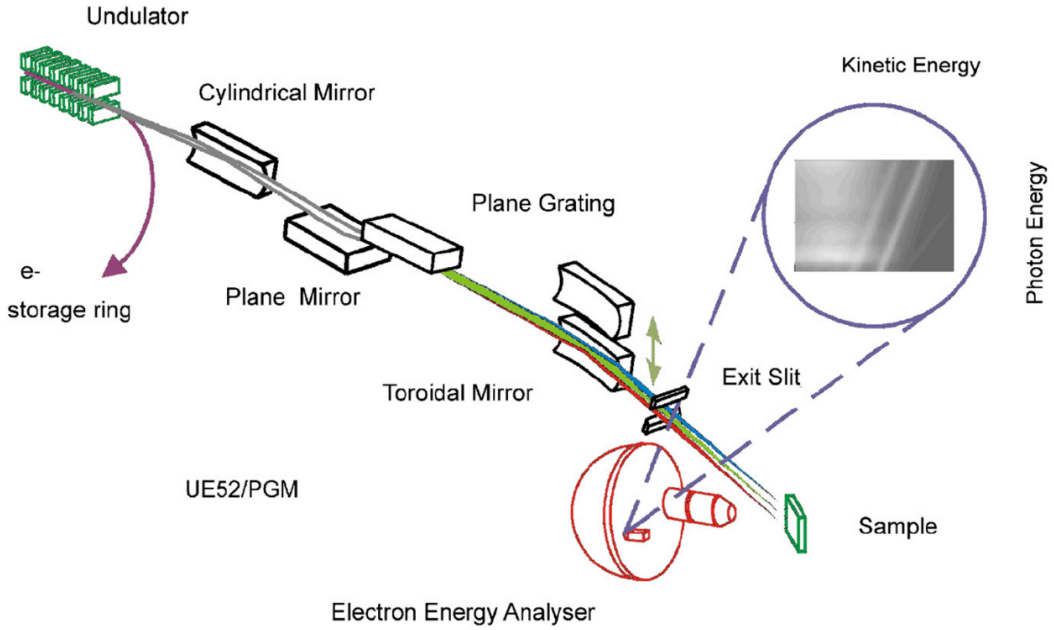

Figure 4.1: Energy-dispersive beamline and end station UE52-PGM at the BESSY II synchrotron light source of the Helmholtz-Zentrum Berlin. The beamline was operated in the energy-dispersive mode in which the beam is focused on the sample without an exit slit, thus leading to a spatial dispersion of photon energies on the sample in vertical direction [131]. By using an electron spectrometer with spatial resolution (VG-SCIENTA R4000), NEXAFS spectra can be recorded in a multi-channeling mode, with acquisition times of less than one second being possible and an energy resolution better than 50 meV at the C K-edge. The illustration was taken from reference [131].

One of the first energy-dispersive soft X-ray absorption beamlines was constructed at the bending-magnet station BL-7A at the Photon Factory in Japan [128–130]. Following this design, an energy-dispersive soft X-ray setup was constructed at the end station UE52-PGM at BESSY II synchrotron light source of the Helmholtz-Zentrum Berlin (Figure 4.1) [131]. The beamline is operated with collimated light and is designed based on a plane-grating monochromator (PGM), for which the fix-focus constant (c_{ff}) is independent of the photon energy [133]. The value of the c_{ff} can be chosen freely within a wide range, leading to higher flexibility for changing the photon flux and energy resolution [134,135].

The energy-dispersive NEXAFS measurements presented in this work were done at BESSY II. The end station UE52-PGM can be operated in the traditional and in the energy-dispersive setup. Through changing between two toroidal mirrors by means of an external stepper motor drive, the focus point of the light beam can be changed between the exit slit (traditional mode) and the sample position (energy-dispersive mode). In the energy-dispersive mode, the exit slit is fully open and the light beam is focused horizontally and vertically on the sample position (Fig. 4.1). In this beamline configuration, the spot size is less than 50 μm horizontally and about 3 mm in the photon energy-dispersive vertical direction [131]. The photon energy dispersion width is given by

$$h\nu_{\text{disp.}} = \frac{h}{c \cdot e_0} \left(\frac{M_{\text{grat}}}{\cos(\arcsin(\frac{\sin(\alpha)}{c_{\text{cff}}})) - \cos(\alpha - 2 \cdot \arctan\frac{A}{B})} - \frac{1}{\lambda} \right), \qquad (4.1)$$

where h is Planck's constant, c the vacuum speed of light, e_0 the elementary charge, M_{grat} the lines per mm of the grating, λ the wavelength of the incident light, α the angle of reflection, c_{cff} the constant fixed focus factor, A the size of the MCP detector slice, B the distance between sample and grating.

BESSY II can be run in different operation modes, but always in the so-called *decay mode* and with constantly dropping ring current between injections of electrons into the storage ring.[1] For the purpose of the NEXAFS experiments, only the ring current, i.e. the photon flux, in the respective operation mode has to be considered. By adjusting the c_{ff} value, energy-dispersive NEXAFS measurements in the *multi-bunch hybrid mode* (maximum storage ring current of 300 mA) and *low-alpha multi-bunch hybrid mode* (maximum storage ring current of 100 mA, 45 mA, and 15 mA) can be performed. The c_{ff} value were chosen to achieve a sufficiently good signal-to-noise ratio while maintaining a sufficiently low photon flux to avoid radiation damage. In general, the dispersive photon energy width and spatial resolution of the dispersed light also depend on the c_{ff} value. For c_{ff} values larger than 7 and a photon energy below 300 eV, the width of the dispersive photon energy window and the spatial resolution of the dispersed light is nearly constant, i.e. $\Delta h\nu = 1.5$ eV. For experiments in the so-called *multi-bunch hybrid mode*, I chose c_{ff} values between 15-70 and in the so-called *low-alpha multi-bunch hybrid mode*, I conducted the experiments at c_{ff} values between 7-15. At these c_{ff} values, I obtained the NEXAFS spectra at a resolution of about 50 meV and at a sample current below 10 nA at resonant excitation of an organic film.

[1] Note, since August 2012 BESSY II is operated in the so-called top-up mode with short refills of the ring every minute.

The X-ray absorption spectra in the energy-dispersive setup were obtained by measuring the emitted Auger electron yield (AEY) with an electron analyzer, after excitation of a core electron into an unpopulated orbital. For organic compounds, I monitored the signal from the C *KLL*-Auger electrons in the kinetic energy range between 252 eV and 267 eV. The VG-SCIENTA R4000 electron analyzer was operated in the *spatial imaging mode* (input lens with x10 magnification). Also, I used the so-called *fixed mode* with an energy window of about 15 eV for parallel data acquisition. In the vertical direction, the dispersed light is detected with spatial resolution and in the horizontal direction the kinetic energy of the emitted Auger electrons is detected within an energy range of about 15 eV.

With these settings, the chosen c_{ff} values, and at photon energies below 300 eV, it was possible to obtain X-ray absorption spectra of 1.5 eV photon energy width at a resolution of 50 meV within seconds.

For temperature-controlled experiments, the thermocouple was mounted on the sample holder close to the silver crystal to facilitate accurate temperature measurements. Measurements were obtained in a temperature range between 93 K and 320 K. The sample was cooled with liquid nitrogen and heated, if necessary, with a filament mounted onto the reverse side of the crystal. To ensure a constant temperature during the experiments, the temperature was controlled by a *proportional-integral-differential* (PID) controller. At a filament current below 4 A, no artifacts, e.g. energy shifts or distortion of peaks, caused by heating the sample were observed. All temperature-controlled experiments in this work were performed with this setup and at less than 4 A filament current.

4.2 Data acquisition and normalisation

A quantitative analysis of a raw data set requires a specific evaluation procedure which differs in some details from the generally applied intensity normalization and energy calibration procedures used for traditional NEXAFS. Most importantly, the data have to be corrected for the micro-channel plate's (MCP's) spatially inhomogeneous response and non-linear gain, which will both directly influence signal intensities and line shape. These issues are well-known from

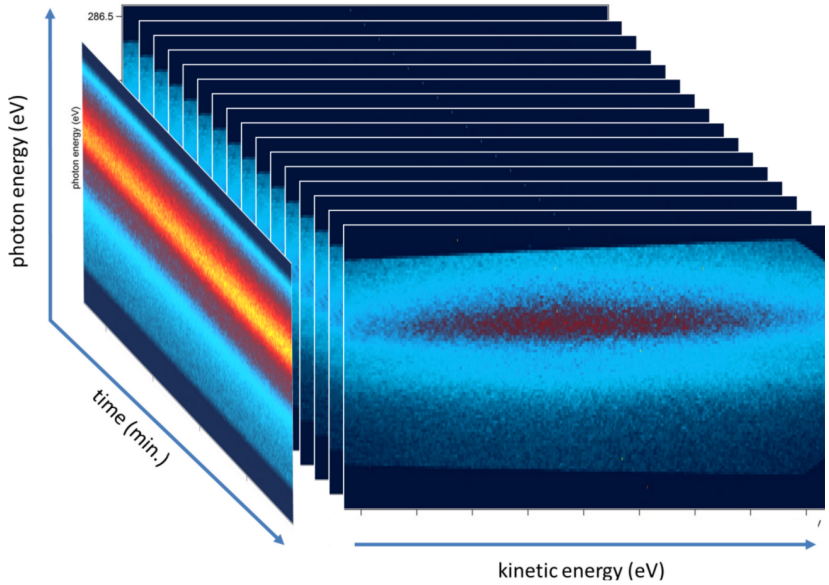

Figure 4.2: Raw data set of a typical time-dependent energy-dispersive NEXAFS experiment. The closely-spaced 2D colour plots represent the micro-channel plate images of the C *KLL*-Auger electron spectra in the range from 252–267 eV kinetic energy and from 284.75–286.3 eV photon energy. Each image is taken within 6 sec. The total measurement time is typically about 40 min. To extract the NEXAFS spectrum, the measurements were integrated along the kinetic energy axis to obtain the 2D colour plot on the left hand side. Yellow refers to high, blue to low intensity.

angle-resolved photoelectron spectroscopy experiments utilizing the same detectors [136, 137].

In Fig. 4.3, the non-linear response of the MCP can clearly be recognized by the different peak shapes and peak-to-background intensity ratio of the Ag *MNN*-Auger electron spectra (black traces) which were obtained at different photon fluxes and were scaled with the sample current. For a better demonstration of the non-linear effect, I integrated along the vertical i.e. spatial direction of the MCP. To determine correction factors, I measured the Ag *MNN*-Auger electron spectra with different photon fluxes in the analyzer's *fixed mode* and normalized the data to the sample current. Subsequently, a routine was set up, which corrects each MCP pixel so that the Ag *MNN*-Auger spectra match the respective data measured with a channeltron (CT) detector. The response of this CT detector was linear in the investigated range of different photon fluxes. All time-dependent NEXAFS data were also corrected for the constantly decreasing ring current. In Fig. 4.3, the spectra of the Ag *MNN*-Auger electrons

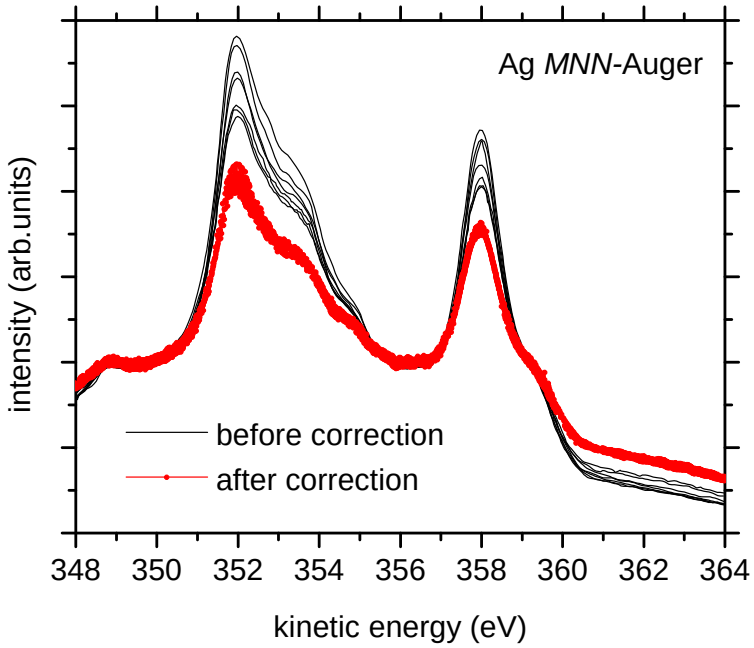

Figure 4.3: Photoelectron spectra of Ag *MNN*-Auger electrons before (black traces) and after (red traces) correction of the MCP non-linear response function. The correction procedure is described in the text. The measurements before correction where obtained at different photon fluxes and scaled with the sample current. The spectra were normalized to 350 eV kinetic energy.

before (black traces) and after (red traces) correction are shown. The uniform peak shape and peak-to-background intensity for each spectrum after applying the correction routine accounts for the successful compensation of the non-linear response.

Also the photon energy calibration requires particular attention in dispersive NEXAFS. Usually, NEXAFS spectra are energy-calibrated by determining the monochromator offset before or after the respective experimental run by measuring the well-known absorption lines of, e.g. gaseous samples such as N_2 or CO_2 [138–140], or using an electron analyzer and measuring a well-known photoemission lines of the substrate [141].

In the spatial mode of the electron analyzer, the raw data is obtained in kinetic energy (in eV) vs. spatial position (in mm). Since in the energy-dispersive setup the monochromator and undulator are not moving as long as the photon energy window is not changed, the relative accuracy of the photon energies measured in one experimental run is very good, as shown in Chapter 5.2, for instance, rela-

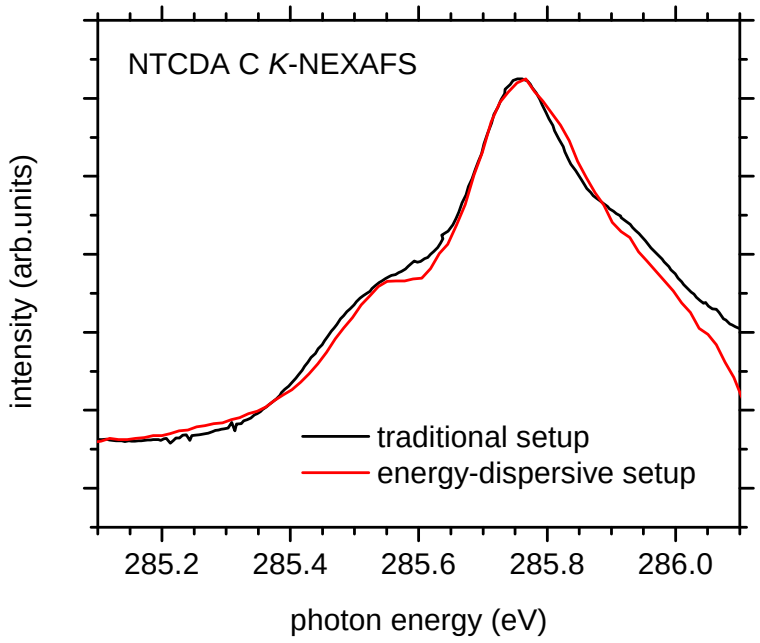

Figure 4.4: X-ray absorption spectra of a NTCDA multilayer film (9 ML) prepared at 95 K and measured with *p*-polarized light and grazing incidence (70°) in the traditional setup (black trace) and photon energy-dispersive setup (red trace). The spectra were normalized to the peak maxima.

tive peak shifts of less than 10 meV can be resolved. For the calibration of the absolute photon energy values, I recorded a NTCDA/Ag(111) sample prepared at 95 K in the traditional energy-scanning mode with the photoemission signal of the Fermi edge set to the value taken from reference [141].This spectrum, which is displayed in Fig.4.4 (black trace), was then used for the calibration of the energy scale of dispersive NEXAFS experiments on NTCDA samples (see Fig. 4.4). All depicted time-dependent X-ray absorption spectra were also corrected for the constantly dropping ring current. It should also be noted that over the measurement time of a typical experiment (about 40 min), no recognizable shifts of the photon energy shift resulting from beam line instabilities were observed.

4.3 Investigation of radiation damage to NTCDA multilayer film

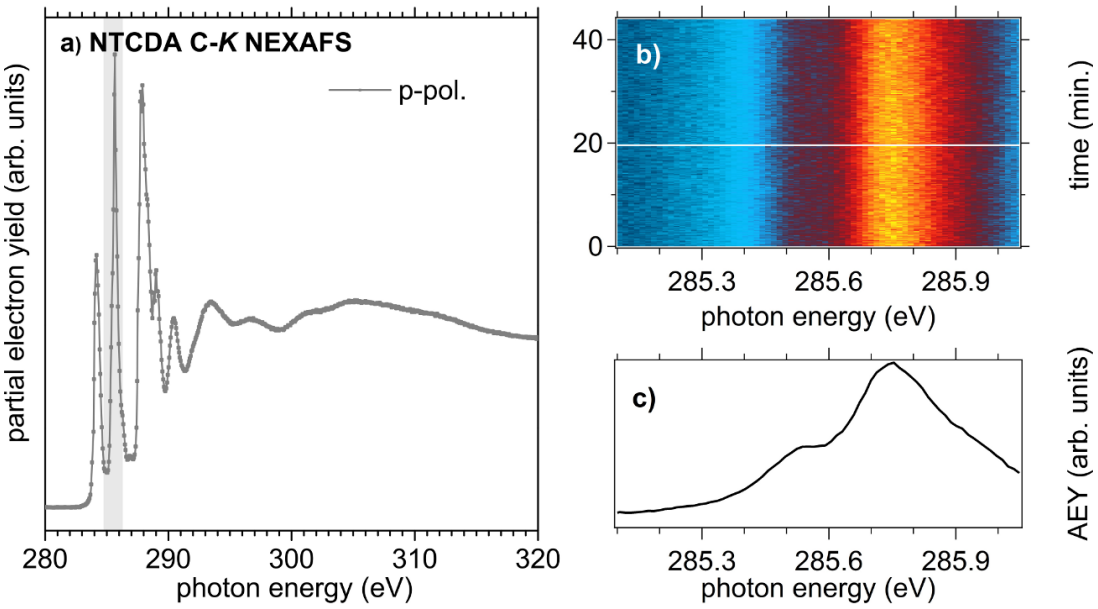

Figure 4.5: a) C *K*-NEXAFS spectrum of a NTCDA multilayer film on Ag(111) prepared at 95 K, recorded in the traditional NEXAFS setup with *p*-polarisation of the incident beam. The shaded region indicates the energy window recorded in the energy-dispersive mode. b) Close-up of the π^*-resonances recorded in the energy-dispersive setup with *p*-polarisation and at a constant temperature of 95 K. Yellow refers to high intensity and blue to low intensity. Note that the intensities of the recorded resonances are constant for over 40 min. and the spectral shape is not changing. The white line indicates the position on the temporal axis of the spectrum displayed in c). c) Spectrum extracted from the data displayed in b) at $t = 20$ min.

Organic compounds are very sensitive to radiation damage in spectroscopic experiments [142–146]. Chemical bonds between the atoms of a molecule can break, resulting in a change in the molecular structure and the optical and electronic properties. Especially after measurements with X-ray light and exposure to a high photon flux from a synchrotron light source, the degradation of the organic sample has to be carefully examined.

In energy-dispersive X-ray absorption measurements it is of crucial importance to look for signs of radiation damage since in this mode the exit slit is fully opened

and the X-ray light is focused onto the sample. This can result in very high photon flux and sample current. Also, the measurements were obtained from the same spot on the sample for about 30-45 min. To exclude significant radiation damage during energy-dispersive X-ray absorption experiments on condensed NTCDA multilayer films, I compared the spectral shape of the obtained spectra with that of NEXAFS spectra recorded in the traditional setup in the photon energy scanning mode. In addition, the intensity evolution between 285–286.3 eV of the NEXAFS spectra was analyzed for a typical measurement time of about 40 min. For a detailed discussion of the spectral shape and the involved electronic transitions, see Chapters 5.2 and 5.3.

The measurements in the traditional NEXAFS setup were performed by stepping the photon energy with a monochromator and monitoring the emission of Auger electrons at the C K-edge with p-polarized light at grazing incidence (70° with respect to the sample surface normal). In the photon energy-dispersive mode, the experiments were performed at a c_{ff} value of 16 and at a photon energy-dispersive width of 1.5 eV. With the electron analyzer, the carbon KLL-Auger electrons in the range of 250–270 eV were recorded. I concentrated on the NEXAFS signal between 285 eV and 286.2 eV measured with p-polarized light and at grazing incidence of the beam. For the 9 ML-thick NTCDA multilayer films, NTCDA was evaporated in UHV from a Knudsen cell evaporator onto a Ag(111) single crystal at a substrate temperature of 95 K. During the experiment, the temperature was kept constant at 95 K.

Fig. 4.5 a) shows a typical X-ray absorption spectrum of a NTCDA multilayer (9 ML) film on Ag(111) prepared at 95 K which was measured with the traditional setup. The spectrum corresponds well with those reported in the literature [19, 147]. In Fig. 4.5 b), I present a 2D colour plot of the time-dependent NEXAFS measurement in the energy-dispersive mode (yellow refers to high intensity, blue to low intensity). The investigated photon energy region is highlighted by the shaded region in a). The intensity evolution of this signal is nearly constant for 44 min and the spectral shape is not changing. To compare the spectral shape of the recorded NEXAFS resonances with those found in the literature, I integrated for 30 sec at t=20 min in spectrum 4.5 b). The spectrum obtained by this integration is shown in c). Also the spectral shapes of the NEXAFS resonances correspond well to the measurement obtained with the traditional setup as shown in a) and to those in the literature [19, 147]. In addition, I also investigated the photoemission line of the C 1s core level (not shown here). No change of the spectral shape of the core level signal before and after the NEXAFS measurements was found.

Radiation damage to organic compounds in X-ray absorption experiments is accompanied by a significant drop in intensity and alteration of the spectral shape due to degradation, e.g. bond scission, double-bond formation, and cross-linking, of organic compounds [143, 144, 148, 149]. I will show in Chapters 5.2 and 5.3, that average molecular orientation with respect to the substrate surface and film morphology is not changing at a constant substrate temperature of 95 K and, thus, does not contribute to the NEXAFS intensity evolution. Therefore, any change in NEXAFS intensity can solely be attributed to radiation damage to the organic film. Since the NEXAFS intensity is nearly constant for over 40 min and the spectral shape corresponds well to the literature spectra, I conclude that there is no significant radiation damage to NTCDA multilayer films in the NEXAFS experiments in the energy-dispersive mode and at the chosen beamline and experimental settings.

5

Results

In Chapter 5.1, I will summarize some of the well-known properties of 1,4,5,8-naphthalene tetracarboxylic acid dianhydride crystals and multilayer films. In Chapter 5.2, I present the results of the core hole-electron correlation study in coherently coupled molecules by energy-dispersive near-edge X-ray absorption fine-structure spectroscopy. In a transient phase which exists during the transition between two bulk arrangements, NTCDA multilayer films exhibit peculiar changes in the line shape and energy position of the X-ray absorption signal at the C K-edge with respect to the bulk and gas-phase spectra. I interpret the observed spectroscopic results with the help of the coupling concepts for intermolecular interaction outlined in Chapter 2. Thereby, their validity in the context of X-ray excitations will be tested. By applying these models, I estimate the energy transfer rate and quantify the coherence length of the delocalized core exciton. Parts of this chapter are accepted for publication in the *Physical Review Letters* [83].

In Section 5.3, I treat the structure formation of NTCDA multilayer films on Ag(111) surfaces studied by time-dependent energy-dispersive near-edge X-ray absorption fine-structure spectroscopy (NEXAFS) and time-dependent photoelectron spectroscopy. The time resolution in the range of seconds of the novel method allows to identify several sub-processes which occur during the post-growth three-dimensional structural ordering and measure their relevant time scales. By applying the Kolmogorov-Johnson-Mehl-Avrami model which I introduced in Chapter 2.2.2, the activation energies of the temperature-driven sub-processes can be derived from the time evolution of the NEXAFS signal. Parts of this chapter are submitted to *New Journal of Physics*.

5.1 Material system

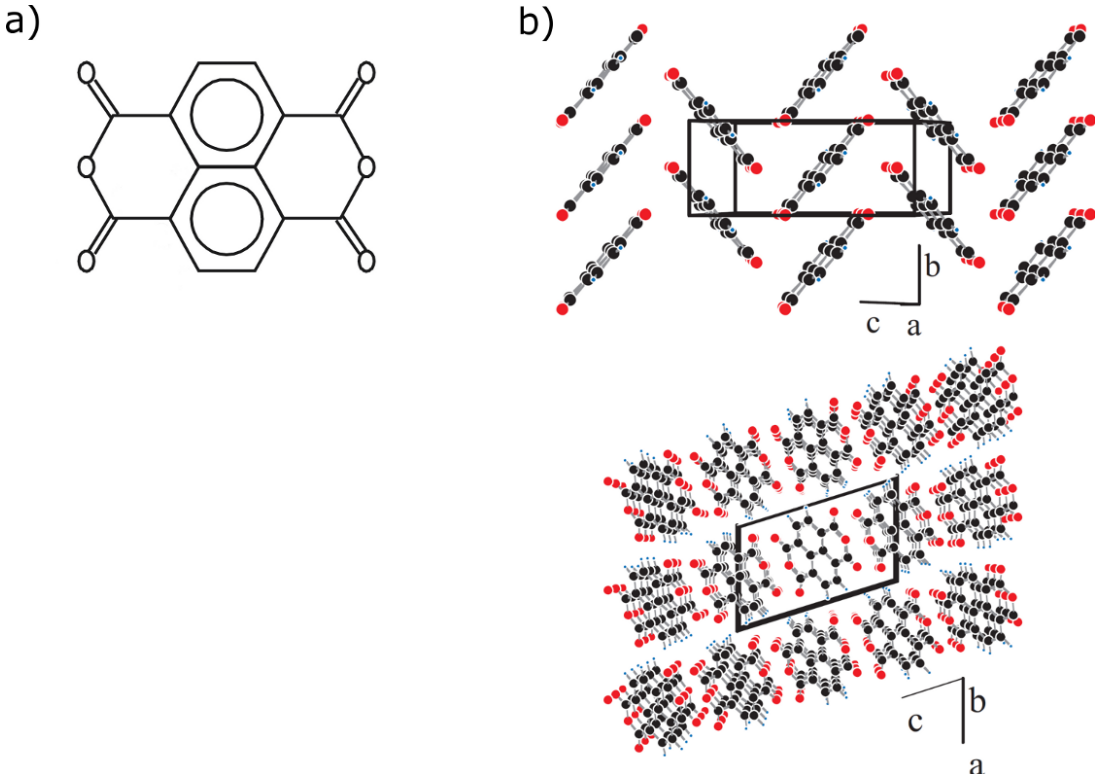

Figure 5.1: a) Structural formula of NTCDA. b) Crystal structure model deduced from X-ray diffraction studies. Figure taken from [150].

In this work, I investigate thin films of the aromatic molecule 1,4,5,8-naphthalene tetracarboxylic acid dianhydride (NTCDA). The chemical structure is shown in Fig. 5.1 a). The planar dye molecule belongs to the D_{2h} symmetry group and has a mass of 268 amu.

The crystal structure of NTCDA was determined with X-ray diffraction studies before [151] and is illustrated in Fig. 5.1 b) [150]. According to Born et al., the monoclinic crystals belong to the space group P_2/n with two molecules in a unit cell and the basis vectors $|\vec{a}| = 7.867\,\mathring{A}$, $|\vec{b}| = 5.305\,\mathring{A}$, $|\vec{c}| = 12.574\,\mathring{A}$. The angle between the $\vec{a}$- and $\vec{c}$-vectors is $\beta = 72.73°$. The molecules stack in $\vec{b}$-direction, with an interplanar distance of 3.52 Å and an angle of 47.9° between the stacking direction $\vec{b}$ and the normal of the molecular plane.

For condensed NTCDA multilayer films on weakly interacting substrates, e.g. MoS_2, a bulk-like phase was observed [152]. On the also weakly interacting HOPG surface, a bulk-like phase as well as close-packed and face-to-face arrangements of NTCDA molecules were reported, as shown in Fig. 5.2 [152,153]. Based on the STM measurements in a), Miyamoto et al. [153] suggested a face-to-face arrangement as illustrated in b), with one NTCDA molecule per unit cell.

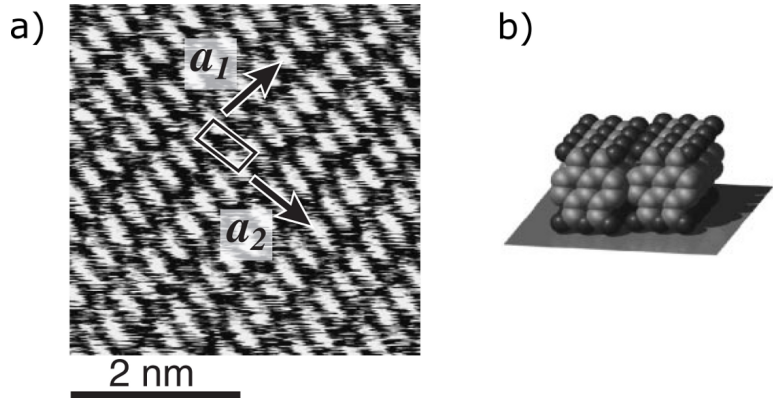

Figure 5.2: a) STM image of NTCDA on HOPG. The unit cell and the corresponding vectors are indicated in the image. b) Suggested structure model. Figure taken from [153].

For condensed NTCDA multilayer films on Ag(111) at least three different film structures were observed [147,154,155]. As discussed before, at substrate temperatures below 100 K, the molecules are preferentially lying flat on the substrate and no long range order is observed [147]. By annealing such a film at T>150 K, the molecules change their orientation and film structure. For NTCDA multilayer films prepared at room temperature, two film structure models were suggested, as presented in Fig. 5.4 [154]. Both models are compatible with the LEED pattern in Fig. 5.3 [154,156] and are based on the known crystal structure [151].

In model A, the molecules are nearly perpendicularly orientated to the substrate surface, i.e. a tilt angle of 82° was derived [147] and is indicated on the left-hand side of Fig. 5.4. Due to the six-fold symmetry of the topmost substrate layer, the superstructures of model A have 3 or 6 rotational and mirror domains, respectively. In Model B (Fig. 5.4), also two super-matrices are proposed but the molecules are tilted about 45° with respect to the substrate surface [109]. Solely from LEED-measurements we cannot distinguish between the two structures.

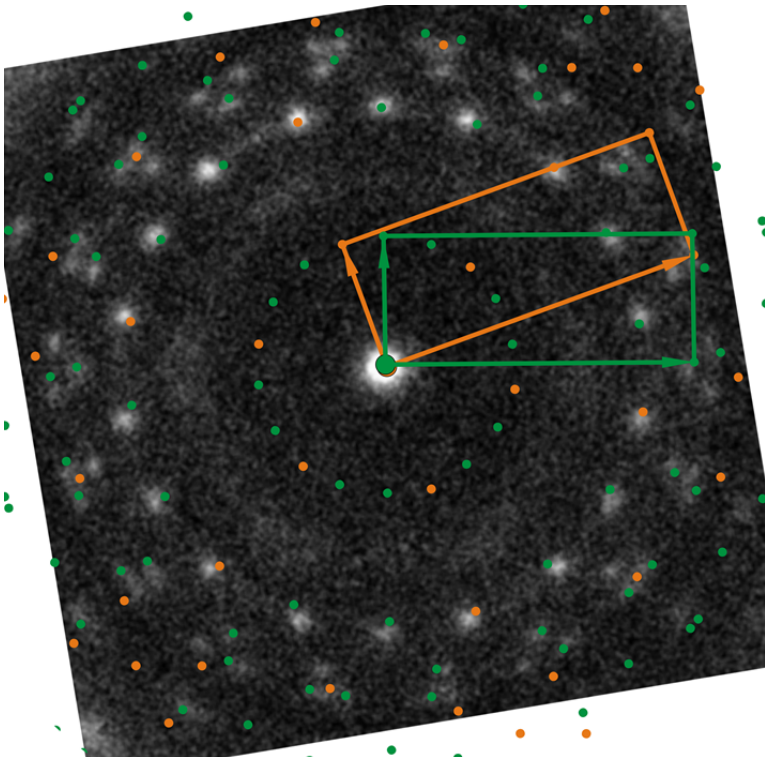

Figure 5.3: SPA-LEED diffraction pattern at 23 eV beam energy of a 30 ML NTCDA film on Ag(111). Two incommensurate superstructures (shown here for model A) are able to simulate the pattern. The unit cells (green and orange) are identical but rotated by 20° [150].

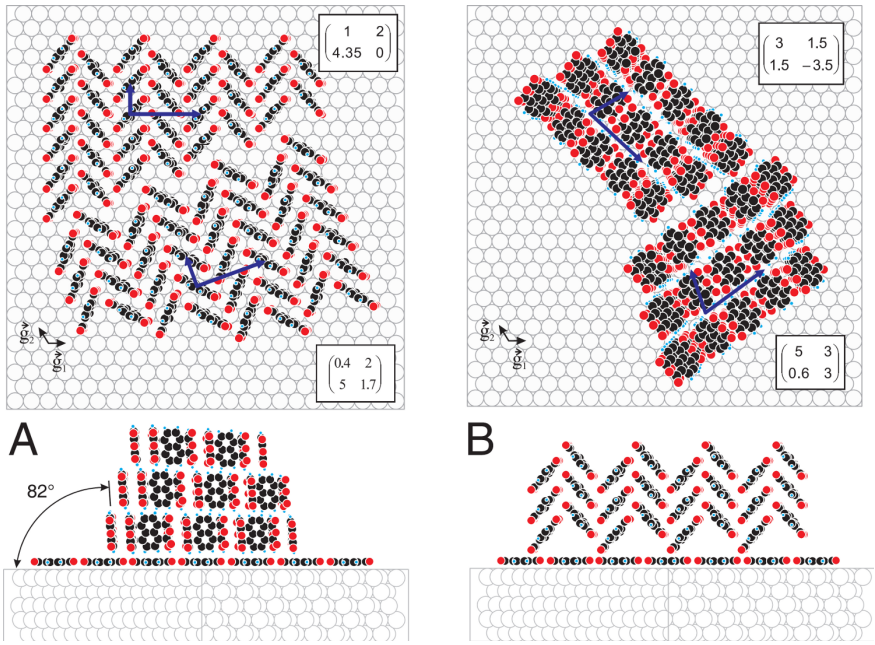

Figure 5.4: Two different crystal structure models, A and B, for NTCDA multilayer films. The upper part shows a top view and the lower part a side view onto the suggested real space suggestion with the derived super-matrices. The illustration was taken from [154].

With high-performance spectro-microscope (SMART) measurements of NTCDA multilayer films, both real-space models were found [156]. In addition, photoemission measurements [109], Hg-photoelectron emission microscopy [156], and low-energy electron microscopy [156] also suggest that the first monolayer of a multilayer film is lying flat on the substrate surface.

5.2 Core hole-electron correlation and intermolecular coupling in NTCDA multilayer films

X-ray absorption measurements at high-resolution beam lines of third-generation synchrotron sources are a powerful tool for the investigation of the electronic and vibronic structure of molecules [17–19]. From an analysis of high-resolution data one can gain insight into the complex response of the electronic system and the molecular frame to the electronic excitation. Upon excitation of a core electron into an unoccupied molecular orbital, a particularly strong reaction of the electronic system in the vicinity of the core excitation occurs. The resulting combination of core hole and electron is often referred to as core exciton. This core hole-electron correlation has to be included for a correct description of the experimental data. However, the nature of core excitons is vague in molecular materials since experimental information, e.g. on the spatial expansion, is usually difficult to extract from X-ray absorption data due to various other interfering effects [157,158]. Thus, it is not clear whether the excitation is mainly localized on one molecule, or on a subunit of a molecule, or if it extends over several molecules.

In this chapter, I demonstrate the importance of the core hole-electron correlation in near-edge X-ray absorption fine-structure (NEXAFS) data of organic molecules. Using the organic dye 1,4,5,8-naphthalene tetracarboxylic acid dianhydride (NTCDA) as an example, I show that under certain circumstances the molecules exhibit an extraordinarily strong intermolecular coupling which leads to a redshift of electronic transitions and a substantial narrowing of the vibronic progressions in the NEXAFS spectra with respect to the gas phase. The respective experimental data can be explained by a coupling of the transition dipoles to the neighboring molecules, thus resulting in a significant intermolecular delocalisation of the core hole-electron pair. While this effect is well established for optical excitations [159], the calculated transition dipoles in core excitations are substantially smaller and, thus, a more local character of the excitation may generally be expected.

The delocalisation of the core exciton upon absorption of an X-ray photon implies not only the transfer of the excited electron but also of the core hole. While for diatomic molecules such as N_2 and O_2 experimental evidence for the non-local character of the core hole exists [160–162], I present the first example for the delocalization of a core hole in condensates of large molecules such as aromatic dyes.

5.2.1 Sample preparation and experimental setup

For the model system NTCDA (see molecular structure in Fig. 5.5 b) on a Ag(111) surface, different structural phases exist for multilayer films (see Chapter 5.1) [19, 147, 163]. Growth at substrate temperatures below 100 K results in morphologically smooth films with molecules preferentially lying flat on the substrate and showing no long range order [147]. Heating the samples to temperatures above 150 K leads to an increasing crystallinity of the films and changes the molecular orientation towards a configuration perpendicular to the substrate. During this transition, a transient phase occurs which exists only for about 10 minutes and shows the characteristic changes in the signature of the NEXAFS spectra which are of particular interest in this work. Thus, the fast acquisition of X-ray absorption data is crucial. Therefore, the experiments were performed at beamline UE52-PGM of BESSY II in Berlin.

The beamline was operated in the energy-dispersive mode in which the beam is focused on the sample without an exit slit, thus leading to a spatial dispersion of photon energies on the sample in vertical direction [131]. By use of an electron spectrometer with spatial resolution (VG-SCIENTA R4000), NEXAFS spectra can be recorded in a multi-channel mode with a feasible acquisition time of less than one second and an energy resolution better than 50 meV at the C K-edge. For a detailed discussion of the energy-dispersive mode, see Chapter 4.

5.2.2 Experimental results

Results in traditional NEXAFS setup

Fig. 5.5 a) shows the C K-NEXAFS spectra of a NTCDA film four monolayers (4 ML) thick which was prepared and measured at a substrate temperature of 95 K. The absorption signal of the π^*-resonances shows in the range between 282 eV and 290 eV a characteristic dependence on the polarization of the incident light which allows determining the average molecular orientation with respect to the substrate surface [104]. The strong dichroism in Fig. 5.5 a) indicates a preferential flat-lying orientation of the NTCDA molecules in the film, consistent with previous investigations [19, 147]. Fig. 5.5 b) shows the π^*-resonances of the p-polarized spectrum on an expanded energy scale. According to the results of the Hartree-Fock calculations [164], plotted on the bottom of Fig. 5.5 b),

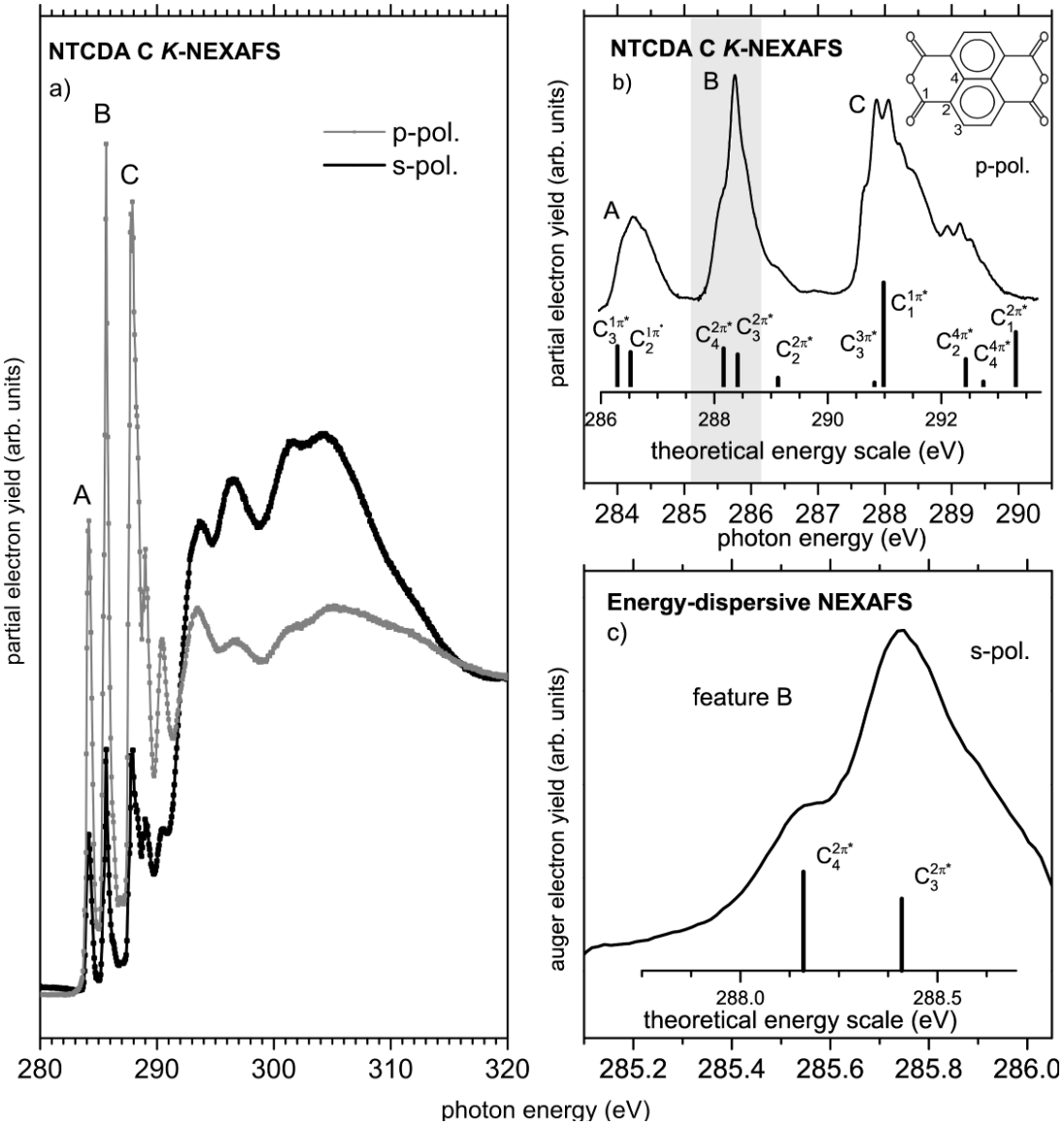

Figure 5.5: a) C *K*-NEXAFS spectra of a NTCDA multilayer film as prepared at 95 K, recorded with *s*- (black line) and *p*- (grey line) polarization of the incident beam. b) Close-up of the π^*-resonances (denoted by A, B and C) recorded with *p*-polarisation compared to the result of a Hartree-Fock calculation with the GSCF3 code [164]. The theoretical energy scale was shifted and scaled to fit the experimental data. The calculated electronic transitions are labeled with the respective carbon 1s-sites C1 to C4 (see inserted molecular structure) and final-state orbitals π^*, $2\pi^*$ and $3\pi^*$. The shaded region indicates the energy window recorded in the energy-dispersive mode. The resulting spectrum is displayed in panel c).

the spectrum can be explained by the superposition of several electronic transitions from the four symmetry-inequivalent carbon 1s sites C1 to C4 (see insert in Fig. 5.5 b)) to the final-state orbitals $1\pi^*$, $2\pi^*$ and $3\pi^*$. In addition, the electronic transitions show a characteristic coupling to vibrations, leading to the rich fine-structure of the three main signals, denoted by A, B and C in Fig. 5.5 b) [19].

Time-dependent energy-dispersive NEXAFS

While the spectra in Fig. 5.5 a) and b) were recorded by scanning the photon energy in the normal beamline mode with an acquisition time of about 30 min per spectrum, Fig. 5.5 c) shows an energy-dispersive NEXAFS experiment in the energy regime of feature B (shaded region in Fig. 5.5 b)). The integration time was 30 sec and the data is in very good agreement with feature B of Fig. 5.5 b). The fine structure is well resolved, and according to the calculations in Fig. 5.5 b), the signal in the photon energy range between 285.1 and 286.0 eV corresponds to the two electronic transitions C4 1s–$2\pi^*$ and C3 1s–$2\pi^*$ which can be assigned to carbon atoms located in the naphthalene core (see Fig. 5.5 b)). As demonstrated in Ref. [19], these electronic transitions lead to the excitation of vibrations of the aromatic core with vibrational energies of around 90 meV.

The colour plot in Fig. 5.6 a) shows the time evolution of feature B during an energy-dispersive NEXAFS experiment. The sample with a thickness of about 4 ML was prepared at 95 K and then quickly (in about 1 min) heated to 220 K in order to induce the transition from flat-lying to upright-standing molecules. $t = 0$ refers to the time when a constant sample temperature of 220 K was reached. In the bottom of Fig. 5.6 a), i.e. directly after preparation at 95 K, the spectra resemble the typical absorption signal of films prepared at low temperature (see Fig. 5.5 c)). This becomes obvious in Fig. 5.6 b), which displays spectra derived after integration of the intensity map in Fig. 5.6 a) over intervals of 3 min at the times indicated by the horizontal dashed lines. Shortly after a substrate temperature of 220 K is reached, the line shape of feature B is significantly altered. Starting at $t = 2$ min, the intensities of the absorption peaks at 285.4 eV and 285.7 eV increase while it decreases between those peaks. In addition, the line width of the most prominent signals decreases, which can be observed best in the spectrum in Fig. 5.6 b) extracted after 8 min at 220 K. Moreover, an energy shift of the main spectral components towards lower energy occurs which is indicated by the slanted dashed lines in Fig. 5.6 a). The energy shift amounts to about

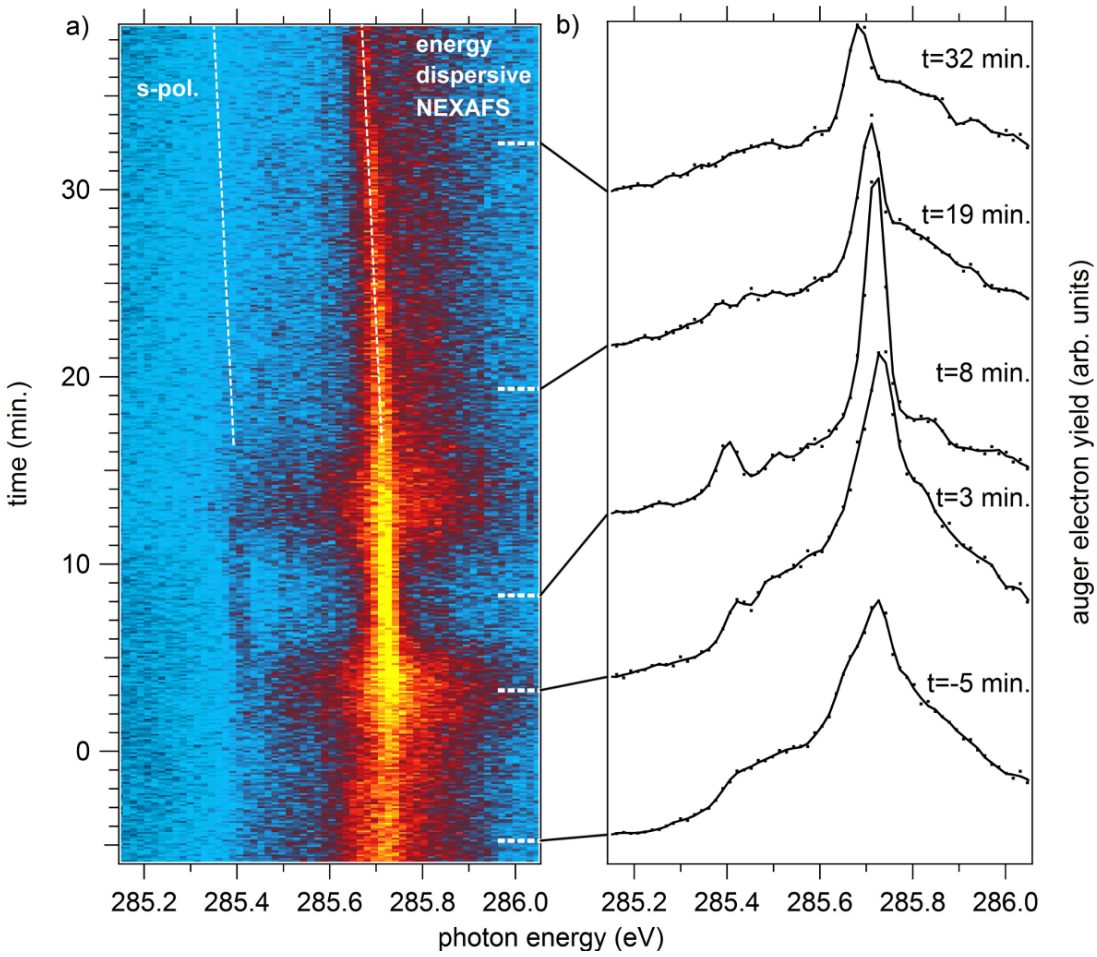

Figure 5.6: a): 2D colour map of the energy-dispersive NEXAFS spectra of feature B, recorded with s-polarized light and plotted against time. Yellow refers to high, blue to low intensity. The 4 ML thick film was prepared at 95 K and heated to 220 K within 1 min. $t = 0$ refers to the time at which a constant sample temperature of 220 K was reached. The slanted dashed lines are guidelines for the eye to illustrate the energy shift of the main components. b) NEXAFS spectra of feature B derived by integration of the intensity map in Fig. a) over 3 min at the times indicated by the horizontal dashed lines (black dots: original data; solid line: 3-point average).

$\sim$80 meV after 35 min. While the overall intensity increases until $t \approx 12$ min, the absorption signal decreases constantly after the sample is kept at 220 K for more than 12 min.

5.2.3 Interpretation and discussion

This variation in general intensity can be explained by the change in orientation angle of the NTCDA molecules from flat lying to a more upright orientation with respect to the substrate surface, which occurs after the sample temperature is increased to 220 K [147]. This leads to an immediate intensity increase in the C K-NEAXFS data recorded with s-polarisation [104]. However, this increase in intensity is counteracted by a change in film morphology since the increased sample temperature also leads to a roughening of the initially smooth film and to formation of 3D islands. Due to the limited probing depth of about 1 nm [106] of the Auger electrons mainly contributing to the NEXAFS signal in the electron yield mode, this second process leads to an overall reduction of the absorption signal. Moreover, the morphology change includes material transport and occurs on a longer time scale than the change in orientation angle, thus accounting for the observed delayed intensity decrease [83].

In the following, I will concentrate on the particular changes in the C K-NEXAFS spectral signature of the NTCDA which occur during the transition. Fig. 5.11 compares the NEXAFS spectra of feature B for four different NTCDA samples. At the bottom, gas phase data is displayed which is representative for the isolated molecules [165]. Film growth at low sample temperature ($T = 95$ K) results in a disordered phase with preferentially flat-lying molecules [19], while annealing to temperatures above 150 K results in the ordered phase with a more upright molecular orientation [19]. The data of the transient phase during the transition is plotted at the top.

The line shape in the spectrum of the disordered phase resembles that of the gas phase while the entire spectrum is redshifted by about 100 meV upon condensation. The ordering of the NTCDA molecules upon annealing leads to a slight decrease of the line width and to a more pronounced shoulder on the low-energy side of feature B. This trend continues for the transient phase. The most intense peak at 285.7 eV is now very narrow and the low-energy shoulder has developed into a clearly distinguishable peak at 285.4 eV. Moreover, additional peaks can be resolved at 285.5 eV and 285.6 eV as well as 285.8 eV. The energetic separation of these signals from the prominent peaks at 285.4 eV and 285.7 eV corresponds well to the vibronic energy of the NTCDA modes coupled to the C4 1s–$2\pi^*$ and C3 1s–$2\pi^*$ transitions, respectively [19].

Therefore, I straightforwardly interpret the spectrum of feature B of the transient phase as arising from the prominent adiabatic transitions C4 1s–$2\pi^*$ at

285.4 eV and C3 1s–$2\pi^*$ at 285.7 eV with adjacent vibronic states. The main difference to the other condensed and gas phase spectra lies in reduced line widths of the signals involved and in a change in the vibronic envelope associated with an intensity shift towards the adiabatic transition (0–0) in the transient phase.

Dipole-dipole interaction

An explanation for this observation can be given on the basis of the coupling of the transition and charge transfer dipole moments of adjacent molecules which was introduced in Chapter 2. The coupling strength strongly depends on the arrangement of the molecules and on the symmetry of the respective transition moments. In the dipole approximation the coupling strength V_{nm} between molecules n and m can be described by

$$V_{nm} = |\vec{\mu}_n|\,|\vec{\mu}_m| \cdot \left(\frac{\vec{n}_{\vec{\mu}_n}\vec{n}_{\vec{\mu}_m}}{R_{nm}^3} - \frac{3(\vec{n}_{\vec{\mu}_n}\vec{r}_{nm})(\vec{n}_{\vec{\mu}_m}\vec{r}_{nm})}{R_{nm}^5} \right), \tag{5.1}$$

where $\vec{\mu}_n$ and $\vec{\mu}_m$ are the transition dipole moments of molecule n and m, respectively, which are separated by $\vec{r}$. For a C 1s–$2\pi^*$ transition with a dipole moment perpendicular to the molecular plane the coupling is thus largest for a head-to-tail arrangement of the dipoles (commonly referred to as J-aggregates), i.e. a configuration as sketched in Fig. 5.7 a).

The proposed dipole-dipole coupling mechanism is illustrated in Fig. 5.7 b). The C 1s–$2\pi^*$ excitation of molecule A couples to the same transition of the neighboring molecule B.

In Chapter 3, I introduced the oscillator strength in XAS as follows:

$$f \sim |\langle \Psi_f \,|\vec{e}\cdot\hat{p}|\, \Psi_i \rangle|^2 = |M_{if}|^2, \tag{5.2}$$

with the transition matrix elements M_{if} and the initial and final states Ψ_i and Ψ_f, respectively. The oscillator strength is related to the X-ray absorption cross section

$$\sigma_x(E) = C\frac{df}{dE}, \tag{5.3}$$

with $C = \frac{2\pi^2 e^2}{\hbar} = 1.1 \cdot 10^2\,\mathrm{Mb\,eV}$.

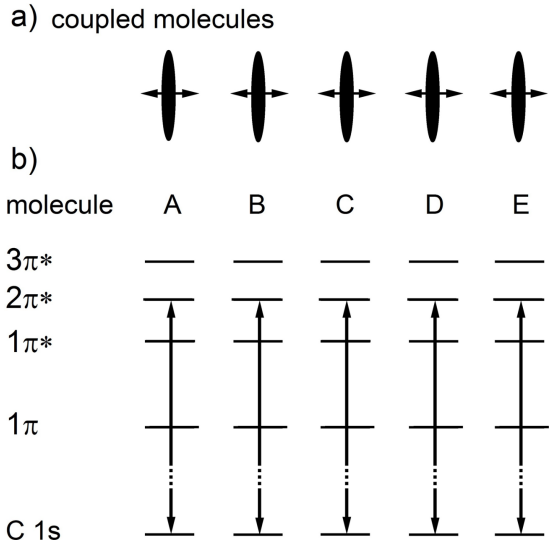

Figure 5.7: a) Illustration of the coupling of NTCDA molecules in the transient phase. The transition dipole moments are oriented perpendicular to the molecular plane. b) Schematic energy level diagram of adjacent NTCDA molecules after resonant core excitation. Proposed coupling mechanism: resonant coupling of the core-to-valence transition for two (or more) molecules. See text for details.

Liu et al. calculated the oscillator strengths of the absolute transition dipole moments for core-to-valence excitations of NTCDA with the FCA/cc-pVTZ and FCA/cc-pVDZ level of theory [166]. His results for core-valence transitions relevant in this chapter are summarized in Table 5.1. For a reasonable fit, the calculated data have to be shifted to fit the NEXAFS spectra. Liu assigns the highest oscillator strength to the central carbon atom and the C4 1s–$2\pi^*$ transition. In the spectrum 5.5 c), this core-valence transition is clearly smaller than the C3 1s–$2\pi^*$ transition. These differences indicate that a quantitative calculation of the transition dipole moment oscillator strength is challenging. Nevertheless, the calculations are useful for a qualitative estimation of the dipole-dipole coupling strength in X-ray absorption in contrast to optical excitation.

The theoretical models presented in Chapter 2 were predominantly applied to optically excited systems. The optical transition dipole moments of valence-to-valence excitations, e.g. 1π–$1\pi^*$, are according to Liu's calculations in the order of 3 a.u. and, thus, nearly 40 times larger than core-excitation dipole mo-

Table 5.1: Absolute transition dipole moments $|\mu|$, excitation energies ΔE, and oscillator strengths f of NTCDA core excitations calculated at the FCA/cc-pVTZ (in parenthesis: FCA/cc-pVDZ) level of theory [166]. For the labeling of the different carbon atoms, see Fig. 5.5 b).

excitation	$\|\mu\|$ (atomic units)	f (atomic units)	ΔE (eV)
C2 1s–$2\pi^*$	0.0251(0.0248)	0.0044(0.0044)	288.6115(290.4266)
C3 1s–$2\pi^*$	0.0453(0.0436)	0.0145(0.0135)	288.1910(290.0549)
C4 1s–$2\pi^*$	0.0760(0.0739)	0.0407(0.0387)	287.8124(289.5649)

ments [56,77]. From equation 5.1 follows that the coupling strength V_{nm} is proportional to the product of the transition dipole moments

$$V_{nm} \propto |\vec{\mu}_n|\,|\vec{\mu}_m|\,. \tag{5.4}$$

Therefore, the coupling of the core-excitation transition dipole moments is about 1600 times smaller than that of the valence-to-valence excitations of optically excited molecules.

From the energy shift of 80 meV of the adiabatic transitions (0–0) in Fig. 5.6, I can evaluate the transition dipole moments $|\vec{\mu}|$ with the help of equation 5.1. For coplanarly arranged dipoles as sketched in Fig. 5.7, this equation can be reduced to equation 2.11 which can be rewritten as:

$$|\vec{\mu}_n|\,|\vec{\mu}_m| = \left(\frac{V_{nm}\cdot R_{nm}^3}{1-3\cos^2\theta}\right). \tag{5.5}$$

If I assume that all transition dipole moments are of the same magnitude, the molecular planes are 3 Å apart, and $\theta = 0$, the calculated transition dipole moments are $|\vec{\mu}| = 0.37$ a.u. and, thus, fall in between the core-valence and optical dipole moments of 0.045 a.u. and 3 a.u., respectively, calculated by Liu.

The discrepancy between the results and the calculated transition dipole moments might question the dipole-dipole approach, i.e. the dipole approximation which is usually applied for core-valence excitations. For very dense molecular packings where the intermolecular distance of around 3 Å is much smaller than the size of the NTCDA molecule (∼9 Å along the long axis), the dipole approximation might reach its limitations. Scholes et al. [34] investigated the contribution of higher orders of interaction beyond the dipole approximation for aromatic molecules. They conclude that higher order terms, i.e. dipole-octopole and

octopole-octopole, may be important at short distances. They also showed that the orientation dependency of those terms is similar to that of the dipole-dipole interaction.
In addition to higher order effects, also the wave function overlap of neighboring dye molecules can make an additional contribution on which I will focus next.

Wave function overlap

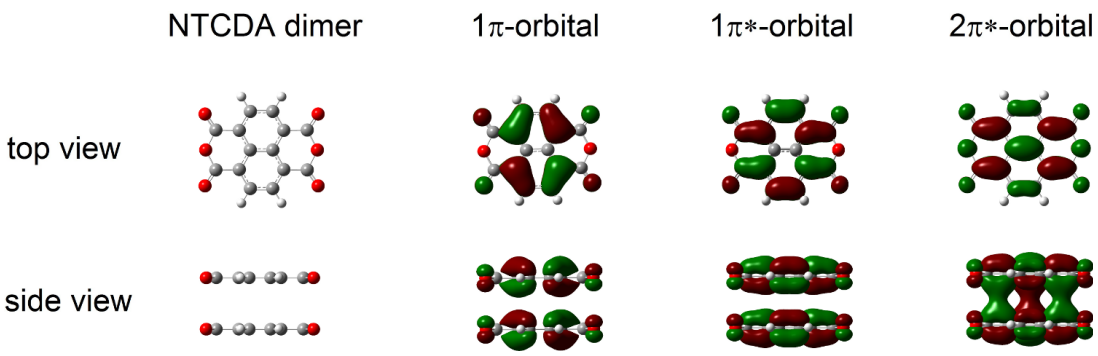

Figure 5.8: NTCDA dimer orbitals calculated at the UB3LYP/6-31G(d,p) level of theory. The centers of the molecules are 3.4 Å apart. The cutoff isodensity values are the same for all orbitals. See text for more details.

For closely packed π-conjugated molecules in a face-to-face arrangement, neighboring dyes can have a considerable overlap of the frontier-orbital wave functions [7,57–59]. This leads to increased intermolecular charge transfer (CT) transition dipole moments [66,67]. This so-called short-range component of the coupling becomes already significant at relatively long distances, e.g. for naphthalene dimers at a separation of about 6 Å [34], and can thus be expected to be substantial in the present case where the intermolecular distance between the NTCDA molecules is only around 3 Å.

In Fig. 5.8, I present the molecular orbitals 1π, $1\pi^*$ and $2\pi^*$ of a NTCDA dimer. The dimers were composed of two NTCDA molecules with an optimized molecular geometry for a single molecule. The molecular planes are 3.4 Å apart. The orbitals were calculated for the ground state at the UB3LYP/6-31G(d,p) level of theory and are all depicted at the same isodensity cutoff value. The effects of the core hole on the final state are therefore not included. Nevertheless, I can

make some quantitative statements about how the orbital shape is affected by adjacent dye molecules in a face-to-face arrangement. In the top view, the orbitals correspond well to a single NTCDA dye molecule [167]. In the side view, the 1π and $1\pi^*$ orbitals still resemble the orbitals of an isolated NTCDA molecule whereas the $2\pi^*$ orbital differs from the monomer orbital. Due to the close-packed and face-to-face arrangement the $2\pi^*$ orbitals overlap which results in a high electron density between the two molecules. This additional electron density can explain an additional CT transition dipole moment. In Chapter 2.1.3, I presented Mulliken's approximation for the CT transition dipole moment as follows:

$$\vec{\mu}_{nm} = -e \int d^3r \; \vec{r} \times \rho_{n,m}(\vec{r}) \approx -e\vec{R}_{n,m} \int d^3r \rho_{n,m}(\vec{r}), \tag{5.6}$$

where $\vec{R}_{n,m}$ is the average position of the transition electron density $\rho_{n,m}$. The location of the CT electron density is determined by the overlap of the initial-state $1s$ and the final-state $2\pi^*$ orbitals. The direction of the CT transition moment points from the initial state towards the CT density. For closely packed NTCDA molecules, as illustrated in Fig. 5.7 a), the CT transition moment is aligned perpendicular to the molecular plane and along the electric field vector of s-polarized light at grazing incidence.

Coherent exciton scattering approximation

The changes in the vibrational envelope observed in the NEXAFS data can be explained in the framework of the coherent exciton scattering (CES) approximation [21,47,48,50]. In Section 2.1.2, I derived the following expression:

$$\langle G \rangle = \langle g \rangle + \langle g \rangle \, V \, \langle G \rangle \,, \tag{5.7}$$

where $\langle g \rangle$ is the mean of the single-molecule Green's function in its vibronic and electronic ground state and $\langle G \rangle$ is the Green's function for interacting molecules. This one-particle Green's function approach obeys Dyson's equation and describes the excitation of coherently delocalized quasi-particles. In other words, this means that the hole-electron pair propagates to the adjacent molecule rapidly compared to the molecular vibration frequencies. Therefore, the originally excited molecule remains preferentially in its vibrational ground state. As a result the intensity is shifted towards the adiabatic transition within the vibrational envelope observed in the experiment.

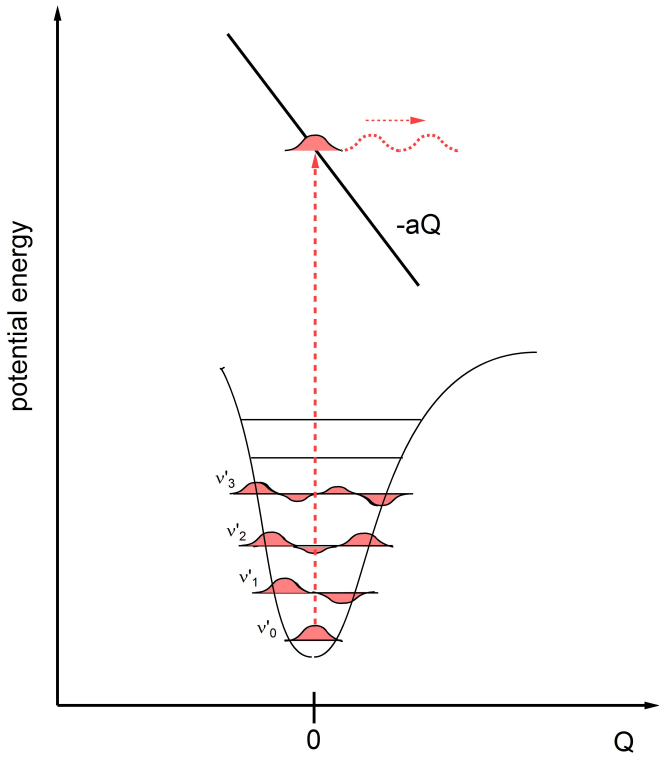

Figure 5.9: Potential energy surfaces in the CES approximation. The lower energy surface is given by a Morse potential and the upper potential by a linear function [168]. See text for more details.

In Fig. 5.9, I present a diagram of the potential energy surfaces in the CES approximation. The ground state potential curve is a simple harmonic potential. In the CES approximation, the upper state can be represented by a linear potential $-aQ$ with the slope a and the normal coordinates Q [168]. Due to different boundary conditions of the upper linear potential no higher vibrations in the excited state are possible. Therefore, the absorption spectrum consists of a single absorption peak.

This is illustrated by Fig. 5.10, which shows the results of CES calculations of the vibronic progressions of a single molecule and of coupled molecules in the configuration sketched in Fig. 5.7 a) [169]. I modeled the Franck-Condon factors $|f^{\alpha}|^2$ of the ground vibrational states ν according to

$$|f^{\nu}|^2 = \frac{\lambda^{\nu}}{\nu!} \exp(-\lambda) \tag{5.8}$$

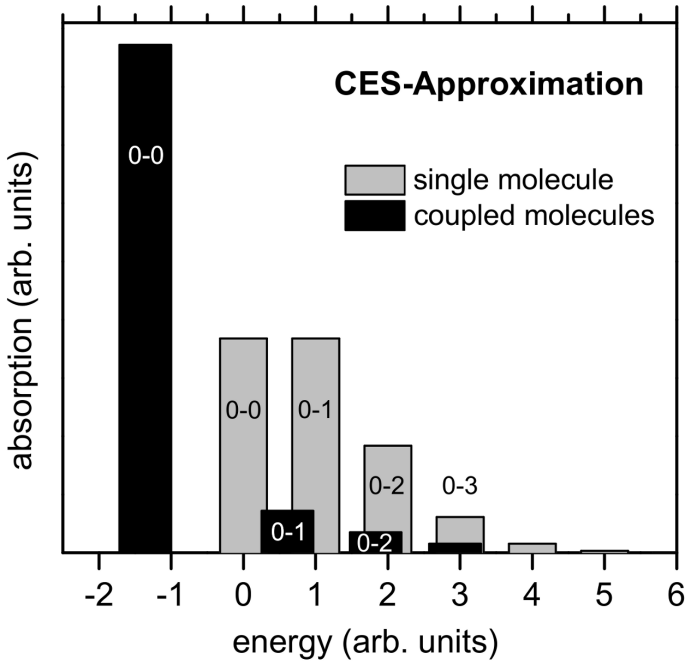

Figure 5.10: Results of coherent exciton scattering calculations: The adiabatic component of the electronic excitation (0–0) and the corresponding vibronic progression (0–1, 0–2, 0–3) are plotted for isolated (gray) and coupled molecules (black). See text for details.

with the Huang-Rhys factor λ. The intensity ratios of the adiabatic transition (0–0) to the higher vibrational states (0–1, 0–2 and 0–3) change markedly and in case of a sufficiently strong coupling the all oscillator strengths accumulates in the 0–0 transition. Moreover, a marked energy shift of the entire vibronic progression towards lower energy can be observed in the case of coupled molecules. This result matches the experimental observation qualitatively (see Fig. 5.6 a)).

Coherent length of a core hole-electron pair

In the transient phase I also observe a reduced line width of the C 1s–$2\pi^*$ transitions, as evident in Fig. 5.11. Jelly, Scheibe, Frank and Teller were the first to investigate the emergence of an unusually sharp and redshifted absorption peak, the so-called *J-band*, upon aggregation of pseudo-isocyanine (PIC) dye molecules in water [170–172]. They described this peculiar behavior as a result of a collective excitation of all aggregated molecules, i.e. a collective electronic eigen-

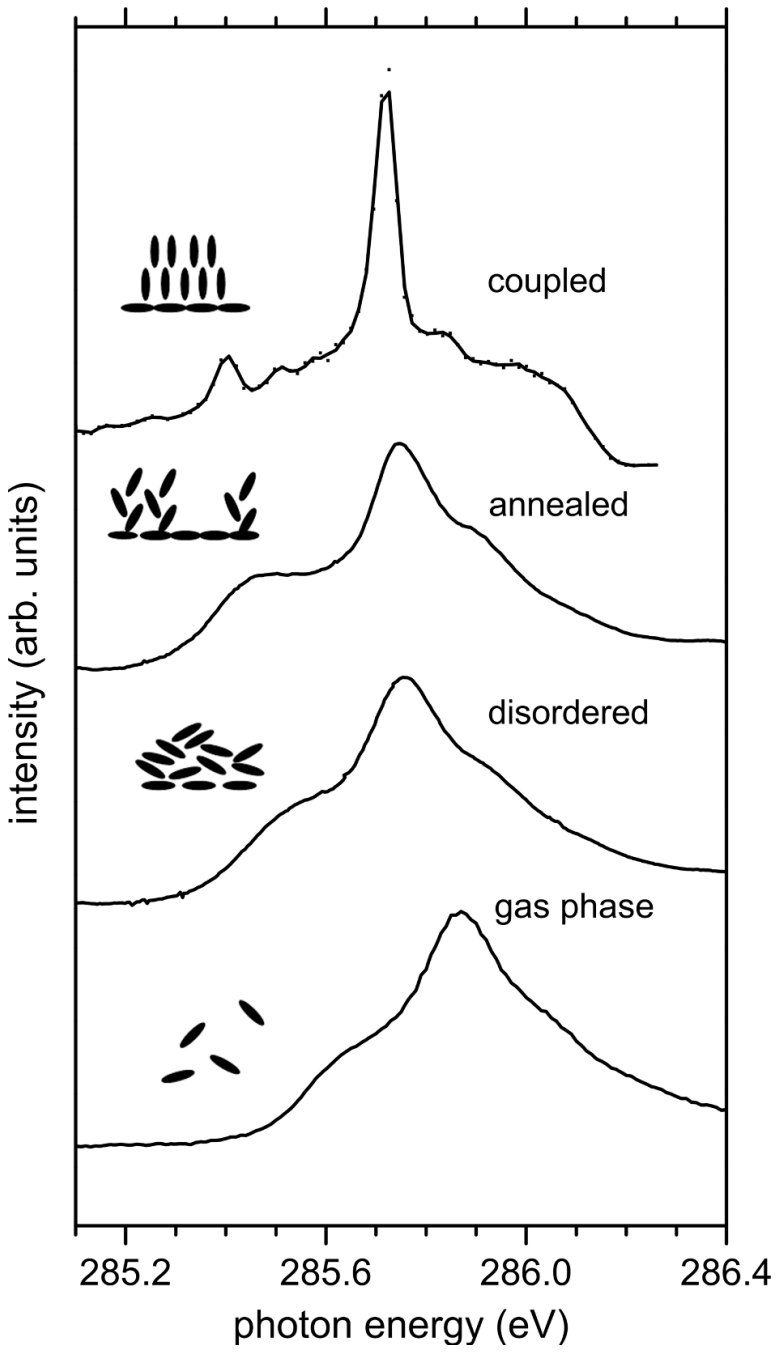

Figure 5.11: NEXAFS spectra of NTCDA feature B in the gas phase [165], in the disordered condensed phase [19], in the ordered condensed phase after annealing [19], and in the transient phase. The spectra were normalized for better comparison of the line shape.

state of the coupled molecules. In the following years, many theoretical models were developed to tackle the question of the unusual sharpness of the absorption peak [37, 50, 51, 173–177].

As discussed in the previous paragraph, in the CES approximation (see Section 2.1.2) the change of the vibronic structure is the result of the fast exciton transfer between adjacent molecules. Therefore, no vibrational waves can be developed in the excited state before the exciton passes to the next molecule. Also, the peak width of an Gaussian absorption peak decreases in the CES approximation. However, the coherence length of the core hole-electron cannot be extracted from this model [51].

Also Knapp explored the unusual peak narrowing of aggregated molecules [178] which is known as *exchange narrowing*. He assumed that the excitation energy is slightly different for every molecule due to the slightly different interaction of every individual molecule with its surrounding. In his pure electronic Hamiltonian for coupled molecules the interaction with the surroundings enters as a diagonal disorder. He then showed that in the strong-coupling limit the linewidth of the absorption signal decreases according to

$$\Delta \propto \frac{1}{\sqrt{N}}, \tag{5.9}$$

where Δ is the FWHM of the absorption signal and N the number of coherently coupled molecules. The linewidth narrowing as given by Knapp's equation is often interpreted as a direct consequence of the exciton delocalized over several molecules. Due to this delocalization the exciton state is averaged over the different inhomogeneities of the individual molecules and, as a result, the collective absorption peak is narrower than the optical response of a single molecule.

For a quantitative analysis, the full widths at half maximum (FWHM) of the gas phase and transient phase absorption spectra were evaluated, yielding $211\,(\pm 10)$ meV and $74\,(\pm 10)$ meV, respectively, for the most prominent signal in the spectra shown in Fig. 5.11. With the FWHM derived from the NEXAFS data of isolated and coherently coupled molecules, i.e. $\Delta_{\text{isol.}}$ and $\Delta_{\text{coup.}}$, respectively, the number of coherently coupled molecules in the transient phase can be estimated to be 8 ± 3.

Exciton band structure

For a long chain with N molecules coupled by dipole-dipole interactions and arranged as depicted in Fig. 5.7, the exciton band is characterized by a Bloch-type exciton wave function [48]

$$|\Psi_k\rangle = \frac{1}{\sqrt{N}} \sum_n \exp(ikn)\,|\pi_n\rangle, \tag{5.10}$$

where $|\pi_n\rangle$ is a Hartree product of single molecular wave functions of the excited molecule n and k is the wave vector, as defined in Chapter 2. For the sake of simplicity, periodic boundary conditions are assumed. The corresponding eigenenergies are, consequently, given by

$$E_k = E_0 + 2 \cdot V_{nm} \cos(k), \tag{5.11}$$

with E_0 being the monomer transition energy. The value of the dipole-dipole coupling V_{nm} was extracted from the 80 meV energy shift of the adiabatic transition shown in Fig. 5.6. With equation 5.5 I obtain for molecules arranged as depicted in Fig. 5.7 a coupling constant V_{nm} = -40 meV. The exciton band structure calculated with this value is presented in Fig. 5.12. For J-aggregates only the states at the Gamma point, i.e. k = 0, are optically allowed and, consequently, the full oscillator strength is concentrated in the lowest transition [48, 177].

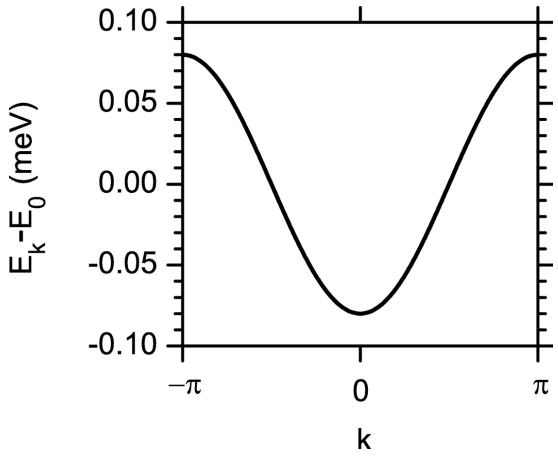

Figure 5.12: Exciton band structure for nearest-neighbor interactions with V_{nm} = -40 meV. For J-aggregates and at the Gamma point k = 0, the energy minimum is -80 meV.

Förster energy transfer rate

Förster investigated dipole-dipole coupling in great detail and derived an expression for the so-called resonant energy transfer (RET) between molecules. Based on Fermi's golden rule, Förster found an expression for the probability per unit time that the occupation probability of an electronic state is transferred from molecule n to molecule m.

In Chapter 3, I introduced Fermi's golden rule for the XAS process and derived the probability per unit time for a transition from an initial state into a final state. Förster expressed the energy transfer rate between molecules n and m by Fermi's golden rule and obtained:

$$k_{nm} \sim \frac{2\pi}{\hbar} \left|\langle \varphi_m^e \varphi_n^g \left| V_{nm} \right| \varphi_m^g \varphi_n^e \rangle\right|^2 \delta(E_m^e + E_n^g - E_n^e - E_m^g), \tag{5.12}$$

where φ_n^g and φ_m^g are the initial states and φ_n^e and φ_m^e are the final states for molecules n and m, respectively, and V_{nm} is the coupling strength. For the energy transfer time ω thus follows:

$$\omega \propto \frac{\hbar}{V_{nm}}. \tag{5.13}$$

For optically excited systems of strongly coupled molecules, energy transfer times of $\sim 10^{-15}$ sec were reported [20, 179]. With the Heisenberg's uncertainty principle,

$$\Delta E \cdot \Delta t \geq \frac{\hbar}{2}, \tag{5.14}$$

the energy transfer time in the transient phase can be derived from the peak width of the absorption spectra.

For a FWHM of 74 ± 10 meV of the absorption peaks in the transient phase, the lifetime of the core hole can be estimated to be $\sim 4 \cdot 10^{-15}$ sec. Such a lifetime is on the same order as the energy transfer time between strongly coupled molecular systems [20, 179]. Therefore, a delocalization of the exciton over ~ 10 molecules for $\sim 4 \cdot 10^{-15}$ sec is reasonable. It has to be stressed that Förster derived the RET expression for dipole-dipole coupled systems only. Therefore, it does not include any additional contribution due to molecular-orbital overlap. Different spectroscopic methods, e.g. core-hole clock spectroscopy [180–182] and time-resolved two-photon photoemission [183–185], show that charge transfer, i.e. electron transfer, is also on the order of several femtoseconds [180–182]. Thus, an additional contribution to the energy transfer time due to the molecular orbital overlap does not contradict the estimation done with Förster's RET expression.

5.2.4 Conclusion

I have reported on X-ray absorption experiments which demonstrate the importance of a correct consideration of the core hole-electron correlation for condensates of organic molecules. During the transition from a disordered to an ordered film arrangement, a transient phase occurs for NTCDA on Ag(111) which is characterized by a distinctly different spectral signature. The spectra of this transient phase exhibit a reduced line width and a redshift as well as a substantial change in the vibronic profile. All these experimental observations can be explained by the coupling of dipole moments of adjacent molecules. The corresponding model is well established for optical spectroscopy methods.

This result has two immediate implications: Firstly, it shows that the excitation is delocalized over several molecules; a number of about 10 can be determined from the data. In consequence, the experimental results provide evidence for an intermolecular delocalisation of the core hole which is involved in the excitation. Secondly, the very exact and complete explanation of the experimental data by this model based on the coupling of transition dipoles strongly suggests that the oscillator strengths of the transition dipole moments involved in the core-to-valence excitations are substantially larger than estimated on the basis of calculations on isolated molecules. This difference may be explained by the additional contribution of the wave function overlap between neighboring molecules [60, 61]. Further efforts to develop a comprehensive theoretical description of the core excitation in molecular condensates are thus highly desirable.

5.3 Structural phase dynamics in NTCDA multilayer films

Opto-electronic devices based on organic materials offer a variety of applications and have already entered the mass market [80, 81]. All such devices have in common that they are based on multiple layers of organic semiconducting materials. To optimize the crucial performance parameters, e.g. the charge carrier mobility, of the organic films, a comprehensive understanding of the interplay between film morphology, geometric structure, and electronic structure is crucial.

In this chapter, I present the results of real-time measurements of the formation of a three-dimensional, stable geometric structure of thin films of organic molecules which follows the deposition of an initially amorphous film. The complex underlying physics makes it challenging to model and predict the structure formation in organic thin films. For a comprehensive understanding specific case studies on well-defined model system are thus mandatory. In particular, information on the processes involved in establishing the final structural arrangement, such as diffusion and the organization in transient phases, is highly desirable. Therefore, experimental techniques with appropriate time resolution are essential [24].

In my investigations I employed energy-dispersive near-edge X-ray absorption fine structure (NEXAFS) spectroscopy and time-dependent photoemission spectroscopy. Using NTCDA films on Ag(111) surfaces as a model system, I utilized energy-dispersive NEXAFS as a novel method to study the post-growth process. During the structure formation I could distinguish several sub-processes involved in the post-growth process. From their time-dependency I quantified thermodynamic parameters, e.g. the activation energy of kinetic processes.

5.3.1 Sample preparation and experimental setup

All experiments were performed in a UHV chamber with a base pressure below $2 \cdot 10^{-10}$ mbar. The Ag single crystal preparation followed the standard sputtering and annealing procedure described in the literature [186]. The NTCDA films were prepared *in situ* by organic molecular beam deposition from a home-built Knudsen cell at a rate of about 0.2 monolayer (ML) per minute and at a substrate temperature of 95 K. The NTCDA was purified by double sublimation prior to deposition. The film thickness was determined by the attenuation of the Ag 3d photoemission signal excited with an Al-K_α X-ray source [106]. For accurate temperature measurements in the temperature-dependent experiments, a thermocouple was mounted close to the sample onto the sample holder. By cooling with liquid nitrogen and heating with a filament, sample temperatures between 95 K and 800 K could be achieved and were stablized by a proportional-integral-differential (PID) controller. For filament currents below 4 A which were sufficient in the experiments presented in this work to access the temperature regime between 95 K and 230 K, no artifacts were observed in the NEXAFS and photoelectron spectroscopy (PES) data.

The energy-dispersive NEXAFS measurements were performed at the beamline UE52-PGM of the BESSY II synchrotron light source of the Helmholtz-Zentrum Berlin [83,131]. For a detailed discussion of the energy-dispersive mode see Chapter 4.

5.3.2 Experimental results

Time-dependent energy-dispersive NEXAFS

For time-dependent X-ray absorption spectra (Fig. 5.13 c)) the C *KLL*-Auger electrons of NTCDA in the rage of 252–278 eV kinetic energy and in the dispersive photon energy window between 284.75 eV and 286.3 eV were probed. For every single C *KLL*-Auger electron spectra I averaged for 6 sec. The total measurement time for energy-dispersive measurements was between 30 min and 50 min. All time-dependent measurements were normalized to the ring current. Within the chosen excitation energy window, the electronic response of C4, C3 and C2 1s core electron excitations of the naphthalene backbone into the second-lowest unoccupied molecular orbital $2\pi^*$ were probed (Fig. 5.13 b), feature B, shaded region). In the following I will concentrate on feature B (Fig. 5.13 b) and d)) because the

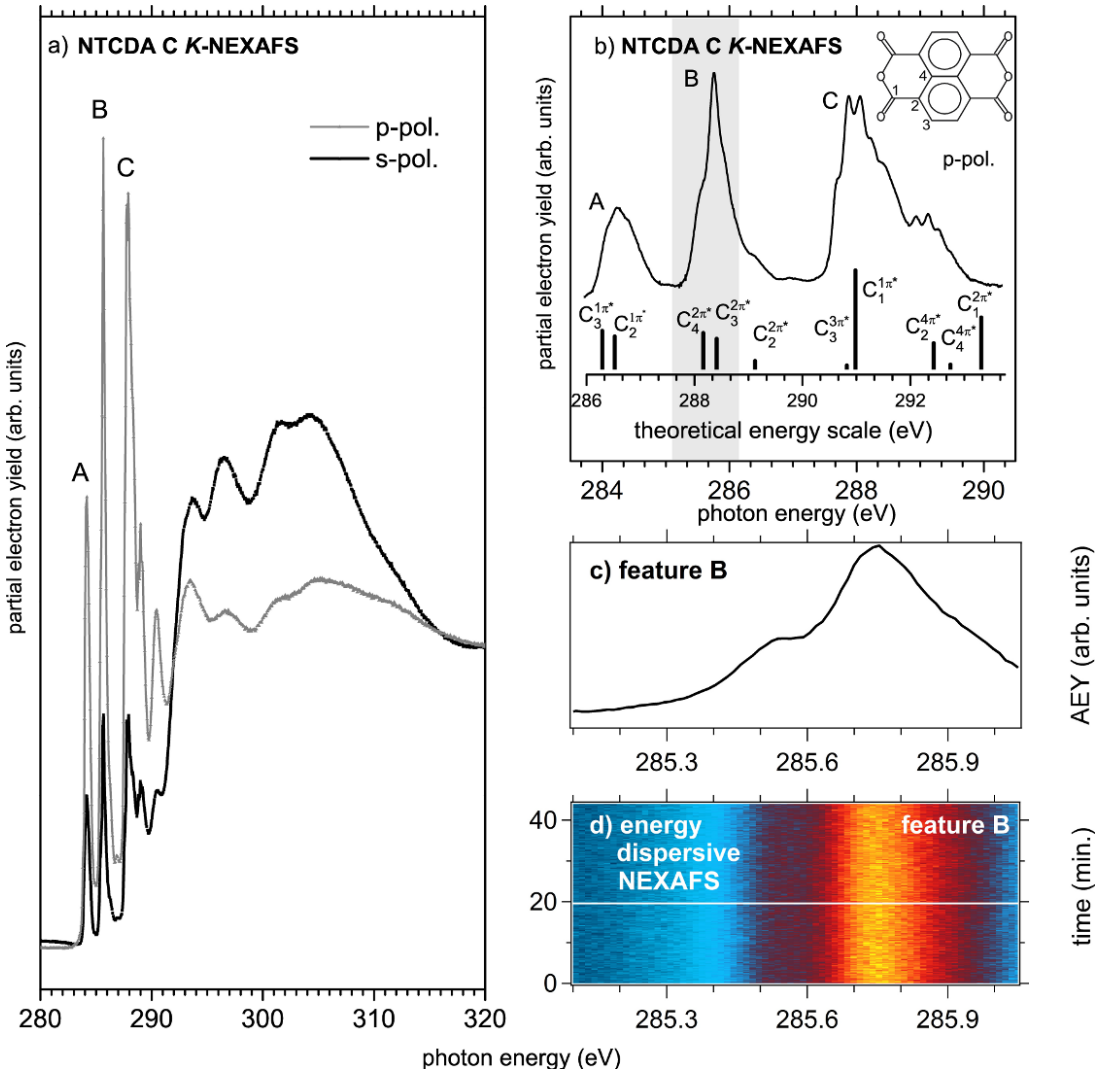

Figure 5.13: a) C *K*-NEXAFS spectra of an NTCDA multilayer film prepared on Ag(111) at a temperature of 95 K. The spectra were recorded with *s*- and *p*-polarization in the traditional beamline mode. b) π^*-region of the *p*-polarized spectrum plotted on an expanded energy scale. The most prominent signals are denoted by A, B and C and the shaded region indicates the photon energy window probed in the dispersive mode. Below the spectrum the result of an *ab-initio* calculation is displayed [164]. Note that the theoretical energy scale is shifted and scaled to fit the experimental data. c) NEXAFS signal of feature B recorded with *p*-polarization in the dispersive mode and averaged over 6 sec. d) Set of dispersive NEXAFS spectra recorded over ca. 45 min at a constant sample temperature of 95 K to demonstrate beamline stability and absence of radiation damage. The white line at t=20 min marks the position of the single spectrum plotted in c).

1s–$2\pi^*$-resonances are well separated in the absorption spectra. Moreover, these core-valence transitions are located at the aromatic core and are sensitive to intermolecular interactions, as shown in Section 5.2.

All films investigated in the following post-growth study were 8–10 ML thick and prepared at a substrate temperature of 95 K. This results in smooth films [147] with molecules preferentially lying flat on the substrate, as demonstrated by the strong linear dichroism [104] in the NEXAFS data presented in Fig. 5.13 a). Due to the symmetry selection rules for planar molecules such as NTCDA, strong absorption occurs for the C $1s$–π^*-transitions if the $\vec{E}$-vector of the incoming light is perpendicular to the molecular plane and a weak absorption if it is parallel to the molecular plane.

Fig. 5.14 shows the results of a time-resolved and energy-dispersive NEXAFS experiment which monitors the transition from flat-lying to upright-standing molecules induced by annealing the films to 200 K. Fig. 5.14 b) and c) present sequences of energy-dispersive NEXAFS spectra recorded with *s*- and *p*-polarization, respectively. In Fig. 5.13 a) and d) the single NEXAFS spectra are presented which I extracted at the positions indicated in b) and c), respectively. The data set starts after preparation of the film at 95 K at $t = $-3 min. The sample was then quickly (i.e. in less than 1 min) heated to 200 K. $t = 0$ refers to the time when a constant temperature of $T = 200$ K was established. Fig. 5.14 b) and c) consistently show that annealing leads to an increase in the intensity of the NEXAFS feature B for *s*-polarization. For *p*-polarization a decrease occurs at the same time. This can immediately be associated with the expected change in molecular orientation from flat-lying to upright.

For a quantitative analysis of the time evolution the intensity of NEXAFS feature B in Fig. 5.14 b) and c) was integrated over the photon energy and plotted against time. The integrated intensity spectra along with the time-dependent NEXAFS results shown in Fig. 5.14 b) and c) are presented in Fig. 5.15 c). Moreover, for a better illustration of the intensity changes the first derivatives of the integrated NEXAFS signals are displayed on the right-hand side of Fig. 5.15 c). The data were normalized in a way that the ratio of the integrated intensities of feature B recorded with *s*- and *p*-polarization before annealing (i.e. at $t \leq$ -1 min) corresponds well to the respective intensity ratio of the NEXAFS spectra obtained with the traditional setup (see Fig. 5.13 a).

The curves in Fig. 5.15 c) show very characteristic changes that can be divided into four sections labeled I to IV, as indicated on the left-hand side. In sec-

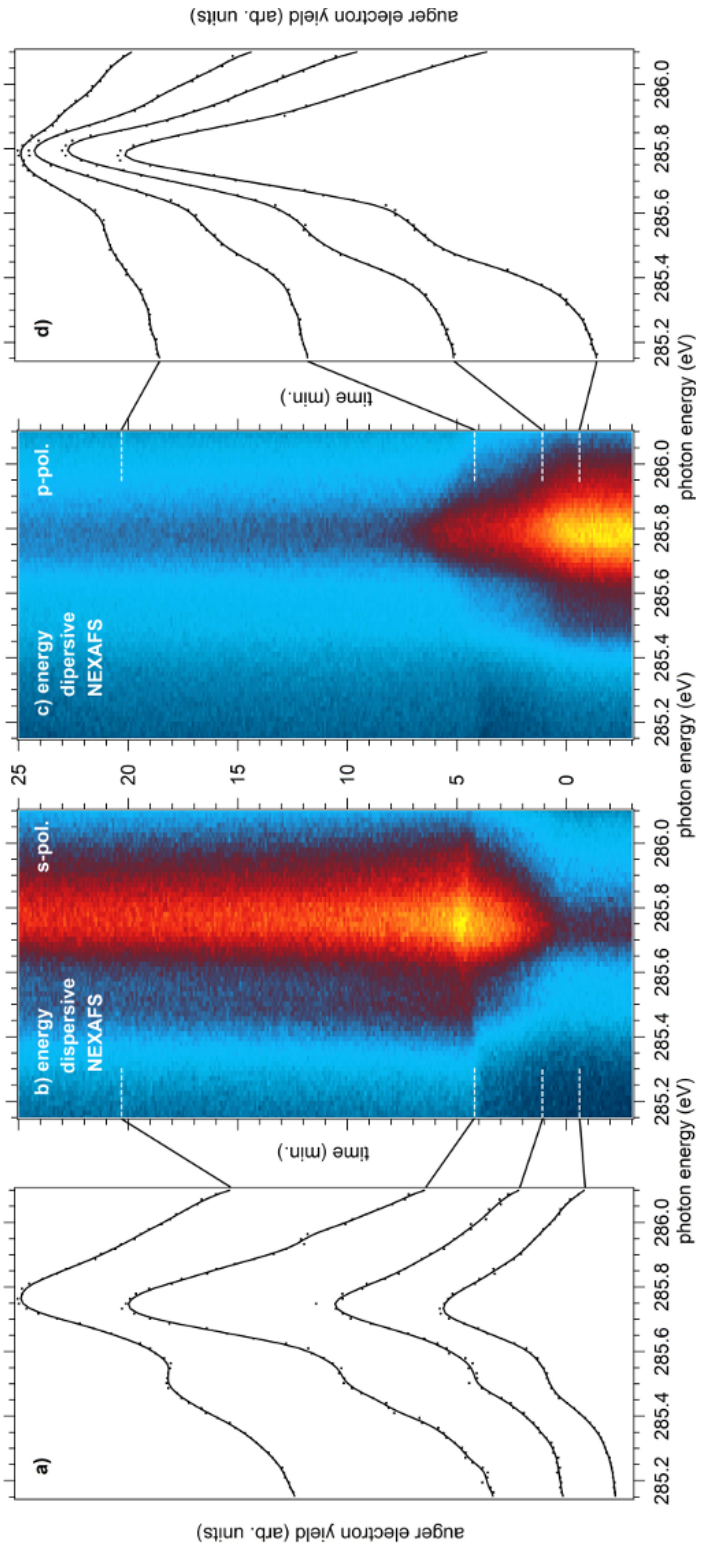

Figure 5.14: Time-dependent energy-dispersive NEXAFS study of a NTCDA/Ag(111) sample (film thickness 8 ML, prepared at 95 K) after annealing to 200 K. The time evolution of the C *K*-NEXAFS spectra of feature B (see Fig. 5.13) recorded with *s*- and *p*-polarisation of the incident light are displayed in colour-coded plots in b) and c), respectively. Yellow represents high and blue low intensity. The data acquisition was started before heating, i.e. at $t = -3$ min. The sample was heated quickly and at $t = 0$ a stable temperature of 200 K was established. Spectra a) and d) are single NEXAFS spectra extracted from b) and c), respectively, by integration over 0.5 min at the specific position indicated by the dashed lines ($t = -0.6$ min, $t = 1.1$ min, $t = 4.2$ min, and $t = 20.3$ min).

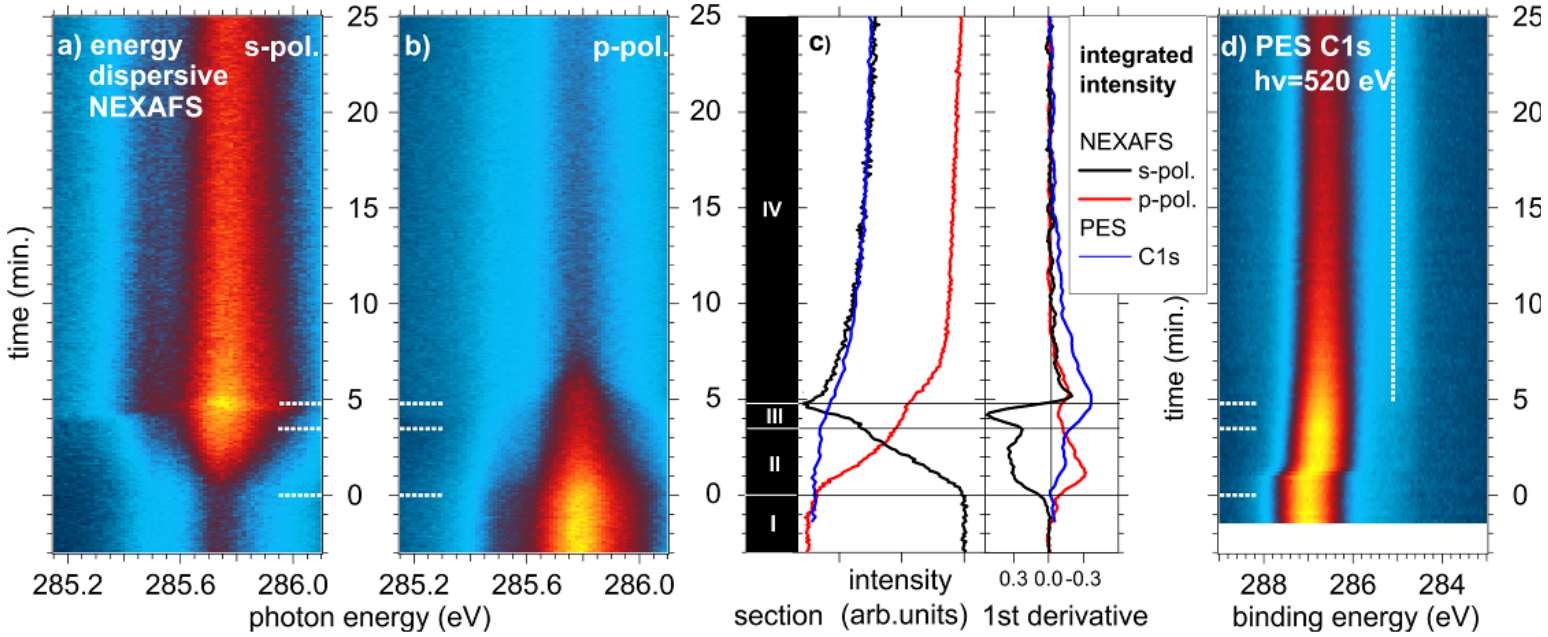

Figure 5.15: Time-dependent NEXAFS study of a NTCDA/Ag(111) sample (film thickness 8 ML, prepared at 95 K) after annealing to 200 K. The time evolution of the C *K*-NEXAFS spectra of feature B (see Fig. 5.5) recorded with *s*- and *p*-polarisation of the incident light are displayed in colour-coded plots in a) and b), respectively. Yellow represents high and blue low intensity. The data acquisition was started after sample preparation at $t = -3$ min. The sample was heated quickly and at $t = 0$ a stable temperature of 200 K was established. c) Integrated intensity (left) and first derivative (right) of NEXAFS feature B with *s*-polarisation (black) and *p*-polarisation (red), derived from the data in a) and b), respectively. The general characteristic changes can be divided into four sections, labeled I to IV. The blue traces represent the C 1s intensity integrated between 288.0 eV and 285.8 eV and the first derivative, respectively, taken from the data in d). d) Time-dependent PES data of NTCDA/Ag(111) (film thickness 8 ML, prepared at 95 K) in the C 1s regime ($h\nu = 520$ eV), recorded up to 25 min after heating to 200 K. See text for details.

tion I, directly after preparation and before the sample temperature has reached 200 K, the intensities in *s*- and *p*-polarization are constant and the slope consequently is zero. Upon heating (section II), the intensity in *p*-polarization decreases while it increases in *s*-polarization. The absolute values of the slopes in *s*- and *p*-polarization are similar until in section III the increase in intensity in *s*-polarization is significantly larger than the decrease in *p*-polarization. The corresponding time window between 3.5 and 4.8 min is small and delimited by a relatively sharp intensity maximum in *s*-polarization which is followed in section IV by a parallel decrease in intensity in *s*- and *p*-polarisation with an almost identical slope.

While the time evolution of the NEXAFS intensity in section II can straightforwardly be associated to a change in molecular orientation from flat-lying to upright, sections III and IV immediately reveal that the post-growth annealing behavior of the NTCDA films is more complicated.

Time-dependent photoelectron spectroscopy

Additional information can be derived from time-dependent C 1s PES measurements which are presented in Fig. 5.15 d). For the chosen photon energy of 520 eV, the kinetic energy of the photoelectrons and, thus, also the information depth of 2–3 ML [106] is similar to that of the *KLL*-Auger electrons in the NEXAFS measurements. The experimental procedure was analogous to that of the NEXAFS measurements described above, i.e. the film (coverage 8 ML) was prepared at 95 K and subsequently annealed at a temperature of 200 K which was established at $t = 0$ min. The colour-coded plot in Fig. 5.15 d) immediately reveals a prominent shift in the energetic position of the C 1s signal towards lower binding energy, which sets in after the sample has been at 200 K for about 1 min.

Moreover, Fig. 5.15 d) shows that the C 1s intensity decreases substantially in sections III and IV. The integrated intensity of the C 1s signal between 288.0 eV and 285.8 eV and the first derivative are compared to the corresponding curves (blue traces) derived from the NEXAFS data shown in Fig. 5.15 c). The C 1s intensity curve was normalized to the intensity of the NEXAFS measurement with *p*-polarization at $t = 0$ and scaled to match the respective *s*-polarization curve at $t = 25$ min.

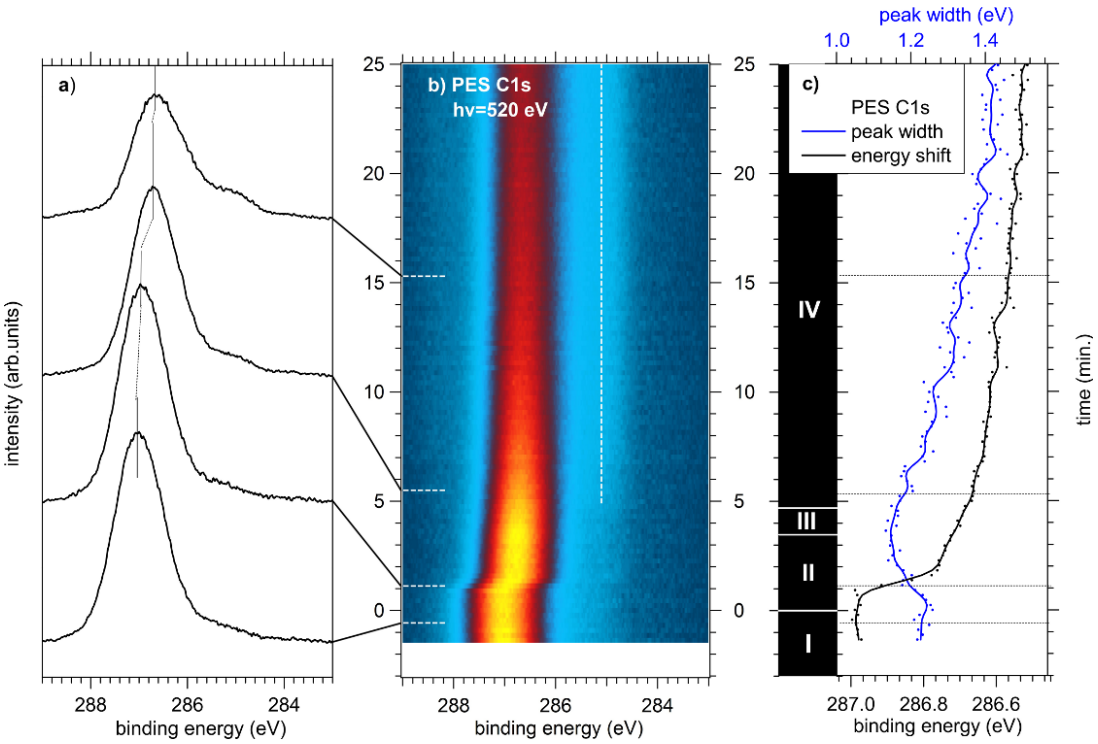

Figure 5.16: a) PES spectra obtained by integration of the time-dependent C 1s measurements shown in b) at $t = -0.6$ min $t = 1.1$ min, $t = 5.5$ min, and $t = 15.3$ min. The vertical lines indicate the energy shift. In c) I present the time evolution of the energy shift of the peak maximum (black trace) and the FWHM peak width (blue trace) of the multilayer C 1s signal. The photoemission lines were fitted with Voigt profiles with a constant Lorentzian lifetime of 85 meV and a Tougaard background.

In section I, the C 1s intensity is constant and the energy position is stable at 286.98 eV. In section II, however, a large energy shift of about 230 meV towards lower binding energy occurs after the sample has been at 200 K for about one minute. This is accompanied by a decrease in C 1s intensity, as evidenced by the negative value of the corresponding first derivative. Subsequently, the peak position shows an almost linear shift towards 286.63 eV until the end of section III and asymptotically approaches 286.52 eV in section IV. The intensity also decreases steadily but shows the most prominent change at the transition between sections III and IV.

Also, the peak FWHM of the C 1s peak becomes smaller in section II and III within the first four minutes and after annealing. The C 1s core level in Fig 5.16 c)

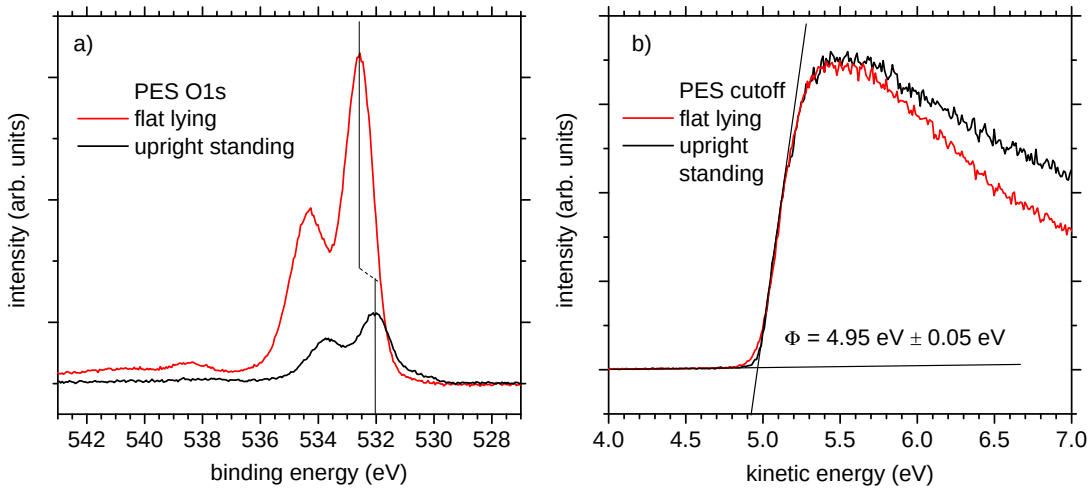

Figure 5.17: Photoemission spectra of the O 1s core level and the work function of nearly flat-lying (red trace) and upright standing (black trace) molecules. Both films were prepared at 95 K and annealed at 200 K. a) The O 1s core level shifts about 0.5 eV to lower binding energy after annealing. The energy shift is indicated by the vertical black lines. b) The work function was determined at the intersection of the horizontal and vertical lines and remains constant at 4.95 eV±0.05 eV after annealing.

was fitted with a Voigt profile with a constant Lorentzian lifetime of 85 meV and a Tougaard background. In section I, the C 1s core level has a FWHM of about 1.20 eV. In section II, the FWHM becomes narrower. The FWHM is smallest in section III. At this position, the FWHM is about 80 meV narrower than in section I. About four minutes later but still in region III, the FWHM increases again. At the end of the experiment, the peak width is about 1.45 eV and, thus, 250 meV wider than in section I. The C 1s core level measurements were complemented with O 1s spectra and measurements of the work function which are presented in Fig. 5.17 a) and b), respectively. The 9 ML thick films were prepared at 95 K and measurements were performed before and after annealing at 200 K. Also the O 1s core level shifts 0.5 meV to lower binding energy after annealing. Remarkably, the work function remains constant at 4.95 eV±0.05 eV upon annealing.

A similar behavior was found with time-dependent PES measurements of the valence regime (VR) between 7 eV and 0 eV binding energy, which I present in Fig. 5.18 b). For a better comparison of the striking similarities between the core level and valence regime measurements, the results of the C 1s measurement are repeated in Fig. 5.18. Note that for a better contrast in the VR spectra the

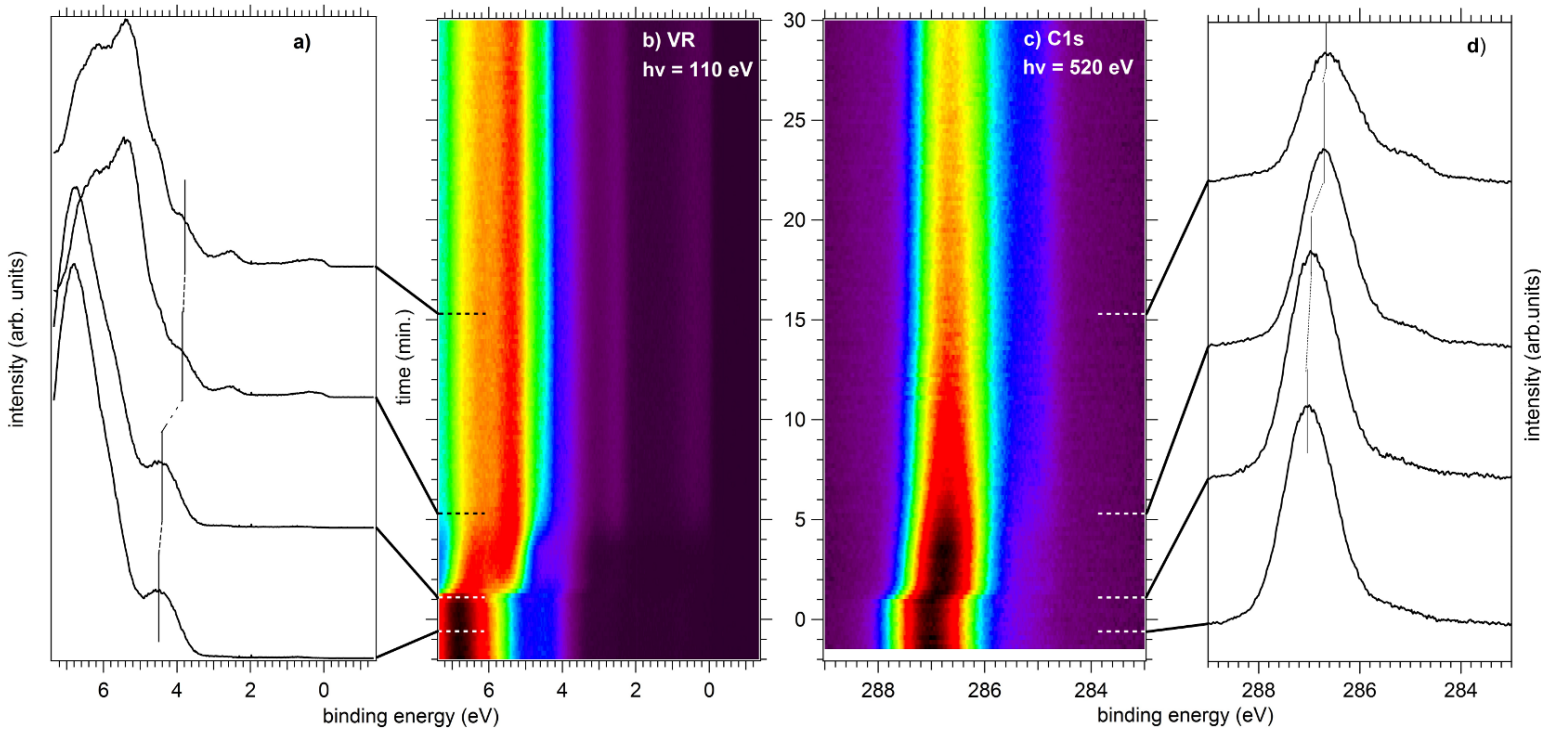

Figure 5.18: a) Photoemission spectra of the valence region derived by integration of the intensity map shown in Fig. b) over 0.5 min at the times indicated by the horizontal dashed lines. The vertical lines indicate the energy shift of the corresponding peak. b) 2D colour map of the time evolution of the valence region photoemission spectra. Red refers to high and blue to low intensity. c) 2D colour map of the photoemission spectra of the C 1s core level. d) Photoemission spectra of the C 1s core level derived by integration of the intensity map in Fig. c) over 0.5 min at the times indicated by the horizontal dashed lines. The slanted lines indicate the energy shift of the C 1s peak. For both measurements, 8 ML thick films were prepared at 95 K. At t = -1 min, the samples were heated to 200 K. $t = 0$ refers to the time when a constant sample temperature of 200 K was reached.

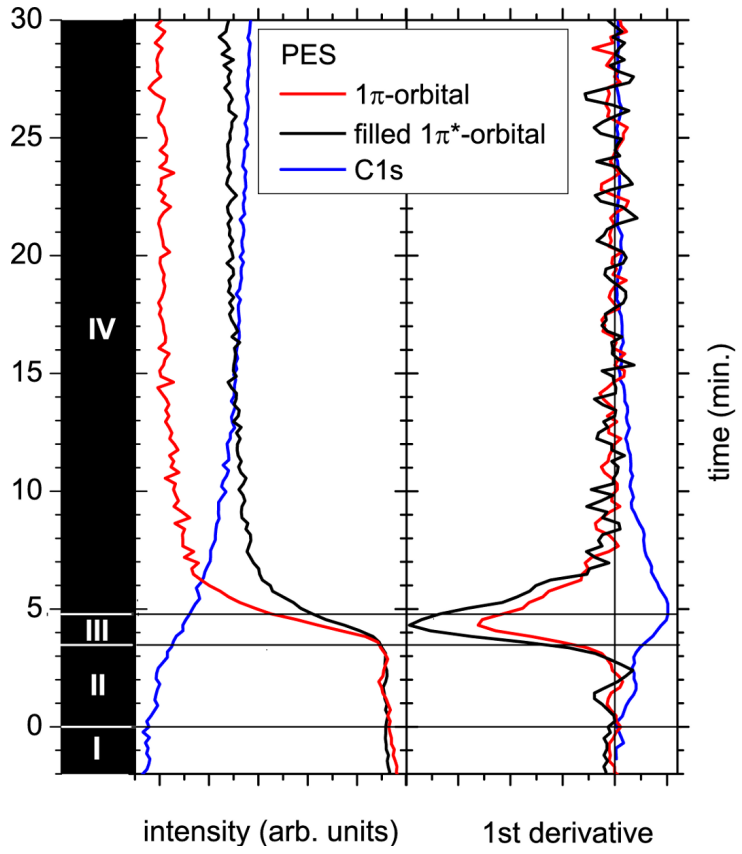

Figure 5.19: Intensity evolution of the C 1s core level along with the 1π-orbital and the initially unoccupied 1π^*-orbital of the first monolayer. Also the derivatives of the integrated intensity evolutions are shown. For more details see text.

colour coding was changed: red refers to high and blue to low intensity. The VR measurements were performed at an excitation energy of 110 eV. This results in a different information depth but also in a higher cross section which is mandatory for measurements in the VR. For the measurements a 8 ML thick NTCDA film was prepared at a substrate temperature of 95 K and annealed at 200 K. The annealing temperature was reached at t=0. I obtained the spectra presented in Fig. 5.18 a) by integrating for 0.5 min at the times indicated by the horizontal dashed lines in b).

At t = -1 min the VR-spectra correspond well to the multilayer spectra published in the literature [155]. I could identify the highest occupied molecular orbital, i.e. the 1π-orbital, at a binding energy of 4.5 eV and which agrees with Reference [155]. There are also molecular orbitals between 4.5 eV and 7 eV binding

energy but since they overlap each other or are partly hidden by substrate bands after roughening of the film a determination of the peak position is more challenging. In section II, at about 1 min of annealing the sample at 200 K, all orbitals shift towards lower binding energy. In Fig. 5.18 a) the energy shift of the 1π-orbital of about 0.6 eV is indicated with black vertical lines. In section III, starting at $t = 4$ min, additional peaks at 2.6 eV and at 0.5 eV were detected. It is well known that these peaks correspond to signals of the 1π- and filled $1\pi^*$-orbital of the first monolayer. Due to the interaction with the substrate the 1π-orbital shifts to lower binding energy and the initially unoccupied $1\pi^*$-orbital is partially filled and appears below the Fermi level [187].

I also investigated the intensity evolution of the peaks at 2.6 eV and 0.5 eV binding energy. In Fig. 5.19, the integrated intensity between 2.22 eV and 2.95 eV as well as 0.7 eV and 0 eV binding energy is plotted along with the previously shown integrated intensity evolution of the C 1s. The intensity of both π-orbitals increases in sections III and IV with the most distinct change in section III and in the beginning of section IV, which can also be seen in the corresponding slopes shown in Fig. 5.19.

Post-annealing study

As discussed in the previous section, I found additional peaks in the valence regime after annealing the film. In Fig. 5.20, I present the region between 3.5 eV and -0.5 eV binding energy for a close-up view of these two peaks. Prior to the measurements the 8 ML thick film was annealed at 200 K for 30 min. After annealing the film was cooled down to 95 K again. For a better illustration of the spectral changes, the intensity was integrated in map b) over 0.5 min at the indicated positions. These profiles of the intensity map are presented in Fig. 5.20 a).

The measurements in Fig. 5.20 started at $T = 95$ K and $t = -6$ min. Starting at $t = -1$ min, the films were annealed at 200 K. A stable temperature was reached at $t = 0$. Between $t = 0$ and $t = 15$ min the temperature was constant at 200 K.

Already at $t = -6$ min peaks at 2.7 eV and 0.5 eV can be recognized. Right after $t = 0$ the shape and intensity of the peak at 0.5 eV binding energy changes. Starting at $t = 1$ min and lasting for about 1 min, the intensity of the peak at 0.5 eV slightly increases and drops very fast afterward. Also the intensity of the peak at 2.7 eV drops at t=2 min. Between t=1 min and t=2 min, the intensity

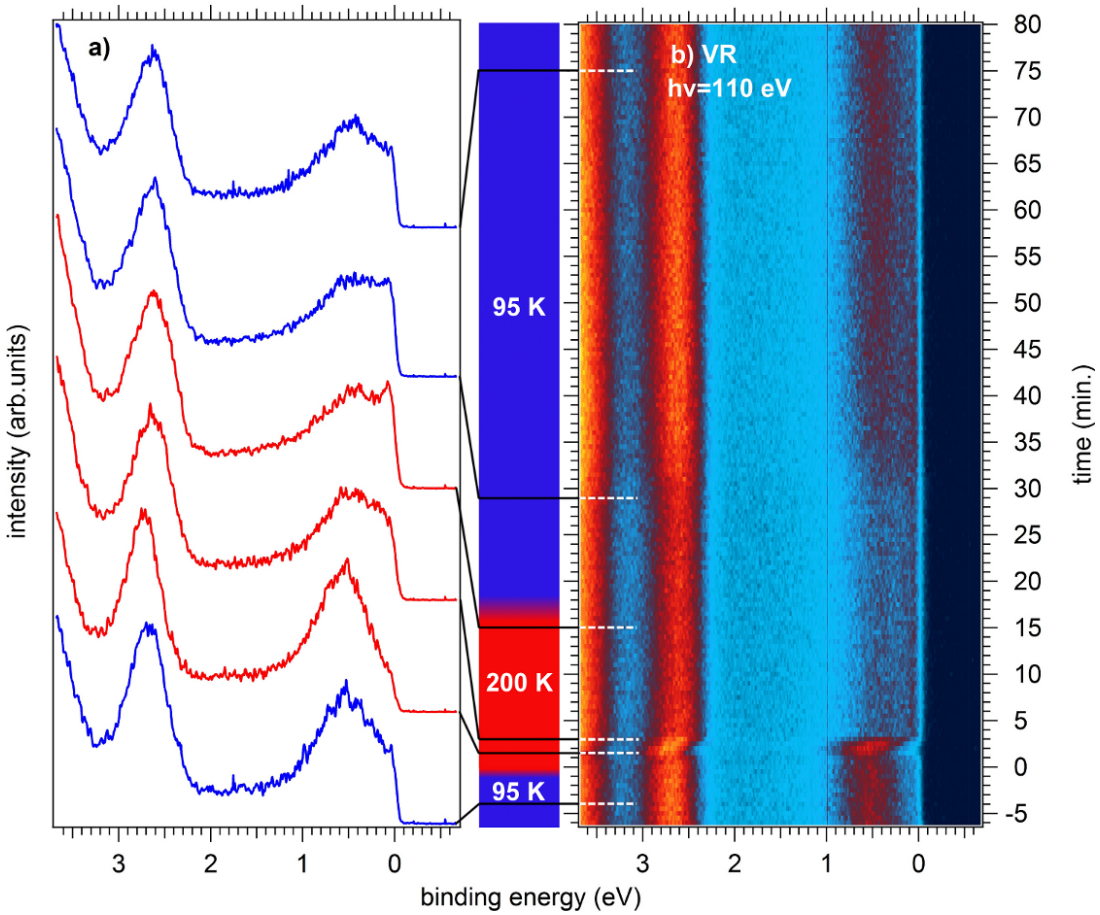

Figure 5.20: Time-dependent photoemission spectra of the valence region (VR) of an NTCDA multilayer film. a) Integrated photoemission intensity (integration time 0.5 min) derived from the data shown in b) at the positions indicated by dashed lines. Blue and red spectra refer to measurements at 95 K and 200 K, respectively. b) 2D colour-coded map of the photoemission spectra. The 8 ML thick film was prepared at 95 K. The measurements were performed immediately after a post-annealing at 200 K for t=30 min. Yellow refers to high and blue to low intensity. See text for more details.

changes are accompanied by small shifts of both peaks of about 100 meV towards higher binding energy. At t = 2 min after annealing, a sharp peak right at the Fermi-edge emerges. When the re-cooling of the sample down to 95 K starts at t =15 min, this sharp feature slowly disappears. Starting at t = 29 min, the intensity of the peak at 0.5 eV steadily increases.

5.3.3 Interpretation and discussion

Phase dynamics

The combination of the NEXAFS and PES results in Fig. 5.15 allows a very detailed insight into the processes that occur upon annealing of the NTCDA films. As known from various spectroscopic [19, 147, 155, 163, 188] and electron diffraction [189] investigations, the NTCDA multilayer films are lacking long-range order after deposition at 95 K and, thus, can be considered amorphous. Moreover, the NTCDA molecules are preferentially lying flat on the substrate surface [19, 147] and the films are morphologically smooth, which leads to the pronounced dichroism in the NEXAFS data with a higher intensity of the *p*-polarized signal and to the absence of any signal from the substrate interface in the PES data shown in Fig. 5.15 (section I). It is also known from the literature annealing at temperatures above 160 K eventually leads to films with crystalline islands [156], which corresponds to section IV of the time-dependent analysis. In this condition of the film the molecules are oriented preferentially upright with respect to the substrate surface [147] which is reflected by the inverted NEXAFS dichroism exhibiting a higher intensity in *s*-polarization now. Moreover, the increased crystallinity involves a morphological roughening of the films. Due to the limited probing depth of the PES and Auger electrons involved in the experiments this leads to the decrease of the PES signal of the NTCDA multilayers observed in Fig. 5.15 d) and also to the collective decrease of the NEXAFS signals in *s*- and *p*-polarization, as visible in Fig. 5.6 c). Furthermore, the roughening accounts for the appearance of the C 1s signal of the first NTCDA layer which is strongly bound to the Ag(111) substrate and is thus observed between $t = 10$ min and $t = 25$ min at lower binding energy (see slanted dashed line in Fig. 5.15 d)) in the PES measurements [188].

The formation of the three-dimensional islands with a crystalline arrangement of the NTCDA molecules involves at least three sub-processes which can be identified by the time evolution analysis I have used. If the substrate temperature is increased after preparation the NTCDA molecules react at first by a change of orientation from flat-lying to upright. This is evident by the inversion of the NEXAFS dichroism in section II. Note that the absolute values of the first derivatives of the *s*- and *p*-polarisation signals are similar, as shown by the corresponding curves in Fig. 5.15 c). At the same time the PES intensity is only very slowly decreasing, indicating only minor roughening of the films.

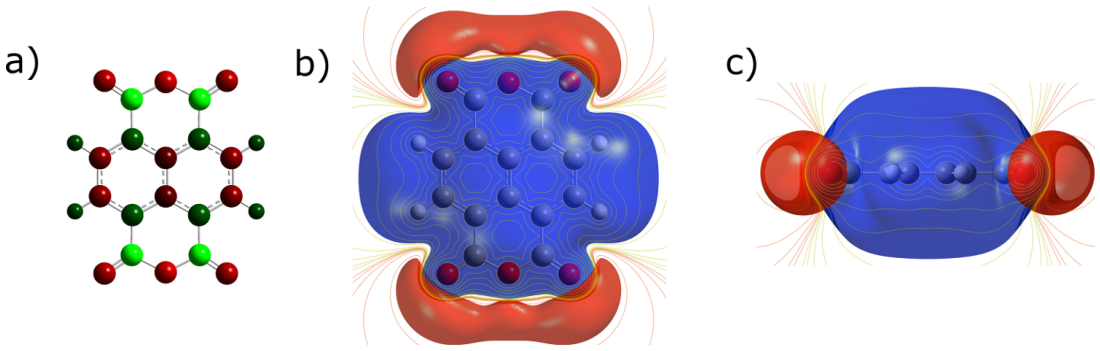

Figure 5.21: a) Mulliken charge distribution of an isolated NTCDA molecule. Red refers to negative and green to positives values. b) and c) Electrostatic potential (ESP) for NTCDA obtained by DFT calculations (b) top view, c) side view). Red refers to low-potential and blue to high-potential regions.

Moreover, the change in orientation angle is also reflected by the energy shifts of the C 1s, O 1s, and valence states. Since the work function is constant at 4.95±0.05 eV throughout the experiment (Fig. 5.17 b)), the energy shift entails a shift of the core and valence levels with respect to the vacuum level. Such an effect has been observed before for similar systems and it can be explained by the intramolecular charge distribution [190]. Duhm et al proposed that the excited photoelectron is affected by the electrostatic potential around the molecule. Therefore, the binding energy of the core and valence levels can also depend on the molecular orientation with respect to the substrate surface. Indeed, for organic compounds with a very anisotropic charge distribution significance of this effect was demonstrated [191–193].
In the framework of this work I can only perform simple DFT calculations for a single NTCDA molecule. The Mulliken charge distribution and electrostatic potential of NTCDA are presented in Fig. 5.21. In a) is shown that the oxygen atoms are slightly more negative than the carbon atom of the naphthalene core. The electrostatic potential (ESP) is shown in b) and c). Around the naphthalene core the energy potential is higher (blue) than around the oxygen atoms (red). Consequently, for a NTCDA film of flat-lying molecules the binding energy of the valence and core levels is slightly higher than for a film with upright-standing NTCDA molecules. From the results and the calculated ESP thus follows, that the molecules are arranged as illustrated in Fig. 5.21 b). Only in such a configuration the ESP is lower above the film.
As soon as the annealing starts in section II, the curves of the integrated NEXAFS intensity patterns shown in Fig. 5.15 c) show a different evolution. While the signal in *s*-polarization is increasing even more strongly, the decrease in *p*-polarization

is slowed down. At the same time the PES intensity starts to decrease, indicating the beginning roughening of the NTCDA film. This is accompanied by a significant alteration of the spectroscopic signature of NEXAFS feature B. In the previous chapter, this change in line shape was associated with a strong coupling of the NTCDA molecules in a transient phase [83]. According to these findings the molecules arrange in an upright configuration and with their molecular planes parallel in a confined time window of several minutes after annealing. Moreover, thickness-dependent experiments showed that this effect can be most clearly observed for films of less than 4 ML thickness.

Fig. 5.22 demonstrates this transient phase in a 5 ML NTCDA film in a time-dependent energy-dispersive NEXAFS experiment with procedure analogous to that of the experiments presented in Fig. 5.15. The colour-coded plot in Fig. 5.22 b) shows the time-evolution data set. In Fig. 5.22 a) several single NEXAFS spectra are compared which have been deduced at the times indicated by the dashed horizontal lines. After the sample has been at 230 K for about 4 min, the signature of feature B changes. Three relatively sharp signals arise which are indicated by the black arrows in Fig. 5.22 a). These sharp signals shift towards lower energy with time, which is illustrated by the slanted dashed lines in Fig. 5.22 b). As elaborated in detail in the previous section and in Ref. [83], the strong coupling of the NTCDA molecules leads to a marked change in the vibronic profiles, enhancing the intensity of the adiabatic components. Also the redshift can be associated to this intermolecular coupling [83].

Comparing the time evolution of the intensity of feature B deduced from the experiment on the 5 ML thick NTCDA film as shown in Fig. 5.22 c) with the corresponding curves for the 8 ML samples as shown in Fig. 5.15 c), the similarities are striking. Of particular importance for the interpretation is the sharp intensity maximum in both data sets. This peak is a strong indication for the existence of the transient phase also in samples with larger coverage.

I therefore suppose that the transient phase develops in the interface region, affecting about three layers on top of the strongly bound, flat-lying first layer [188]. This also occurs for thicker films, where the topmost layers behave differently and do not show the spectroscopic signature of a strongly coupled transient phase. Consequently, in sections III and IV the NEXAFS data of films thicker than 4 ML are a superposition of the transient phase and the topmost layers which are upright-standing and already re-arranging into crystalline islands.

In section IV, the concerted decrease of the intensities of the s- and p-polarization

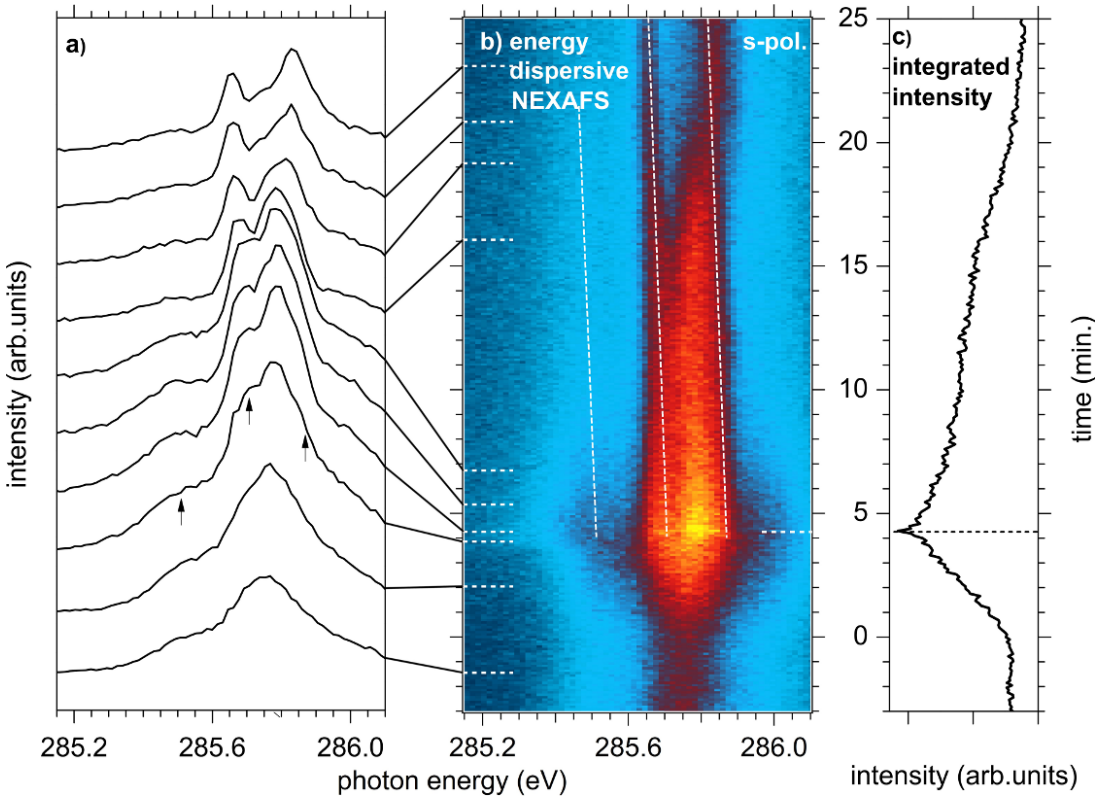

Figure 5.22: Time-dependent NEXAFS study of a 5 ML thick NTCDA film on Ag(111) prepared at 95 K, after annealing at 230 K. a) C K-NEXAFS spectra of feature B deduced from the data shown in b) at the times specified by dashed lines (integration time 0.5 min). b) Colour-coded plot of the energy-dispersive C K-NEXAFS data of feature B recorded with s-polarisation of the incident light. Yellow represents high and blue low intensity. The data acquisition was started after sample preparation at 95 K at $t = -4$ min. The sample was heated quickly and at $t = 0$ a stable temperature of 230 K was established. The doted slanted dashed lines indicate the energy shift of the peaks indicated by black arrows in a) which are discussed in detail in the text. c) Integrated intensity of NEXAFS feature B derived from the data shown in b).

NEXAFS and the C 1s multilayer signals straightforwardly reveal that this regime is governed by a change in film morphology. Very obviously the organisation of the molecules into three-dimensional islands is the dominating process, thus leading to an increasing roughening of the sample until a thermodynamically stable configuration is reached after about 25 min.

This picture of the post-growth annealing behavior of the NTCDA films which I have drawn from the time-evolution analysis is illustrated graphically by the sketches on the right-hand side of Fig. 5.23 together with the derivatives of the NEXAFS intensities from Fig. 5.15 c). On the whole, three sub-processes occur. At first, the molecules change their orientation and flip into a more upright orientation. Next, the NTCDA dyes aggregate into a transition phase featuring strongly coupled molecules with their molecular planes oriented parallel to each other [83]. Finally, three-dimensional islands are formed exhibiting a crystalline structure and accompanied by a marked roughening of the originally smooth films.

Kolmogorov-Johnson-Mehl-Avrami model

The same time-dependent NEXAFS experiments were performed for several similar NTCDA samples after annealing at temperatures between 180 K and 230 K. The evolution of the NEXAFS signal with time is always similar and shows the same general characteristics, as shown in Fig. 5.15 c) and described in detail above. However, the slope of the intensity patterns in each section shows a dependence on the temperature.

For a quantitative analysis of the relevant sub-processes, I evaluated the intensity evolution in each section. If I assume an instant change of the molecular orientation, the NEXAFS signal is proportional to the absolute number of molecules during each phase transformation. The observed characteristic intensity evolution can best be explained with the Kolmogorov-Johnson-Mehl-Avrami model. This model has proven to describe quite successfully the general kinetics in crystallization of amorphous materials, polymers, metals and metal alloys and was introduced in Chapter 2.2.2 [89–92]. The phase transformation kinetics generally follow an s-curve, i.e. a sigmoidal type of function, from which kinetic parameters can be quantified.

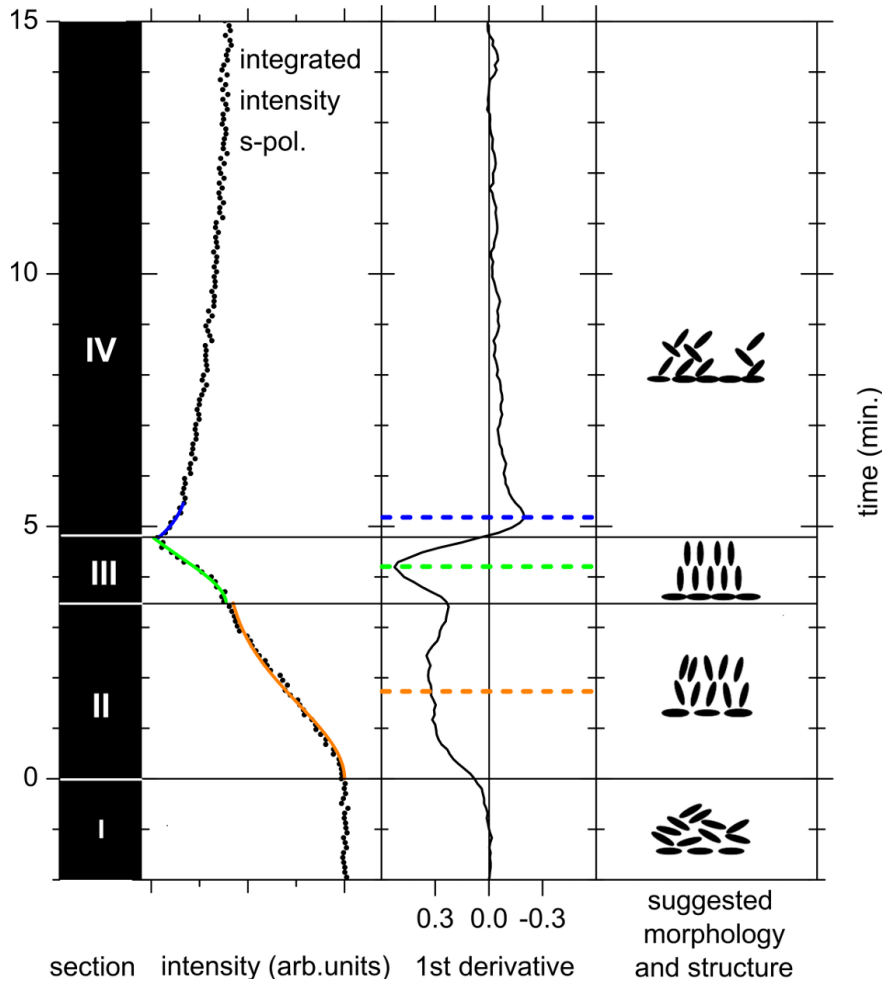

Figure 5.23: Illustration of the sub-processes involved in the post-growth structure formation of NTCDA films: Intensity evolution of the integrated NEXAFS signal along with sigmoidal fits (orange, green and blue traces) in section II, III and IV. Additionally the derivatives of the intensities of the NEXAFS and PES signals shown in Fig. 5.6 c) (left-hand side) together with sketches illustrating the film structure and morphology in sections I-IV are shown. The orange, green and blue dashed horizontal lines mark the maximum slope, at which 50% of the molecules are transformed in each phase transition. The respective values of the first derivative were used for the quantitative analysis of the activation energies. See text for more details.

For isothermal conditions and time-independent nucleation and growth rates, the transformed fraction x is given by

$$x(t) = 1 - e^{-(kt)^n}, \tag{5.15}$$

where k is the temperature-dependent reaction rate constant, t the time, and n the so-called Avrami's exponent. In most situations it can be assumed that the rate constant k shows an Arrhenian temperature dependency,

$$k = k_0 \cdot e^{-\left(\frac{E_{act}}{k_B T}\right)}, \tag{5.16}$$

where k_0 is the frequency factor, E_{act} the activation energy, and k_B Boltzmann's constant. Defining $n(1-x)(-ln(1-x))^{\frac{n^2-1}{n}} = f(x)$, Equation (5.15) can be differentiated with respect to time to yield

$$ln\left(\frac{dx}{dt}\right) = ln(k_0 f(x)) - \frac{E_{act}}{k_B T}, \tag{5.17}$$

with $ln\left(\frac{dx}{dt}\right)$ depending linearly on the inverse of the absolute temperature, $\frac{1}{T}$. By plotting $ln\left(\frac{dx}{dt}\right)$ versus $\frac{1}{T}$ and assuming the frequency factor k_0 and Avrami's exponent n to be constant within each section, the activation energy for the kinetic processes can be extracted from the slope of the corresponding curves.

For a quantitative analysis of the extrema of the slope, I fitted each section II-IV with sigmoidal types of functions. I added a constant intensity offset to the fit function in III and IV which was determined by the initial intensity in the respective sections. In section IV I fitted an inverted s-curve to the intensity evolution in a way that the extrema of the fit coincide with the minimum of the first derivative of the integrated NEXAFS signal. In Fig. 5.23, the fit functions for section II-IV are shown for the measurement at 200 K (orange, green and blue curves). In the following, I will evaluate the extrema of the slopes of the sigmoidal functions which mark the time when 50% of the molecules are transformed during each phase transition. This positions are illustrated by the orange, green and blue dashed horizontal lines in Fig. 5.23.

Fig. 5.24 displays a plot of $ln\left(\frac{d(\text{intensity})}{dt}\right)$ versus $\frac{1}{T}$. A linear dependence on the inverse absolute temperature of the values determined from the different sections can be clearly observed. From linear fits the activation energies can be determined according to Equation 5.17. The resulting values are 81±11 meV for the initial flipping, 57±4 meV for changing into the transient phase, and 76±10 meV for the three-dimensional island growth.

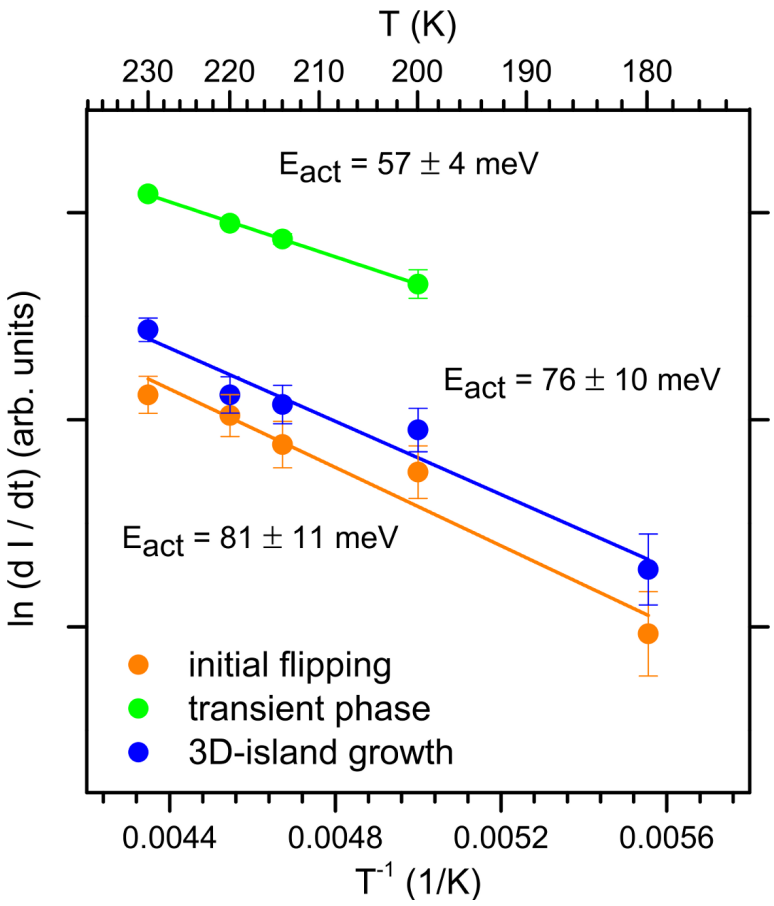

Figure 5.24: Arrhenius plot derived from the analysis of the time-dependent NEXAFS intensities. The values for the three different sub-processes flipping (orange), aggregation in a transient phase (green), and three-dimensional island growth (blue) show a linear behavior, thus allowing the determination of the respective activation energies. Note that at 180 K the transient phase was not observed.

Phase change of the first layer of a multilayer film

Recently, a growing disorder upon cooling was reported for NTCDA monolayer films on Ag(111) [194]. Upon cooling the sample below 155 K, a first-order melting process occurs which was observed with time- and temperature-dependent spot profile analysis low-energy electron diffraction (SPA-LEED) measurements. This so-called "inverse-melting" process was accompanied by changes in the spectral shape and the energy position of the valence levels. Upon annealing, a sharp peak at the Fermi edge emerges which was attributed to a Fermi resonance. The

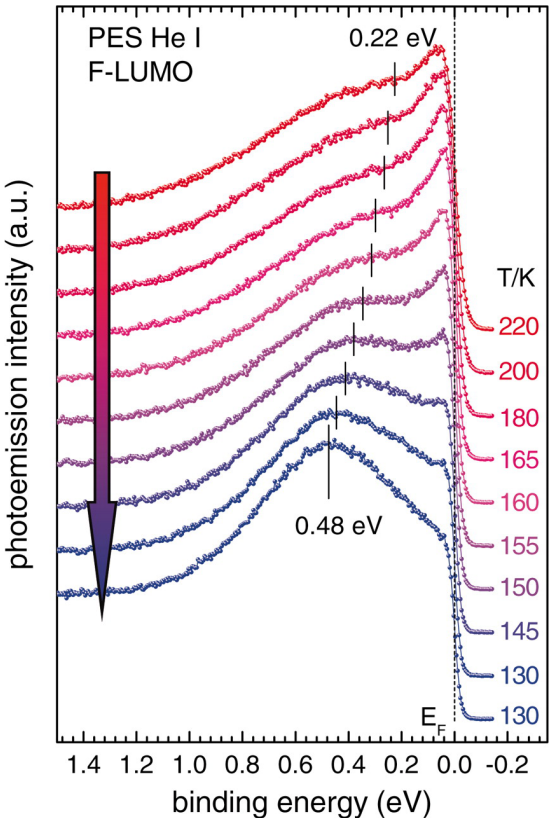

Figure 5.25: Temperature-controlled photoemission study of the valence regime of 1 ML NTCDA on Ag(111). The diagram was taken from Reference [194].

authors interpreted their spectroscopic results by a stronger molecule-substrate interaction at lower temperature. Therefore, the initially unoccupied molecular orbital $1\pi^*$ is pulled below the Fermi edge of the substrate and partially filled. In Fig. 5.25, a typical temperature-controlled photoemission study of 1 ML NTCDA on Ag(111) is shown[1].

The similarity to the time- and temperature-dependent photoemission measurements presented in Fig. 5.20 is a indication of the inverse melting of the first monolayer. After roughening of the multilayer film prior to the measurement, the signal of the first monolayer can clearly be identified. The Fermi resonance in Fig. 5.20 appears after 4 min at 200 K. It has to be stressed that I have no structural information of the first monolayer, which would be desirable for a unambiguous identification of the findings. Gador investigated the first mono-

[1]Note that the $1\pi^*$ orbital is referred to as F-LUMO in Fig. 5.25.

layer of a NTCDA multilayer films with LEED and found a densely packed film structure, which they donated as a "compressed monolayer" [195]. For such a structure, Schöll also found the inverse melting [196].

5.3.4 Conclusion

In this section, I studied the structure formation of NTCDA multilayer films on Ag(111) and demonstrated the capability of energy-dispersive NEXAFS in real-time measurements. A particular advantage of this method is the simultaneous access to information on structural aspects and on the electronic properties of the film with a time resolution of seconds. Moreover, it allows studying the geometry and stability of transient phases which can be of crucial importance for the comprehensive understanding of nucleation and film growth phenomena. The importance has been shown for various materials, from metals [197] to small molecules such as e.g. water [198] where the geometric arrangement of the constituents is intricately dependent on the size of the aggregate or cluster.

In chapter 5.3 I report on the first observation of effects in the structure formation within extended aggregates of molecules that are analogous to the aforementioned phenomena reported in the literature. During post-growth annealing of NTCDA multilayer films, I identified different processes that occur prior to the formation of the crystalline structures and I quantified the corresponding activation energies. After an initial flipping of the NTCDA molecules into a more upright orientation, a transient phase is established which is characterised by a particularly strong intermolecular coupling. Finally, on a time scale of several minutes, three-dimensional islands are established with bulk crystalline structure involving substantial mass transport on the substrate surface accompanied by morphological roughening.

6

Summary

Films of π-conjugated molecules are considered to be model systems for the investigation of the electronic properties and especially the intermolecular coupling in organic semiconductors. Moreover, all three fundamental growth modes were observed in films of aromatic molecules, which allows the investigation of the interplay between film morphology, geometric structure and electronic structure. In my thesis, I investigated the role of core hole-electron correlation and intermolecular interaction of NTCDA molecules. Furthermore, I explored in a real-time study the structure formation upon annealing from an initially amorphous film towards a three-dimensional, stable film structure.

In Chapter 5.2, I demonstrated the importance of the core hole-electron correlation in coherently coupled molecules and its influence on NEXAFS spectroscopy. In the course of the temperature-induced transition of an initially amorphous film with preferentially flat-lying molecules to a phase with more upright-orientated molecules, I discovered a transient phase for 4 ML thick NTCDA films on Ag(111). This phase is characterized by a distinct and unique spectral shape change which sets the transient phase clearly apart from the gas phase and condensed phase. The line widths of the most prominent signals are each reduced by about 137 meV and by 100 meV redshifted with respect to the gas-phase measurements. Most interestingly, the vibronic profile is substantially changed. I was able to straightforwardly explain my results by the dipole coupling of neighboring molecules and, therefore, applied models which are well established in optical spectroscopy. By means of these models I was capable of interpreting all my experimental findings. I discovered that the core hole-electron is delocalized over 8 ± 3 molecules. From FCA/cc-pVTZ calculations follows that core-valence transition dipole moments are significantly smaller than valence-valence transitions. From the results of DFT calculations I estimated the contribution of the frontier-orbital wave function overlap for closely packed π-conjugated molecules. At a distance of around 3 Å between two molecules arranged face to face, I found a high electron density which accounts for an additional charge transfer transition dipole moment. From

the redshift of the most prominent signals, I calculated the exciton band structure for dipole-dipole interacting molecules. Furthermore, from the peak width I estimated the energy transfer time to be of the order of $\sim 4 \cdot 10^{-15}$ sec.
My experimental results provide evidence for a delocalized core hole-electron pair in coherently coupled molecules. My findings suggest that the core-to-valence excitations in the X-ray range are substantially larger than estimated for an isolated molecule. I therefore suggest an additional contribution due to the wave function overlap of adjacent molecules.

In Chapter 5.3, I presented the investigation of the formation of a three-dimensional, stable film structure in NTCDA multilayer films measured in real time. I investigated the phase change and the formation of a three-dimensional film structure with long-range order upon annealing of smooth 8–10 ML thick NTCDA films of initially preferentially flat-lying molecules. The intensity evolution of the X-ray absorption signal in s- and p-polarization showed a very characteristic behavior which I divided into four different sections. A similar intensity evolution in four different sections was found in measurements between 180 K and 230 K. By combining this with the results of time-dependent photoemission measurements, I could describe the post-growth behavior of NTCDA multilayer films:

- Section I: amorphous, but preferentially orientated flat on the substrate surface;
- Section II: flipping into an upright orientation;
- Section III: strong intermolecular coupling;
- Section IV: three-dimensional film structure formation and film roughening.

With the Kolmogorov-Johnson-Mehl-Avrami model I determined the activation energies, i.e. 81±11 meV for the flipping, 57±4 meV for the transition into the strongly coupling phase, and 76±10 meV for the three-dimensional island growth. The results of my post-growth study of NTCDA multilayer films demonstrate the importance of time-dependent measurements for the investigation of growth and post-growth phenomena. Prior to the formation of a stable, three-dimensional film structure and film roughening, I detected the occurrence of a transient phase where the molecules are oriented preferentially upright with respect to the substrate surface and which is characterized by a strong intermolecular coupling between neighboring molecules.

A key ingredient of my experimental work was the novel method soft X-ray

energy-dispersive NEXAFS spectroscopy at the end station UE52-PGM of the BESSY II synchrotron light source of the Helmholtz-Zentrum Berlin. A major advantage of this new method is the simultaneous access to spectroscopic and structural information with a temporal resolution of seconds. During my Ph. D thesis, I performed the initial experiments using the novel method and explored its potential with respect to real-time studies, in particular the measurements of organic thin films. For a quantitative evaluation of the raw data set, I developed a correction routine to compensate the non-linear gain of the micro-channel plate. Also the energy calibration required a specific approach.

In this work, I utilized soft X-ray energy-dispersive NEXAFS spectroscopy as a novel method to explore intermolecular coupling, short-lived transient phases and post-growth processes. In a next step, this technique can be applied to more complex systems such as molecular switches [199]. For applications of such switches in, e.g., organic-based transistors, memory devices and logic circuits, it is essential to understand and control the switching between different three-dimensional spatial arrangements of the molecules [200–204]. Time-dependent energy-dispersive NEXAFS measurements facilitate the simultaneous study of the molecular rearrangement and its effects on the electronic properties. Such information is essential for a better understanding of molecular switching mechanisms, which is of key importance for gaining full mastery of organic electronic materials.
Also, the investigation of donor and acceptor materials in layered or blended thin films structures is of special interest. Such films are basic elements of novel passive and active organic electronic devices and they consist of at least two different organic components. They feature a complex film structure which depends on the preparation and post-annealing processes [205–207]. Of particular interest is the evolution of the blended or layered material's surface composition and morphology during annealing since this strongly influences the performance of devices made from such materials [208–210]. Time-dependent energy-dispersive NEXAFS measurements will help to elucidate the influence of the post-annealing process on the surface composition and morphology of organic materials.

List of Figures

List of Tables

List of own publications

[1] D. Kuethe, M. Scholz, and P. Fantazzini. Imaging inert fluorinated gases in cracks: perhaps in david's ankles. *Magnetic Resonance Imaging*, 25(4):505–508, May 2007.

[2] M. Scholz, R. Schmidt, S. Krause, A. Schöll, F. Reinert, and F. Würthner. Electronic structure of epitaxial thin films of bay-substituted perylene bisimide dyes. *Applied Physics A*, 95(1):285–290, April 2009.

[3] C. Arantes, M. Scholz, R. Schmidt, V. Dehm, M. L. M. Rocco, A. Schöll, F. Reinert, and F. Würthner. Comparative analysis of the energy levels of planar and core-twisted perylene bisimides in solution and solid state by UV/VIS, CV, and UPS/IPES. *Applied Physics A*, 108(3):629–637, May 2012.

[4] M. Scholz, F. Holch, C. Sauer, M. Wiessner, A. Schöll, and F. Reinert. Core hole-electron correlation in coherently coupled molecules. *Physical Review Letters*, accepted Tuesday Apr 23, 2013.

[5] M. Scholz, C. Sauer, M. Wiessner, N. Nguyen, A. Schöll, and F. Reinert. Structure formation in organic thin films observed in real time by energy dispersive nexafs. *New Journal of Physics*, submitted.

Bibliography

[1] H. Letheby. XXIX.—On the production of a blue substance by the electrolysis of sulphate of aniline. *Journal of the Chemical Society*, 15(0):161–163, January 1862.

[2] The nobel prize in chemistry 2000, Nobelprize.org. 6 May 2013.

[3] Vikram C. Sundar, Jana Zaumseil, Vitaly Podzorov, Etienne Menard, Robert L. Willett, Takao Someya, Michael E. Gershenson, and John A. Rogers. Elastomeric transistor stamps: Reversible probing of charge transport in organic crystals. *Science*, 303(5664):1644–1646, March 2004. PMID: 15016993.

[4] Hiroyuki Yamane, Satoshi Kera, Koji K. Okudaira, Daisuke Yoshimura, Kazuhiko Seki, and Nobuo Ueno. Intermolecular energy-band dispersion in PTCDA multilayers. *Physical Review B*, 68(3):033102, July 2003.

[5] J. Takeya, M. Yamagishi, Y. Tominari, R. Hirahara, Y. Nakazawa, T. Nishikawa, T. Kawase, T. Shimoda, and S. Ogawa. Very high-mobility organic single-crystal transistors with in-crystal conduction channels. *Applied Physics Letters*, 90(10):102120–102120–3, March 2007.

[6] G. Koller, S. Berkebile, M. Oehzelt, P. Puschnig, C. Ambrosch-Draxl, F. P. Netzer, and M. G. Ramsey. Intra- and intermolecular band dispersion in an organic crystal. *Science*, 317(5836):351–355, July 2007.

[7] Shin-ichi Machida, Yasuo Nakayama, Steffen Duhm, Qian Xin, Akihiro Funakoshi, Naoki Ogawa, Satoshi Kera, Nobuo Ueno, and Hisao Ishii. Highest-occupied-molecular-orbital band dispersion of rubrene single crystals as observed by angle-resolved ultraviolet photoelectron spectroscopy. *Physical Review Letters*, 104(15):156401, April 2010.

[8] H. Sirringhaus, P. J. Brown, R. H. Friend, M. M. Nielsen, K. Bechgaard, B. M. W. Langeveld-Voss, A. J. H. Spiering, R. A. J. Janssen, E. W. Meijer, P. Herwig, and D. M. de Leeuw. Two-dimensional charge transport in self-organized, high-mobility conjugated polymers. *Nature*, 401(6754):685–688, October 1999.

[9] D. M. DeLongchamp, S. Sambasivan, D. A. Fischer, E. K. Lin, P. Chang, A. R. Murphy, J. M. J. Fréchet, and V. Subramanian. Direct correlation of organic semiconductor film structure to field-effect mobility. *Advanced Materials*, 17(19):2340–2344, 2005.

[10] L. Li, Q. Tang, H. Li, X. Yang, W. Hu, Y. Song, Z. Shuai, W. Xu, Y. Liu, and D. Zhu. An ultra closely π-stacked organic semiconductor for high performance field-effect transistors. *Advanced Materials*, 19(18):2613–2617, 2007.

[11] Howard E. Katz and Jia Huang. Thin-film organic electronic devices. *Annual Review of Materials Research*, 39(1):71–92, 2009.

[12] Gregor Witte and Christof Wöll. Growth of aromatic molecules on solid substrates for applications in organic electronics. *Journal of Materials Research*, 19(07):1889–1916, 2004.

[13] S Kowarik, A Gerlach, and F Schreiber. Organic molecular beam deposition: Fundamentals, growth dynamics, and in situ studies. *Journal of Physics: Condensed Matter*, 20(18):184005, May 2008.

[14] F. Schreiber. Organic molecular beam deposition: Growth studies beyond the first monolayer. *physica status solidi (a)*, 201(6):1037–1054, 2004.

[15] Atsushi Koma. Molecular beam epitaxial growth of organic thin films. *Progress in Crystal Growth and Characterization of Materials*, 30(2–3):129–152, 1995.

[16] Stephen R. Forrest. Ultrathin organic films grown by organic molecular beam deposition and related techniques. *Chemical Reviews*, 97(6):1793–1896, October 1997.

[17] Höfer, Breitschafter, and Umbach. Photoemission line shapes of adsorbates: Conclusions from the analysis of vibration-resolved N2 spectra. *Physical Review Letters*, 64(25):3050–3053, June 1990. PMID: 10041882.

[18] A. Föhlisch, N. Wassdahl, J. Hasselström, O. Karis, D. Menzel, N. Mårtensson, and A. Nilsson. Beyond the chemical shift: Vibrationally resolved core-level photoelectron spectra of adsorbed CO. *Physical Review Letters*, 81(8):1730–1733, 1998.

[19] A. Schöll, Y. Zou, L. Kilian, D. Hübner, D. Gador, C. Jung, S. G. Urquhart, Th. Schmidt, R. Fink, and E. Umbach. Electron-vibron coupling in high-resolution X-ray absorption spectra of organic materials: NTCDA on Ag(111). *Physical Review Letters*, 93(14):146406, 2004.

[20] T. Förster. Zwischenmolekulare Energiewanderung und Fluoreszenz. *Annalen Der Physik*, 2(1-2):55–75, 1948. WOS:A1948UY61400004.

[21] J S Briggs and A Herzenberg. Sum rules for the vibronic spectra of helical polymers. *Journal of Physics B: Atomic and Molecular Physics*, 3(12): 1663–1676, December 1970.

[22] J.S. Briggs and A. Herzenberg. Bandshapes in polymer spectra. *Molecular Physics*, 21(5):865–879, 1971.

[23] John A. Venables. *Introduction to Surface and Thin Film Processes*. Cambridge University Press, 2000. ISBN 9780511755651.

[24] S. Kowarik, A. Gerlach, S. Sellner, F. Schreiber, L. Cavalcanti, and O. Konovalov. Real-time observation of structural and orientational transitions during growth of organic thin films. *Physical Review Letters*, 96(12): 125504, March 2006.

[25] F. Schreiber. Organic molecular beam deposition: Growth studies beyond the first monolayer. In Wolfgang Brütting, editor, *Physics of Organic Semiconductors*, page 15–40. Wiley-VCH Verlag GmbH & Co. KGaA, 2006. ISBN 9783527606634.

[26] Gregor Hlawacek, Peter Puschnig, Paul Frank, Adolf Winkler, Claudia Ambrosch-Draxl, and Christian Teichert. Characterization of step-edge barriers in organic thin-film growth. *Science*, 321(5885):108–111, July 2008.

[27] Achim Schöll and Frank Schreiber. *Thin Films of Organic Molecules: Interfaces and Epitaxial Growth*. Elsevier, Oxford, 2013. ISBN 978-0-12-387839-7. 591–609 pp.

[28] L. Kilian, A. Hauschild, R. Temirov, S. Soubatch, A. Schöll, A. Bendounan, F. Reinert, T.-L. Lee, F. S. Tautz, M. Sokolowski, and E. Umbach. Role of intermolecular interactions on the electronic and geometric structure of a large π-conjugated molecule adsorbed on a metal surface. *Physical Review Letters*, 100(13):136103, April 2008.

[29] David Cahen, Antoine Kahn, and Eberhard Umbach. Energetics of molecular interfaces. *Materials Today*, 8(7):32–41, July 2005.

[30] Christoph Stadler, Sören Hansen, Ingo Kröger, Christian Kumpf, and Eberhard Umbach. Tuning intermolecular interaction in long-range-ordered submonolayer organic films. *Nature Physics*, 5(2):153–158, 2009.

[31] Ingo Kröger, Benjamin Stadtmüller, Christian Wagner, Christian Weiss, Ruslan Temirov, F. Stefan Tautz, and Christian Kumpf. Modeling intermolecular interactions of physisorbed organic molecules using pair potential calculations. *The Journal of Chemical Physics*, 135(23):234703–234703–12, December 2011.

[32] C. Arantes, M. Scholz, R. Schmidt, V. Dehm, M. L. M. Rocco, A. Schöll, F. Reinert, and F. Würthner. Comparative analysis of the energy levels of planar and core-twisted perylene bisimides in solution and solid state by UV/VIS, CV, and UPS/IPES. *Applied Physics A*, 108(3):629–637, May 2012.

[33] David Parker Craig and D. P. Craig T. Thirunamachandran. *Molecular Quantum Electrodynamics: An Introduction to Radiation-Molecule Interactions*. Courier Dover Publications, 1984. ISBN 9780486402147.

[34] Gregory D. Scholes and Kenneth P. Ghiggino. Electronic interactions and interchromophore excitation transfer. *The Journal of Physical Chemistry*, 98(17):4580–4590, April 1994.

[35] Gregory D. Scholes and Kenneth P. Ghiggino. Mechanisms of excitation transfer in multichromophoric systems. *Journal of Photochemistry and Photobiology A: Chemistry*, 80(1–3):355–362, May 1994.

[36] J. Roden, A. Eisfeld, and J.S. Briggs. The j- and h-bands of dye aggregate spectra: Analysis of the coherent exciton scattering (CES) approximation. *Chemical Physics*, 352(1–3):258–266, September 2008.

[37] Volkhard May and Oliver Kühn. *Charge and Energy Transfer Dynamics in Molecular Systems*. John Wiley & Sons, November 2008. ISBN 9783527617470.

[38] Y. Ma, F. Sette, G. Meigs, S. Modesti, and C. T. Chen. Breaking of ground-state symmetry in core-excited ethylene and benzene. *Physical Review Letters*, 63(19):2044–2047, November 1989.

[39] G. Remmers, M. Domke, and G. Kaindl. Vibrationally resolved carbon core excitations in alkane molecules. *Physical Review A*, 47(4):3085–3091, April 1993.

[40] Jan Roden, Alexander Eisfeld, Matthieu Dvořák, Oliver Bünermann, and Frank Stienkemeier. Vibronic line shapes of PTCDA oligomers in helium nanodroplets. *The Journal of Chemical Physics*, 134(5):054907–054907–12, February 2011.

[41] Alexander Eisfeld, Georg Schulz, and John Briggs. The influence of geometry on the vibronic spectra of quantum aggregates. *Journal of Luminescence*, 131(12):2555–2564, December 2011.

[42] John S. Briggs and Alexander Eisfeld. Equivalence of quantum and classical coherence in electronic energy transfer. *Physical Review E*, 83(5):051911, May 2011.

[43] Hitoshi Sumi. Exciton-phonon interaction in the coherent potential approximation with application to optical spectra. *Journal of the Physical Society of Japan*, 32(3):616–628, 1972.

[44] Paul Soven. Coherent-potential model of substitutional disordered alloys. *Physical Review*, 156(3):809–813, April 1967.

[45] B. Velický, S. Kirkpatrick, and H. Ehrenreich. Single-site approximations in the electronic theory of simple binary alloys. *Physical Review*, 175(3): 747–766, November 1968.

[46] B. Velický. Theory of electronic transport in disordered binary alloys: Coherent-potential approximation. *Physical Review*, 184(3):614–627, August 1969.

[47] A. Eisfeld and J.S. Briggs. The J- and H-bands of organic dye aggregates. *Chemical Physics*, 324(2–3):376–384, May 2006.

[48] Alexander Eisfeld and John S Briggs. The J-band of organic dyes: Lineshape and coherence length. *Chemical Physics*, 281(1):61–70, July 2002.

[49] E. W. Knapp. Vibrational line shapes in liquids. the role of resonant intermolecular coupling. *The Journal of Chemical Physics*, 81(2):643–652, July 1984.

[50] P. B Walczak, A. Eisfeld, and J. S Briggs. Exchange narrowing of the J band of molecular dye aggregates. *The Journal of Chemical Physics*, 128 (4):044505–044505–12, January 2008.

[51] Jan Roden and Alexander Eisfeld. Anomalous strong exchange narrowing in excitonic systems. *The Journal of Chemical Physics*, 134(3):034901–034901–8, January 2011.

[52] Uli Wurfel, Michael Thorwart, and Eicke R. Weber. *Quantum Efficiency in Complex Systems, Part II: From Molecular Aggregates to Organic Solar Cells: Organic Solar Cells*. Academic Press, I edition, November 2011.

[53] H.A. Kramers. La diffusion de la lumière par les atomes. *Atti Cong. Intern. Fisica, (Transactions of Volta Centenary Congress)*, 2:545–557, 1927.

[54] R. De L. Kronig. On the theory of dispersion of X-rays. *Journal of the Optical Society of America*, 12(6):547–556, June 1926.

[55] V. Stehr, J. Pfister, R. F. Fink, B. Engels, and C. Deibel. First-principles calculations of anisotropic charge-carrier mobilities in organic semiconductor crystals. *Physical Review B*, 83(15):155208, April 2011.

[56] Volker Settels, Wenlan Liu, Jens Pflaum, Reinhold F. Fink, and Bernd Engels. Comparison of the electronic structure of different perylene-based dye-aggregates. *Journal of Computational Chemistry*, 33(18):1544–1553, 2012.

[57] Satoshi Kera, Hiroyuki Yamane, Isamu Sakuragi, Koji K. Okudaira, and Nobuo Ueno. Very narrow photoemission bandwidth of the highest occupied state in a copper-phthalocyanine monolayer. *Chemical Physics Letters*, 364(1–2):93–98, September 2002.

[58] N. Koch, A. Vollmer, I. Salzmann, B. Nickel, H. Weiss, and J. P. Rabe. Evidence for temperature-dependent electron band dispersion in pentacene. *Physical Review Letters*, 96(15):156803, April 2006.

[59] Nobuo Ueno and Satoshi Kera. Electron spectroscopy of functional organic thin films: Deep insights into valence electronic structure in relation to charge transport property. *Progress in Surface Science*, 83(10–12):490–557, December 2008.

[60] H. Yamagata, J. Norton, E. Hontz, Y. Olivier, D. Beljonne, J. L. Brédas, R. J. Silbey, and F. C. Spano. The nature of singlet excitons in oligoacene molecular crystals. *The Journal of Chemical Physics*, 134(20):204703–204703–11, May 2011.

[61] Hajime Yamagata, Chris M. Pochas, and Frank C. Spano. Designing J- and H-aggregates through wave function overlap engineering: Applications to poly(3-hexylthiophene). *The Journal of Physical Chemistry B*, 116(49): 14494–14503, December 2012.

[62] Richard D. Harcourt, Gregory D. Scholes, and Kenneth P. Ghiggino. Rate expressions for excitation transfer. II. electronic considerations of direct and through–configuration exciton resonance interactions. *The Journal of Chemical Physics*, 101(12):10521–10525, December 1994.

[63] R. S. Mulliken. Electronic population analysis on LCAOXMO molecular wave functions. *The Journal of Chemical Physics*, 23(10):1833–1840, October 1955.

[64] J. N. Murrell, M. Randic, and D. R. Williams. The theory of intermolecular forces in the region of small orbital overlap. *Proceedings of the Royal Society of London. Series A. Mathematical and Physical Sciences*, 284(1399):566–581, March 1965.

[65] Jian Ping Lu, X.-P. Li, and Richard M. Martin. Ground state and phase transitions in solid C60. *Physical Review Letters*, 68(10):1551–1554, March 1992.

[66] Jean-Luc Brédas, David Beljonne, Veaceslav Coropceanu, and Jérôme Cornil. Charge-transfer and energy-transfer processes in π-conjugated oligomers and polymers: A molecular picture. *Chemical Reviews*, 104(11): 4971–5004, November 2004.

[67] Jean-Luc Brédas, Joseph E. Norton, Jérôme Cornil, and Veaceslav Coropceanu. Molecular understanding of organic solar cells: The challenges. *Accounts of Chemical Research*, 42(11):1691–1699, November 2009.

[68] M. Hoffmann, K. Schmidt, T. Fritz, T. Hasche, V.M. Agranovich, and K. Leo. The lowest energy frenkel and charge-transfer excitons in quasi-one-dimensional structures: application to MePTCDI and PTCDA crystals. *Chemical Physics*, 258(1):73–96, August 2000.

[69] M. Hoffmann and Z. G. Soos. Optical absorption spectra of the holstein molecular crystal for weak and intermediate electronic coupling. *Physical Review B*, 66(2):024305, July 2002.

[70] I. J. Lalov, C. Warns, and P. Reineker. Model of mixed frenkel and charge-transfer excitons in donor acceptor molecular crystals: Investigation of vibronic spectra. *New Journal of Physics*, 10(8):085006, August 2008.

[71] Grzegorz Mazur, Piotr Petelenz, and Michał Slawik. Transition dipole moments of charge transfer excitations in one-component molecular crystals. *Chemical Physics*, 397:92–97, March 2012.

[72] Robert S. Mulliken. Molecular compounds and their spectra. II. *Journal of the American Chemical Society*, 74(3):811–824, February 1952.

[73] Robert Sanderson Mulliken and Willis B. Person. *Molecular complexes: A lecture and reprint volume*. Wiley-Interscience, 1969.

[74] Vladimir Agranovich. *Excitations in Organic Solids*. Oxford University Press, February 2009. ISBN 9780199234417.

[75] R.F. Fink, J. Pfister, A. Schneider, H. Zhao, and B. Engels. Ab initio configuration interaction description of excitation energy transfer between closely packed molecules. *Chemical Physics*, 343(2–3):353–361, January 2008.

[76] Anna Stradomska, Waldemar Kulig, Michał Slawik, and Piotr Petelenz. Intermediate vibronic coupling in charge transfer states: Comprehensive calculation of electronic excitations in sexithiophene crystal. *The Journal of Chemical Physics*, 134(22):224505–224505–12, June 2011.

[77] Wenlan Liu, Volker Settels, Philipp H. P. Harbach, Andreas Dreuw, Reinhold F. Fink, and Bernd Engels. Assessment of TD-DFT- and TD-HF-based approaches for the prediction of exciton coupling parameters, potential energy curves, and electronic characters of electronically excited aggregates. *Journal of Computational Chemistry*, 32(9):1971–1981, 2011.

[78] Kazuhiro J. Fujimoto. Transition-density-fragment interaction combined with transfer integral approach for excitation-energy transfer via charge-transfer states. *The Journal of Chemical Physics*, 137(3):034101–034101–9, July 2012.

[79] Conor Hogan, Maurizia Palummo, Johannes Gierschner, and Angel Rubio. Correlation effects in the optical spectra of porphyrin oligomer chains: Exciton confinement and length dependence. *The Journal of Chemical Physics*, 138(2):024312–024312–12, January 2013.

[80] David Fyfe. LED technology: Organic displays come of age. *Nature Photonics*, 3(8):453–455, August 2009.

[81] Michael F. L. De Volder, Sameh H. Tawfick, Ray H. Baughman, and A. John Hart. Carbon nanotubes: Present and future commercial applications. *Science*, 339(6119):535–539, February 2013.

[82] H. Marchetto, U. Groh, Th. Schmidt, R. Fink, H.-J. Freund, and E. Umbach. Influence of substrate morphology on organic layer growth: PTCDA on Ag(111). *Chemical Physics*, 325(1):178–184, June 2006.

[83] M. Scholz, F. Holch, C. Sauer, M. Wiessner, A. Schöll, and F. Reinert. Core hole-electron correlation in coherently coupled molecules. *Physical Review Letters*, accepted Tuesday Apr 23, 2013.

[84] Ernst Bauer. Phänomenologische Theorie der Kristallabscheidung an Oberflächen. *Zeitschrift fur Kristallographie*, 110:372–394, January 1958.

[85] John A Venables. Atomic processes in crystal growth. *Surface Science*, 299–300(0):798–817, January 1994.

[86] C. E. Aumann, R. Kariotis, and M. G. Lagally. Rate equation modeling of interface width. *Journal of Vacuum Science & Technology A: Vacuum, Surfaces, and Films*, 7(3):2180–2185, 1989.

[87] Alex C. Mayer, Ricardo Ruiz, Hua Zhou, Randall L. Headrick, Alexander Kazimirov, and George G. Malliaras. Growth dynamics of pentacene thin films: Real-time synchrotron X-ray scattering study. *Physical Review B*, 73 (20):205307, May 2006.

[88] M. Fendrich and J. Krug. Ehrlich-schwoebel effect for organic molecules: Direct calculation of the step-edge barrier using empirical potentials. *Physical Review B*, 76(12):121302, September 2007.

[89] W.A. Johnson and R.F. Mehl. Reaction kinetics in processes of nucleation and growth. *Trans. Am. Inst. Min., Metall. Pet. Eng.*, 135(416), 1939.

[90] Melvin Avrami. Kinetics of phase change. i general theory. *The Journal of Chemical Physics*, 7(12):1103–1112, December 1939.

[91] Melvin Avrami. Kinetics of phase change. II Transformation-Time relations for random distribution of nuclei. *The Journal of Chemical Physics*, 8(2): 212–224, February 1940.

[92] Melvin Avrami. Granulation, phase change, and microstructure kinetics of phase change. III. *The Journal of Chemical Physics*, 9(2):177–184, February 1941.

[93] M. E. Fine. *Phase Transformations in Condensed Systems*. The Macmillan Co, 1964.

[94] C. N. R. Rao and K. J. Rao. *Phase Transitions in Solids: An Approach to the Study of Chemistry and the Physics of Solids*. McGraw-Hill Inc.,US, June 1978. ISBN 0070511853.

[95] Sergei V. Nemilov. *Vitreous State Thermodynamic & Kinetic Aspects*. CRC Press Inc, March 1995. ISBN 0849337828.

[96] Werner Pepperhoff and Mehmet Acet. *Constitution and Magnetism of Iron and its Alloys*. Springer, I edition, November 2001.

[97] J. W. Christian. *The Theory of Transformations in Metals and Alloys (Part I+II)*. Pergamon, 1 edition, December 2002. ISBN 0080440193.

[98] G Hampel, A Pundt, and J Hesse. Crystallization of Fe73.5Cu1Nb3Si13.5B9 structure and kinetics examined by X-ray diffraction and mossbauer effect spectroscopy. *Journal of Physics: Condensed Matter*, 4(12):3195–3214, March 1992.

[99] Fei Zhou, Kai-Yuan He, Man-Ling Sui, and Zu-Han Lai. Nucleation and growth characteristics of amorphous FeSiB(Cu)(Nb) alloys during isothermal crystallization process. *Materials Science and Engineering: A*, 181–182 (0):1419–1422, May 1994.

[100] A. Cserei, J. Jiang, F. Aubertin, and U. Gonser. Study of the crystallization kinetics in amorphous Fe73.5Cu1Nb3Si13.5B9 alloy. *Journal of Materials Science*, 29(5):1213–1216, March 1994.

[101] A. Danzig, N. Mattern, and S. Doyle. An in-situ investigation of the Fe3Si crystallization in amorphous Fe73.5Si15.5B7Cu1Nb3. *Nuclear Instruments and Methods in Physics Research Section B: Beam Interactions with Materials and Atoms*, 97(1–4):465–467, May 1995.

[102] T Pradell, D Crespo, N Clavaguera, and M T Clavaguera-Mora. Diffusion controlled grain growth in primary crystallization: Avrami exponents revisited. *Journal of Physics: Condensed Matter*, 10(17):3833–3844, May 1998.

[103] S. Ranganathan and M. Von Heimendahl. The three activation energies with isothermal transformations: Applications to metallic glasses. *Journal of Materials Science*, 16(9):2401–2404, September 1981.

[104] Joachim Stöhr. *Nexafs Spectroscopy*. Springer, 1992. ISBN 9783540544227.

[105] Y. Zou, T. Araki, G. Appel, A.L.D. Kilcoyne, and H. Ade. Solid state effects in the NEXAFS spectra of alkane-based van der waals crystals: Breakdown of molecular model. *Chemical Physics Letters*, 430(4–6):287–292, October 2006.

[106] Tina Graber, Frank Forster, Achim Schöll, and Friedrich Reinert. Experimental determination of the attenuation length of electrons in organic molecular solids: The example of PTCDA. *Surface Science*, 605(9–10): 878–882, May 2011.

[107] P. A. M. Dirac. The quantum theory of the emission and absorption of radiation. *Royal Society of London Proceedings Series A*, 114:243–265, March 1927.

[108] T Koopmans. Über die Zuordnung von Wellenfunktionen und Eigenwerten zu den einzelnen Elektronen eines Atoms. *Physica*, 1(1–6):104–113, 1934.

[109] Achim Schöll, Ying Zou, Thomas Schmidt, Rainer Fink, and Eberhard Umbach. High-resolution photoemission study of different NTCDA monolayers on Ag(111): bonding and screening influences on the line shapes. *The Journal of Physical Chemistry B*, 108(38):14741–14748, September 2004.

[110] Y. Zou, L. Kilian, A. Schöll, Th. Schmidt, R. Fink, and E. Umbach. Chemical bonding of PTCDA on Ag surfaces and the formation of interface states. *Surface Science*, 600(6):1240–1251, March 2006.

[111] M. Häming, A. Schöll, E. Umbach, and F. Reinert. Adsorbate-substrate charge transfer and electron-hole correlation at adsorbate/metal interfaces. *Physical Review B*, 85(23):235132, June 2012.

[112] Graeme L. Nyberg and Neville V. Richardson. Symmetry analysis of angle-resolved photoemission: Polarization dependence and lateral interactions in chemisorbed benzene. *Surface Science*, 85(2):335–352, July 1979.

[113] N. V. Richardson. Angle-resolved photoemission from adsorbate covered surfaces. In Peter Day, editor, *Emission and Scattering Techniques*, number 73 in NATO Advanced Study Institutes Series, pages 75–102. Springer Netherlands, January 1981. ISBN 978-94-009-8527-8, 978-94-009-8525-4.

[114] E. W. Plummer and W. Eberhardt. Angle-resolved photoemission as a tool for the study of surfaces. In I. Prigogine and Stuart A. Rice, editors, *Advances in Chemical Physics*, pages 533–656. John Wiley & Sons, Inc., 2007. ISBN 9780470142691.

[115] M. Born and R. Oppenheimer. Zur Quantentheorie der Molekeln. *Annalen der Physik*, 389(20):457–484, 1927.

[116] J. Franck and E. G. Dymond. Elementary processes of photochemical reactions. *Transactions of the Faraday Society*, 21(February):536–542, January 1926.

[117] Edward Condon. Minutes of the stanford meeting. *Physical Review*, 27: 637–644, May 1926.

[118] Edward U. Condon. Nuclear motions associated with electron transitions in diatomic molecules. *Physical Review*, 32(6):858–872, December 1928.

[119] Kun Huang and Avril Rhys. Theory of light absorption and non-radiative transitions in f-centres. *Proceedings of the Royal Society of London. Series A. Mathematical and Physical Sciences*, 204(1078):406–423, December 1950.

[120] L. S. Cederbaum and W. Domcke. A many-body approach to the vibrational structure in molecular electronic spectra. I. theory. *The Journal of Chemical Physics*, 64(2):603–611, January 1976.

[121] M Grunze. Preparation and characterization of self-assembled organic films on solid substrates. *Physica Scripta*, T49B:711–717, January 1993.

[122] W. E. S. Unger, A. Lippitz, C. Wöll, and W. Heckmann. X-ray absorption spectroscopy (NEXAFS) of polymer surfaces. *Fresenius' Journal of Analytical Chemistry*, 358(1):89–92, 1997.

[123] M. Hagelstein, A. San Miguel, A. Fontaine, and J. Goulon. The beamline ID24 at ESRF for energy dispersive X-ray absorption spectroscopy. *Le Journal de Physique IV*, 7(C2):C2–303–C2–308, April 1997.

[124] J. C. Lang, G. Srajer, J. Wang, and P. L. Lee. Performance of the advanced photon source 1-BM beamline optics. *Review of Scientific Instruments*, 70 (12):4457–4462, December 1999.

[125] O. Mathon, F. Baudelet, J.-P. Itié, S. Pasternak, A. Polian, and S. Pascarelli. XMCD under pressure at the Fe K edge on the energy-dispersive beamline of the ESRF. *Journal of Synchrotron Radiation*, 11(5):423–427, August 2004.

[126] Philip A. Heimann, Masato Koike, and Howard A. Padmore. Dispersive X-ray absorption spectroscopy with gratings above 2 keV. *Review of Scientific Instruments*, 76(6):063102–063102–3, May 2005.

[127] S. Pascarelli, O. Mathon, M. Muñoz, T. Mairs, and J. Susini. Energy-dispersive absorption spectroscopy for hard-X-ray micro-XAS applications. *Journal of Synchrotron Radiation*, 13(5):351–358, August 2006.

[128] K. Amemiya, Y. Kitajima, T. Ohta, and K. Ito. Design of a holographically recorded plane grating with a varied line spacing for a soft X-ray grazing-incidence monochromator. *Journal of Synchrotron Radiation*, 3(6):282–288, 1996.

[129] Yoshinori Kitajima, Kenta Amemiya, Yoshiki Yonamoto, Toshiaki Ohta, Takashi Kikuchi, Takashi Kosuge, Akio Toyoshima, and Kenji Ito. A soft X-ray (80–1500 eV) grazing-incidence monochromator with varied-line-spacing plane gratings at PF-BL-11A. *Journal of Synchrotron Radiation*, 5(3):729–731, 1998.

[130] Kenta Amemiya, Hiroshi Kondoh, Toshihiko Yokoyama, and Toshiaki Ohta. A soft X-ray beamline for surface chemistry at the photon factory. *Journal of Electron Spectroscopy and Related Phenomena*, 124(2–3):151–164, July 2002.

[131] D.R. Batchelor, Th. Schmidt, R. Follath, C. Jung, R. Fink, M. Knupfer, A. Schöll, T. Noll, F. Siewert, B. Büchner, and E. Umbach. An energy-dispersive VUV beamline for NEXAFS and other CFS/CIS studies. *Nuclear Instruments and Methods in Physics Research Section A: Accelerators, Spectrometers, Detectors and Associated Equipment*, 575(3):470–475, June 2007.

[132] H. Peisert, I. Biswas, L. Zhang, B.-E. Schuster, M. B. Casu, A. Haug, D. Batchelor, M. Knupfer, and T. Chassé. Unusual energy shifts in resonant photoemission spectra of organic model molecules. *The Journal of Chemical Physics*, 130(19):194705–194705–7, May 2009.

[133] Helmuth Petersen. The plane grating and elliptical mirror: A new optical configuration for monochromators. *Optics Communications*, 40(6):402–406, February 1982.

[134] Rolf Follath and Friedmar Senf. New plane-grating monochromators for third generation synchrotron radiation light sources. *Nuclear Instruments and Methods in Physics Research Section A: Accelerators, Spectrometers, Detectors and Associated Equipment*, 390(3):388–394, May 1997.

[135] Rolf Follath. The versatility of collimated plane grating monochromators. *Nuclear Instruments and Methods in Physics Research Section A: Accelerators, Spectrometers, Detectors and Associated Equipment*, 467–468, Part 1(0):418–425, July 2001.

[136] A. W. Kay, F. J. Garcia de Abajo, S.-H. Yang, E. Arenholz, B. S. Mun, N. Mannella, Z. Hussain, M. A. Van Hove, and C. S. Fadley. Multiatom resonant photoemission. *Physical Review B*, 63(11):115119, March 2001.

[137] D. Nordlund, M. G. Garnier, N. Witkowski, R. Denecke, A. Nilsson, M. Nagasono, N. Mårtensson, and A. Föhlisch. Limits to the quantitative analysis of multiatom resonant photoemission: The case of c(2×2)O/Ni(100). *Physical Review B*, 63(12):121402, March 2001.

[138] M Tronc, G C King, and F H Read. Carbon k-shell excitation in small molecules by high-resolution electron impact. *Journal of Physics B: Atomic and Molecular Physics*, 12(1):137–157, January 1979.

[139] A.P. Hitchcock and C.E. Brion. K-shell excitation spectra of CO, N2 and O2. *Journal of Electron Spectroscopy and Related Phenomena*, 18(1):1–21, 1980.

[140] T. K. Sham, B. X. Yang, J. Kirz, and J. S. Tse. K-edge near-edge X-ray-absorption fine structure of oxygen- and carbon-containing molecules in the gas phase. *Physical Review A*, 40(2):652–669, July 1989.

[141] A. Schöll, Y. Zou, T. Schmidt, R. Fink, and E. Umbach. Energy calibration and intensity normalization in high-resolution nexafs spectroscopy. *Journal of Electron Spectroscopy and Related Phenomena*, 129(1):1–8, March 2003.

[142] M. Rei Vilar, M. Schott, and P. Pfluger. Vibrational and electronic excitation of hexatriacontane thin films by low energy electron impact. *The Journal of Chemical Physics*, 92(9):5722–5730, May 1990.

[143] Fabrice Amy, Calvin K. Chan, Wei Zhao, Jaehyung Hyung, Masaki Ono, Tomoki Sueyoshi, Satoshi Kera, Guy Nesher, Adi Salomon, Lior Segev, Oliver Seitz, Hagay Shpaisman, Achim Schöll, Marc Haeming, Till Böcking, David Cahen, Leeor Kronik, Nobuo Ueno, Eberhard Umbach, and Antoine Kahn. Radiation damage to alkyl chain monolayers on semiconductor substrates investigated by electron spectroscopy. *The Journal of Physical Chemistry B*, 110(43):21826–21832, November 2006.

[144] Masaki Ono and Eizi Morikawa. Ultraviolet photoelectron spectroscopy study of synchrotron radiation-degraded polyethylene ultrathin films. *The Journal of Physical Chemistry B*, 108(6):1894–1897, February 2004.

[145] K. Heister, M. Zharnikov, M. Grunze, L. S. O. Johansson, and A. Ulman. Characterization of X-ray induced damage in alkanethiolate monolayers by high-resolution photoelectron spectroscopy. *Langmuir*, 17(1):8–11, January 2001.

[146] Nobuo Ueno, Kazuyuki Sugita, Osamu Koga, and Shin Suzuki. Radiation effect in hexatriacontane thin film. *Japanese Journal of Applied Physics*, 22(Part 1, No. 10):1613–1617, 1983.

[147] D Gador, C Buchberger, R Fink, and E Umbach. Manipulation of molecular orientation in ultrathin organic films: NTCDA on Ag(111). *Europhysics Letters (EPL)*, 41(2):231–236, January 1998.

[148] Anthony J. Wagner, Keping Han, Amanda L. Vaught, and D. Howard Fairbrother. X-ray induced modification of semifluorinated organic thin films†. *The Journal of Physical Chemistry B*, 104(14):3291–3297, April 2000.

[149] Eizi Morikawa, Jaewu Choi, Harish M. Manohara, Hisao Ishii, Kazuhiko Seki, Koji K. Okudaira, and Nobuo Ueno. Photoemission study of direct photomicromachining in poly(vinylidene fluoride). *Journal of Applied Physics*, 87(8):4010–4016, April 2000.

[150] Dominique Hübner. *Vibronic and electronic excitations of large organic molecules in gas and condensed phase*. Ph. D thesis, Universität Würzburg, January 2012.

[151] Liborius Born and Gerhard Heywang. Crystal structure of 1,4,5,8-naphthalene-tetracarboxylic-dianhydride (NTDA). *Zeitschrift für Kristallographie*, 190(1-2):147–152, January 1990.

[152] R. Strohmaier, C. Ludwig, J. Petersen, B. Gompf, and W. Eisenmenger. STM investigations of NTCDA on weakly interacting substrates. *Surface Science*, 351(1–3):292–302, May 1996.

[153] Yusuke Miyamoto, Takashi Nemoto, Kaname Yoshida, Hiroki Kurata, and Seiji Isoda. *In Situ* atomic force microscopy observation of the desorption process from monomolecular organic layers of a naphthalene derivative. *Japanese Journal of Applied Physics*, 43(7B):4606–4609, 2004.

[154] Vitaliy Shklover. *HREELS- und FTIRRAS-Untersuchungen an organischen Dünnschichten : PTCDA und NTCDA auf Ag*. Ph. D thesis, 2002.

[155] D. Gador, C. Buchberger, R. Fink, and E. Umbach. Characterization of high-quality NTCDA films on metal substrates. *Journal of Electron Spectroscopy and Related Phenomena*, 96(1–3):11–17, November 1998.

[156] Ullrich Groh. *Spektromikroskopische Untersuchungen an organischen Nanostrukturen*. Ph. D thesis, Universität Würzburg, January 2007.

[157] J. F. Morar, F. J. Himpsel, G. Hollinger, G. Hughes, and J. L. Jordan. Observation of a C 1s core exciton in diamond. *Physical Review Letters*, 54(17):1960–1963, April 1985.

[158] P. A. Brühwiler, A. J. Maxwell, C. Puglia, A. Nilsson, S. Andersson, and N. Mårtensson. π^* and σ^* excitons in C 1s absorption of graphite. *Physical Review Letters*, 74(4):614–617, January 1995.

[159] Frank Würthner, Theo E. Kaiser, and Chantu R. Saha-Möller. J-aggregates: From serendipitous discovery to supramolecular engineering of functional dye materials. *Angewandte Chemie International Edition*, 50 (15):3376–3410, 2011.

[160] O. Björneholm, M. Bässler, A. Ausmees, I. Hjelte, R. Feifel, H. Wang, C. Miron, M. N. Piancastelli, S. Svensson, S. L. Sorensen, F. Gel'mukhanov, and H. Ågren. Doppler splitting of in-flight auger decay of dissociating oxygen molecules: The localization of delocalized core holes. *Physical Review Letters*, 84(13):2826–2829, March 2000.

[161] Daniel Rolles, Markus Braune, Slobodan Cvejanović, Oliver Geßner, Rainer Hentges, Sanja Korica, Burkhard Langer, Toralf Lischke, Georg Prümper, Axel Reinköster, Jens Viefhaus, Björn Zimmermann, Vincent McKoy, and Uwe Becker. Isotope-induced partial localization of core electrons in the homonuclear molecule n2. *Nature*, 437(7059):711–715, September 2005.

[162] M. S. Schöffler, J. Titze, N. Petridis, T. Jahnke, K. Cole, L. Ph. H. Schmidt, A. Czasch, D. Akoury, O. Jagutzki, J. B. Williams, N. A. Cherepkov, S. K. Semenov, C. W. McCurdy, T. N. Rescigno, C. L. Cocke, T. Osipov, S. Lee, M. H. Prior, A. Belkacem, A. L. Landers, H. Schmidt-Böcking, Th. Weber, and R. Dörner. Ultrafast probing of core hole localization in N2. *Science*, 320(5878):920–923, May 2008.

[163] Carolin R. Braatz, Gregor Öhl, and Peter Jakob. Vibrational properties of the compressed and the relaxed 1,4,5,8-naphthalene-tetracarboxylic dianhydride monolayer on Ag(111). *The Journal of Chemical Physics*, 136(13): 134706–134706–8, April 2012.

[164] Nobuhiro Kosugi. Strategies to vectorize conventional SCF-Cl algorithms. *Theoretical Chemistry Accounts: Theory, Computation, and Modeling (Theoretica Chimica Acta)*, 72(2):149–173, 1987.

[165] Florian Holch, Dominique Hübner, Rainer Fink, Achim Schöll, and Eberhard Umbach. New set-up for high-quality soft-X-ray absorption spectroscopy of large organic molecules in the gas phase. *Journal of Electron Spectroscopy and Related Phenomena*, 184(8–10):452–456, November 2011.

[166] Wenlan Liu. *Exciton Coupling in Valence and Core Excited Aggregates of π-Conjugated Molecules*. Ph. D thesis, April 2011.

[167] M. Dauth, T. Körzdörfer, S. Kümmel, J. Ziroff, M. Wiessner, A. Schöll, F. Reinert, M. Arita, and K. Shimada. Orbital density reconstruction for molecules. *Physical Review Letters*, 107(19):193002, November 2011.

[168] Jan Roden, Georg Schulz, Alexander Eisfeld, and John Briggs. Electronic energy transfer on a vibronically coupled quantum aggregate. *The Journal of Chemical Physics*, 131(4):044909–044909–17, July 2009.

[169] Note that the coupling strength was chosen arbitrarily in order to match the observed changes of the vibronic progression.

[170] Edwin Jelley. Spectral absorption and fluorescence of dyes in the molecular state. *Nature*, 1936.

[171] G. Scheibe. Über die Veränderlichkeit der Absorptionsspektren in Lösungen und die Nebenvalenzen als ihre Ursache. *Angewandte Chemie*, 50(11): 212–219, 1937.

[172] James Franck and Edward Teller. Migration and photochemical action of excitation energy in crystals. *The Journal of Chemical Physics*, 6(12): 861–872, December 1938.

[173] Joseph Klafter and Joshua Jortner. Some effects of structural disorder on the optical properties of organic molecular crystals. *Chemical Physics Letters*, 50(2):202–206, September 1977.

[174] A.V. Lukashin and M.D. Frank-Kamenetskii. Comparison of different theoretical descriptions of vibronic spectra of molecular aggregates. *Chemical Physics Letters*, 45(1):36–40, January 1977.

[175] Joseph Klafter and Joshua Jortner. Effects of structural disorder on the optical properties of molecular crystals. *The Journal of Chemical Physics*, 68(4):1513–1522, February 1978.

[176] Jan Roden, Alexander Eisfeld, Wolfgang Wolff, and Walter T. Strunz. Influence of complex exciton-phonon coupling on optical absorption and energy transfer of quantum aggregates. *Physical Review Letters*, 103(5):058301, July 2009.

[177] Frank C. Spano. The spectral signatures of frenkel polarons in H- and J-aggregates. *Accounts of Chemical Research*, 43(3):429–439, March 2010.

[178] E.W. Knapp. Lineshapes of molecular aggregates, exchange narrowing and intersite correlation. *Chemical Physics*, 85(1):73–82, March 1984.

[179] D. L Dexter. A theory of sensitized luminescence in solids. *The Journal of Chemical Physics*, 21(5):836–850, May 1953.

[180] C. Keller, M. Stichler, G. Comelli, F. Esch, S. Lizzit, D. Menzel, and W. Wurth. Femtosecond dynamics of adsorbate charge-transfer processes as probed by high-resolution core-level spectroscopy. *Physical Review B*, 57(19):11951–11954, May 1998.

[181] A. Föhlisch, D. Menzel, P. Feulner, M. Ecker, R. Weimar, K.L. Kostov, G. Tyuliev, S. Lizzit, R. Larciprete, F. Hennies, and W. Wurth. Energy dependence of resonant charge transfer from adsorbates to metal substrates. *Chemical Physics*, 289(1):107–115, April 2003.

[182] A. Föhlisch, P. Feulner, F. Hennies, A. Fink, D. Menzel, D. Sanchez-Portal, P. M. Echenique, and W. Wurth. Direct observation of electron dynamics in the attosecond domain. *Nature*, 436(7049):373–376, July 2005.

[183] C. H. Schwalb, S. Sachs, M. Marks, A. Schöll, F. Reinert, E. Umbach, and U. Höfer. Electron lifetime in a shockley-type metal-organic interface state. *Physical Review Letters*, 101(14):146801, September 2008.

[184] N. Armbrust, J. Güdde, P. Jakob, and U. Höfer. Time-resolved two-photon photoemission of unoccupied electronic states of periodically rippled graphene on Ru(0001). *Physical Review Letters*, 108(5):056801, January 2012.

[185] Askat E. Jailaubekov, Adam P. Willard, John R. Tritsch, Wai-Lun Chan, Na Sai, Raluca Gearba, Loren G. Kaake, Kenrick J. Williams, Kevin Leung, Peter J. Rossky, and X.-Y. Zhu. Hot charge-transfer excitons set the time limit for charge separation at donor/acceptor interfaces in organic photovoltaics. *Nature Materials*, 12(1):66–73, January 2013.

[186] G. Nicolay, F. Reinert, S. Schmidt, D. Ehm, P. Steiner, and S. Hüfner. Natural linewidth of the Ag(111) L-gap surface state as determined by photoemission spectroscopy. *Physical Review B*, 62(3):1631–1634, July 2000.

[187] J. Ziroff, S. Hame, M. Kochler, A. Bendounan, A. Schöll, and F. Reinert. Low-energy scale excitations in the spectral function of organic monolayer systems. *Physical Review B*, 85(16):161404, April 2012.

[188] Azzedine Bendounan, Frank Forster, Achim Schöll, David Batchelor, Johannes Ziroff, Eberhard Umbach, and Friedrich Reinert. Electronic structure of 1 ML NTCDA/Ag(111) studied by photoemission spectroscopy. *Surface Science*, 601(18):4013–4017, September 2007.

[189] L. Kilian, U. Stahl, I. Kossev, M. Sokolowski, R. Fink, and E. Umbach. The commensurate-to-incommensurate phase transition of an organic monolayer: A high resolution LEED analysis of the superstructures of NTCDA on Ag(111). *Surface Science*, 602(14):2427–2434, July 2008.

[190] Steffen Duhm, Georg Heimel, Ingo Salzmann, Hendrik Glowatzki, Robert L. Johnson, Antje Vollmer, Jürgen P. Rabe, and Norbert Koch. Orientation-dependent ionization energies and interface dipoles in ordered molecular assemblies. *Nature Materials*, 7(4):326–332, 2008.

[191] Wei Chen, Han Huang, Shi Chen, Yu Li Huang, Xing Yu Gao, and Andrew Thye Shen Wee. Molecular orientation-dependent ionization potential of organic thin films. *Chemistry of Materials*, 20(22):7017–7021, November 2008.

[192] Stijn Verlaak, David Beljonne, David Cheyns, Cedric Rolin, Mathieu Linares, Frédéric Castet, Jérôme Cornil, and Paul Heremans. Electronic structure and geminate pair energetics at Organic–Organic interfaces: The case of Pentacene/C60 heterojunctions. *Advanced Functional Materials*, 19 (23):3809–3814, 2009.

[193] Wei Chen, Dong-Chen Qi, Han Huang, Xingyu Gao, and Andrew T. S. Wee. Organic–Organic heterojunction interfaces: Effect of molecular orientation. *Advanced Functional Materials*, 21(3):410–424, 2011.

[194] A. Schöll, L. Kilian, Y. Zou, J. Ziroff, S. Hame, F. Reinert, E. Umbach, and R. H. Fink. Disordering of an organic overlayer on a metal surface upon cooling. *Science*, 329(5989):303–305, July 2010.

[195] Detlef Gador. *Organische Dünnschichten auf Einkristalloberflächen: Wachstumsverhalten und elektronische Struktur an Grenzflächen*. Ph. D thesis, 1999.

[196] Achim Schöll. *High-resolution investigation of the electronic structure of organic thin films*. Ph. D thesis, November 2004.

[197] W. Eberhardt. Clusters as new materials. *Surface Science*, 500(1–3):242–270, March 2002.

[198] Roy L. Johnston. *Atomic and Molecular Clusters*. CRC Press, December 2010. ISBN 9781420055771.

[199] Ben L. Feringa, editor. *Molecular Switches*. Wiley-VCH Verlag GmbH, 2001. ISBN 9783527600328. i–xxii pp.

[200] Charles P. Collier, Gunter Mattersteig, Eric W. Wong, Yi Luo, Kristen Beverly, José Sampaio, Françisco M. Raymo, J. Fraser Stoddart, and James R. Heath. A [2]Catenane-Based solid state electronically reconfigurable switch. *Science*, 289(5482):1172–1175, August 2000. PMID: 10947980.

[201] B. Crone, A. Dodabalapur, Y.-Y. Lin, R. W. Filas, Z. Bao, A. LaDuca, R. Sarpeshkar, H. E. Katz, and W. Li. Large-scale complementary integrated circuits based on organic transistors. *Nature*, 403(6769):521–523, February 2000.

[202] Jana Zaumseil and Henning Sirringhaus. Electron and ambipolar transport in organic field-effect transistors. *Chemical Reviews*, 107(4):1296–1323, April 2007. WOS:000245600000011.

[203] Amanda R. Murphy and Jean M. J. Frechet. Organic semiconducting oligomers for use in thin film transistors. *Chemical Reviews*, 107(4):1066–1096, April 2007. WOS:000245600000005.

[204] Ge Yang, Chong-an Di, Guanxin Zhang, Jing Zhang, Junfeng Xiang, Deqing Zhang, and Daoben Zhu. Highly sensitive chemical-vapor sensor based on thin-film organic field-effect transistors with benzothiadiazole-fused-tetrathiafulvalene. *Advanced Functional Materials*, 23(13):1671–1676, April 2013. WOS:000317019100009.

[205] Mariano Campoy-Quiles, Toby Ferenczi, Tiziano Agostinelli, Pablo G. Etchegoin, Youngkyoo Kim, Thomas D. Anthopoulos, Paul N. Stavrinou, Donal D. C. Bradley, and Jenny Nelson. Morphology evolution via self-organization and lateral and vertical diffusion in polymer:fullerene solar cell blends. *Nature Materials*, 7(2):158–164, February 2008.

[206] A. J. Moulé and K. Meerholz. Controlling morphology in Polymer–Fullerene mixtures. *Advanced Materials*, 20(2):240–245, 2008.

[207] B. A. Collins, J. E. Cochran, H. Yan, E. Gann, C. Hub, R. Fink, C. Wang, T. Schuettfort, C. R. McNeill, M. L. Chabinyc, and H. Ade. Polarized X-ray scattering reveals non-crystalline orientational ordering in organic films. *Nature Materials*, 11(6):536–543, June 2012.

[208] P. Vanlaeke, A. Swinnen, I. Haeldermans, G. Vanhoyland, T. Aernouts, D. Cheyns, C. Deibel, J. D'Haen, P. Heremans, J. Poortmans, and J.V. Manca. P3HT/PCBM bulk heterojunction solar cells: Relation between morphology and electro-optical characteristics. *Solar Energy Materials and Solar Cells*, 90(14):2150–2158, September 2006.

[209] Li-Min Chen, Ziruo Hong, Gang Li, and Yang Yang. Recent progress in polymer solar cells: Manipulation of polymer: Fullerene morphology and the formation of efficient inverted polymer solar cells. *Advanced Materials*, 21(14-15):1434–1449, April 2009. WOS:000265866300003.

[210] Christoph J. Brabec, Martin Heeney, Iain McCulloch, and Jenny Nelson. Influence of blend microstructure on bulk heterojunction organic photovoltaic performance. *Chemical Society Reviews*, 40(3):1185–1199, February 2011.

Danksagung

An dieser Stelle bedanke ich mich bei allen, die zum Gelingen dieser Arbeit beigetragen haben.

Mein besonderer Dank gilt Priv.-Doz. Dr. Achim Schöll, seinem Vertrauen und der höchst interessanten wissenschaftlichen Fragestellung. Er hat mir ein sehr freies wissenschaftliches Arbeiten ermöglicht, hatte aber immer ein offenes Ohr für Fragen und bei Probleme. Stets konnte ich mich in kniffligen Situationen auf seine Denkansätze und Vorschläge verlassen. Nichtsdestoweniger danke ich Prof. Dr. Friedrich Reinert für die Aufnahme in seine Arbeitsgruppe. Ich schätze seine Sichtweise auf organische Filme sehr, auch weil sie mich oft zum Nachdenken anregte. Zudem gewann ich viele spannende Einblicke in Themenbereiche jenseits der Organik.

Prof. Dr. Jean Geurts danke ich für die freundliche Bereitschaft das Zweitgutachten zu übernehmen und Prof. Dr. Björn Trauzettel für seine Teilnahmen am Promotionskolloquium als dritter Prüfer.

Ein Großteil dieser Arbeit entstand bei BESSY. Deshalb danke ich besonders den vielen Helfern während meiner Messungen. Die Hilfe, Neugier und Begeisterung von Christoph Sauer und Michael Wiessner ermöglichten viele der Ergebnisse und machten die Messzeiten zu unvergesslichen Erlebnissen. Besonders danken möchte ich Dr. David Batchelor und seiner Hilfe zu Beginn unserer energiedispersiven NEXAFS Messungen. Seine enorme Erfahrung und speziellen Kenntnisse der UE52-PGM Beamline halfen in vielen Situationen sehr weiter.

Auch möchte ich Sophia Huppmann und Dirk Hauschild danken, die ich während ihrer Diplomarbeit betreute und Dr. Caroline Arantes DaSilva für die Zusammenarbeit zu Beginn meiner Doktorandenzeit.

Mit Than-Nam Nguyen teilte ich mir viele Jahre eine UHV-Kammer und ein Büro. Mir hat es immer sehr viel Spass gemacht mit ihm zu arbeiten. Auf die

Hilfe von Sebastian Fiedler, Chul-Hee Min und zuletzt Peter Lutz konnte ich mich immer verlassen. Vielen Dank! Patrick Bayersdorfer danke ich für seine LEED-Software.

Als Kollegiat des Graduiertenkolleg GRK 1221 hörte ich viele interessante Vorträge und gewann Einblick in chemische Aspekte.

Bei der gesamten EP 7 möchte ich mich für die tolle Atmosphäre bedanken. Ich war gerne ein Teil dieser Arbeitsgruppe.

Zum Schluss möchte ich mich bei meiner Familie und ihrer bedingungslosen Unterstützung bedanken.

Eidesstattliche Erklärung

gemäß § 5, Abs. 2, Satz 2, 3, 4 und 6 der
Promotionsordnung der
Fakultät für Physik und Astronomie der
Julius-Maximilians-Universität Würzburg

Hiermit erkläre ich an Eides statt, dass ich die vorliegende Dissertation eigenständig, d.h. insbesondere selbstständig und ohne Hilfe einer kommerziellen Promotionsberatung angefertigt und keine anderen als die von mir angegebenen Quellen und Hilfsmittel benutzt habe und dass ich die Gelegenheit zum Promotionsvorhaben nicht kommerziell vermittelt bekommen habe und insbesondere nicht eine Person oder Organisation eingeschaltet habe, die gegen Entgelt Betreuer bzw. Betreuerinnen für die Anfertigung von Dissertationen sucht.

Hiermit erkläre ich zudem, dass ich die Regeln der Universität Würzburg über gute wissenschaftliche Praxis eingehalten habe und dass ich die Dissertation in gleicher oder anderer Form nicht bereits in einem anderen Prüfungsfach vorgelegt habe.

Würzburg, den 07.06.2013

Markus Scholz